CARDIFF
UNIVERSITY
PRIFYSGOL
CAERDYDD

BINDING SERVICES
Tel +44 (0)29 2087 4949
Fax +44 (0)29 20371921
e-mail bindery@cardiff.ac.uk

ProQuest LLC
789 East Eisenhower Parkway
P.O. Box 1346
Ann Arbor, MI 48106-1346

Polariton Optics of Spherical Nanostructures

by

Andrew Smith

A thesis submitted to

Cardiff University

for the degree of

Doctor of Philosophy

2005

"God runs electromagnetics by wave theory on Monday, Wednesday, and Friday, and the Devil runs them by quantum theory on Tuesday, Thursday, and Saturday."
– Sir William Bragg, (1862 - 1942)

Dedicated to absent friends.

ACKNOWLEDGEMENTS

I would like to express my gratitude to the many people who gave me a great deal of help and support throughout my PhD. First and foremost is Prof. Alexei Ivanov who has supervised me throughout my PhD. The line of research I took and the discovery of the polariton transition point was due to his suggestion, and without him this thesis would be very different. In addition I have been fortunate in being able to work closely with Dr. Nikolay Nikolaev for the past two years, and he has worked a great deal on the research. His help has simply been invaluable.

Through Alex and Nikolay I have been able to interact with members of the Photon Mediated Phenomena Network; a Research Training Network set up under the European Commission's Fifth Framework Programme. This has not only afforded me the opportunity to attend several excellent conferences, but has also generated many interesting discussions with its members including Prof. Peter Littlewood (Cambridge University), Prof. Ulrike Woggon (Dortmund University), Dr. Detlef Schikora (Paderborn University) and Prof. Le Si Dang (Grenoble University). In particular I would like to thank Dr. Mats-Erik Pistol of Lund University for many informative discussions on the practical aspects of photoluminescence experiments on quantum dots.

A special thank you goes to Kikuo Cho and Hiroshi Ajiki for many discussions regarding my work in relation to their own, despite the long distances involved.

I'd also like to thank the administrative staff, particularly everyone in the main office, for making sense of all the department's procedures for me. Also Rob Evans, Paul Jones and the computer support team, for ensuring that inevitable technical glitches never proved to be (too) detrimental to my progress.

Beyond technical considerations I'd like to give a wide thank you to numerous friends. Cele Creatore and Lois Smallwood have helped to bring an occasional smile and a laugh to the office. Tim Waskett and Owen Davies, amongst others, have been around for a long time, and helped with the technical aspects of writing this thesis. Outside the department I'd like to thank all my friends for keeping me sane. In particular I'd like to thank Lex and Tom for always asking me how the work was going, and for putting up with me working late around the house.

My family have given me a great deal of support during my time here in Cardiff, both as an undergraduate and postgraduate. They may not understand my work, but they have been very understanding when it has kept me away from home.

Lastly I reserve a special thank you for Bronwen for all her love and support over the past years. She has given me encouragement when things have been hard and understanding when work has run late.

ABSTRACT

This thesis describes the completely coherent polariton optics of a spherical semiconductor photonic dot (PD). Our theoretical model solves the eigen-modes of the system to produce the polariton frequencies as a function of the PD radius, $\omega(a)$, where the photonic modes with $\lambda = 2a$ are resonant with the sphere. Dispersion curves are classified into the weak and strong coupling regimes according to crossing/anti-crossing of the polariton branches, in analogy with polaritons in bulk materials. We assume the coherent distribution of energy between the photonic and excitonic branches in order to calculate the total radiative linewidth.

The effect of spatial dispersion of excitons is considered using the dispersion equations developed by Ruppin and the Pekar Additional Boundary Condition. The asymptotic values of the resulting dispersion curves are described, and plots of the dispersion curves for a CuCl PD show low-order modes ($n = 1$ and 2) to be in the weak coupling regime, whilst $n = 3$ and 4 are in the strong regime.

Our analysis of the radiative linewidth, both including and excluding spatial dispersion, produces a $1/a$ dependence for Γ_n for large radii, corresponding the "ballistic escape" of optically-dressed excitons from the PD. The low-radius behaviour, usually described as an a^3 volume-dependent increase of the oscillator strength, is shown to be more complex with powers from a^1 - a^7 depending on the mode polarisation and the presence/absence of spatial dispersion.

The transition between weak and strong coupling regimes is identified as a discrete point at which the two polariton branches meet, characterised by critical values of the Rabi frequency, dielectric permittivities of the PD and surrounding material, and the PD radius, which have been obtained analytically and numerically. We propose the observation of the transition point via derivatives of the radiative linewidth, using high-precision modulation techniques.

PUBLICATIONS

N. I. Nikolaev, A. Smith, A. L. Ivanov. Polariton optics of semiconductor photonic dots: weak and strong coupling limits. *J. Phys.-Condens. Mat.* 16:S3703-S3719, 2004.

A. Smith, N. I. Nikolaev, A. L. Ivanov. *Coherent optics of spherical photonic dots: transition between weak and strong coupling*, in 27th International Conference on the Physics of Semiconductors, edited by J. Menendez and C. Van de Walle, AIP Conference Proceedings Volume 772. American Institute of Physics, Melville, NY, 2005, pp. 757-758.

N. I. Nikolaev, A. Smith, A. L. Ivanov. Weak-strong coupling polariton transition in a spherical photonic dot. *Phys. Rev. B*, submitted.

Contents

List of Figures

Chapter 1

Introduction

Polaritons arise from the resonant interaction of photons with a matter excitation; excitons or transverse-optical- (TO-) phonons, resulting in hybridised eigenmodes which are a mixture of the original, non-interacting states. Theoretical description of this phenomena was done in the 1950's, first semiclassically by Born and Huang [1], and then quantum mechanically by Fano and Hopfield [2, 3]. In 1960 Maiman demonstrated the first laser, providing a coherent light source for the laboratory and sparking a revolution in experimental optics, including the study of polaritons. Resonant Brillouin scattering (RBS) and hyper-Raman scattering experiments produced measurements of the polariton dispersion curves in bulk semiconductors [4, 5], proving polaritons to be true excitations of the material and a fundamental process in light-matter interaction. Their properties were thoroughly studied, including absorption [3, 6, 7, 8], luminescence [9, 10, 11], non-linear optics [12], and reflectivity [13, 14].

Developments in semiconductor growth and fabrication techniques led to the ability to engineer materials on smaller length scales, producing first microstructures and then nanostructures. This saw reseach interests move away from bulk materials towards lower-dimensionality structures; quantum wells (QWs) which are quasi-2-dimensional [15], 1-dimensional quantum wires, and finally 0-dimensional quantum dots (QDs) [16]. The novel physics present in low-dimensional structures in general have led to many valuable applications such as quantum dot lasers [17] and photonic crystals [18], with grand aims for future applications such as quantum computing [19] and quantum cryptography [20].

The study of polaritons progressed in tandem with these advances in material engineering. The effect of these low-dimensional systems on both light and matter excitations lead to subsequent effects on the polaritons.

1.1 Background Theory

We will now review the background theory of this research in the published literature. For the purposes of this work we are interested only in exciton-polaritons, so we begin with a basic description of excitons in bulk semiconductors, before proceeding to the interaction of excitons and photons and the formation of polaritons.

1.1.1 Excitons

Excitation of electrons in semiconductors and insulators can form excitons: Coulomb-correlated electron-hole pairs. The energy levels can be calculated assuming that the electron and hole bands are isotropic, parabolic and non-degenerate using [21]:

$$E_n(\mathbf{k}) = E_{\mathrm{G}} - \frac{R^*}{n^2} + \frac{\hbar^2\mathbf{k}^2}{2M_{\mathrm{x}}} = E_{n,T} + \frac{\hbar^2\mathbf{k}^2}{2M_{\mathrm{x}}}, \tag{1.1}$$

where n is the principal quantum number, $\mathbf{k}$ is the wavevector, E_{G} is the energy gap, $M_{\mathrm{x}} = m_e + m_h$ is the exciton translational effective mass, and $E_{n,T}$ is the n^{th} transverse exciton energy. R^* is the excitonic Rydberg energy:

$$R^* = \frac{1}{2}\frac{\mu e^4}{\hbar^2 \varepsilon_{\mathrm{b}}^2}, \tag{1.2}$$

where $\mu = (m_e m_h)/(m_e + m_h)$ is the exciton reduced mass, and ε_{b} is the background dielectric permittivity. This assumes that the effective mass approximation holds; $R^* \ll E_{\mathrm{G}}$. This two-band band description of excitons is a useful approximation, but does not fully describe excitons in most semiconductors, for example heavy- and light-hole excitons. However, a full description of excitonic properties is beyond the scope of this thesis. We stress, however, the useful description of the exciton as a point-particle in the effective mass approximation, allowing the relative electron-hole motion to be neglected in favour of the translational motion of the exciton as a whole.

1.1.2 Exciton-photon interaction

The observed properties of bulk materials depend crucially on the *hierarchy of couplings* [22], in which all possible exciton interactions are ordered according to their strength relative to the incoherent perturbation of excitons within the material. If one interaction is stronger than all others *and* incoherent perturbations, then this coupling describes the states within the material. We will consider the case where exciton-photon coupling is strong compared to all others.

The non-interacting exciton dispersion curve is, within the approximation described in the preceeding section, a parabola $E_{n,T} + \hbar^2\mathbf{k}^2/2M_{\mathrm{x}}$. The photon dispersion is a straight line; $\hbar c\mathbf{k}/\sqrt{\varepsilon_b}$. Due to the laws of conservation, the interaction of excitons and photons can only occur in the proximity of the crossing point of these dispersions in the ω,$\mathbf{k}$ plane. The relative strength of this interaction can be described by several parameters; the oscillator strength per unit cell f_{exc}, the exciton polarisability α, or the longitudinal-transverse splitting energy E_{LT} [23]. The resulting dispersion curves can be classified into two cases; the *weak coupling* and *strong coupling* regimes.

Weak coupling

In the weak coupling regime excitons resulting from the absorption of photons experience a scattering event before the reverse process, i.e. the recombination of the exciton and corresponding emission of a photon, can occur. This scattering occurs in time $\tau_{\mathrm{x}} = 1/\Gamma$. The rate of absorption of light in then determined by the exciton-photon coupling. The photons and exciton remain separate and distinct, and their dispersion curves remain similar to the non-interacting curves described above.

Strong coupling

The strong coupling regime corresponds to the scattering time being longer than the recombination time of the exciton. A photon may then be absorbed into an exciton and re-emitted many times before a scattering event occurs. The exciton and photon are then hybridised, the propagation of excitons and photons can no longer be considered separately, and polaritons become the true eigenstates of the system. The time oscillation of the system from one component to another is described by the Rabi formula [24, 25], with frequency $\Omega_{\mathrm{R}} \simeq \sqrt{2\omega_{\mathrm{LT}}\omega_{\mathrm{T}}}$, where ω_{T}

is the frequency of the excitonic resonance and $\omega_{\mathrm{LT}} = E_{\mathrm{LT}}/\hbar$.

1.1.3 Exciton-polaritons

Since we will in general consider exciton-polaritons throughout this work, as opposed to, for example phonon-polaritons, we will drop the "exciton" prefix for brevity in referring to exciton-polaritons. The dispersion relation can be obtained classically [1] or quantum mechanically [3, 6] in the single-band approximation to be:

$$\varepsilon(\mathbf{k},\omega) = \frac{c^2\mathbf{k}^2}{\omega^2} = \varepsilon_{\mathrm{b}} + \frac{4\pi\alpha\omega_n^2(\mathbf{k})}{\omega_n^2(\mathbf{k}) - \omega^2}, \tag{1.3}$$

where $\omega_n(\mathbf{k})$ is the non-interacting exciton dispersion curve, equation (1.1). The resulting dispersion curves, $\omega(\mathbf{k})$, are shown in figure 1.1. There $n = 1$ dispersion curve is characterised by $E_{\mathrm{T}} = E_{\mathrm{G}} - R^*$, ε_{b}, M_{x} and a term for the strength of exciton-photon interaction; f_{exc}, α, or E_{LT}. For polaritons associated with excited exciton levels $n > 1$ we expect polariton effects to becoming increasingly less important because the exciton-photon interaction terms depend on n as n^{-3}. In the models we develop in later chapters we will consider a generic excitonic resonance, which can be applied to these excited excitons if desired.

Incoherent scattering, γ_{x}, which was neglected in equation 1.3, serves to damp exciton-photon interaction and hence polaritonic effects. Tait showed that for small scattering rates, $\gamma_{\mathrm{x}} < 0.1\ \omega_{\mathrm{LT}}$, the polariton dispersion curves are relatively unaffected, however as scattering is increased the dispersion curves undergo a drastic change at a critical value, $\gamma_{\mathrm{x}}^{\mathrm{cr}}$, given by [26]:

$$\gamma_{\mathrm{x}}^{\mathrm{cr}} = 2^{3/2}\left(\frac{\hbar\omega_{\mathrm{T}}^2\omega_{\mathrm{LT}}}{M_{\mathrm{x}}c^2}\right)^{1/2} = 2^{3/2}\left(\frac{\omega_{\mathrm{T}}}{\omega_{\mathrm{LT}}}\right)^{1/2}\left(\frac{\hbar\omega_{\mathrm{T}}}{M_{\mathrm{x}}c^2}\right)^{1/2}\omega_{\mathrm{LT}}^{-1}. \tag{1.4}$$

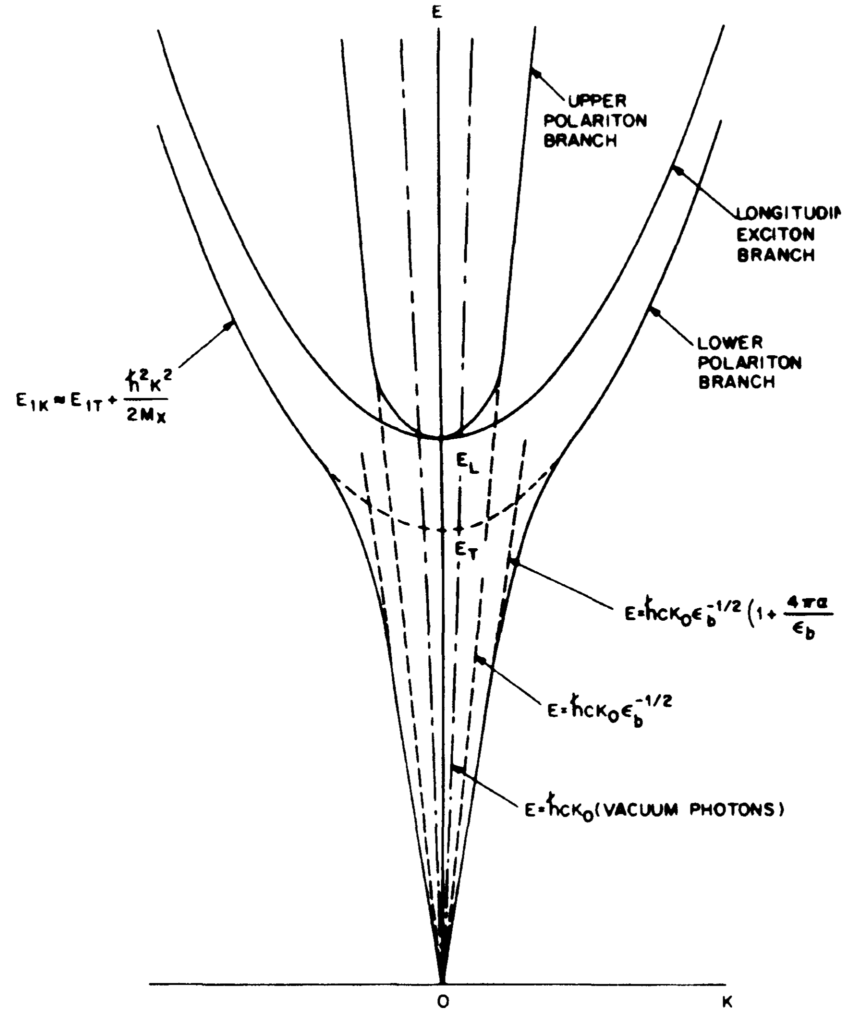

Figure 1.1: Dispersion curves for excitonic polaritons in the vicinity of a single exciton resonance E_T. Note that the asymptotic photon-like polariton states above E_L are normalised by all excitations of the crystal above E_L (photon "dressed" according to the background dielectric constant ε_b) and below E_T by the same plus the excitonic level (total dielectric constant $\varepsilon_b + 4\pi\alpha$). Vacuum photon and longitudinal exciton (uncoupled to light) dispersion curves are also shown. Reproduced from [21].

Increasing the scattering rate therefore causes a transition between undamped polariton states and heavily damped polariton states at $\gamma_{\mathrm{x}} \simeq \gamma_{\mathrm{x}}^{\mathrm{cr}}$. This is illustrated in figure 1.2 which plots the transverse solutions to a classical polariton model.

Spatial dispersion and Additional Boundary Conditions (ABCs)

Spatial dispersion of the excitonic energy levels occurs due to the confinement of the exciton wavefunction at the interface of the material. If the exciton translational mass can be considered to be infinite, $M_{\mathrm{x}} = \infty$, spatial dispersion is removed and the excitons are said to be "dispersionless". This is most applicable to Frenkel excitons, though some Wannier-Mott excitons can have effective masses large enough that infinite mass is a reasonable approximation. In comparison, TO-phonons do not experience spatial dispersion and the Additional Boundary Problem we are about to discuss does not apply for phonon-polaritons.

Theoretical treatment of polaritons requires knowledge of the electric and magnetic fields, **E** and **H**, inside the material in order to obtain knowledge of the polarisation field, **P**. As a result of spatial dispersion a polarisation field is associated with each polariton branch, $\mathbf{P}_i$, which can in general propagate at different frequencies. Maxwell's boundary conditions alone are not sufficient in order to determine the resulting dispersion equations, and an Additional Boundary Condition (ABC) must be imposed.

An ABC describes the polarisation field at an interface, and possibly the derivative of the field perpendicular to the interface. The general form of an ABC can be written as:

$$\mathbf{P} + \lambda \left. \frac{d\mathbf{P}}{dz} \right|_{z=0} = 0, \tag{1.5}$$

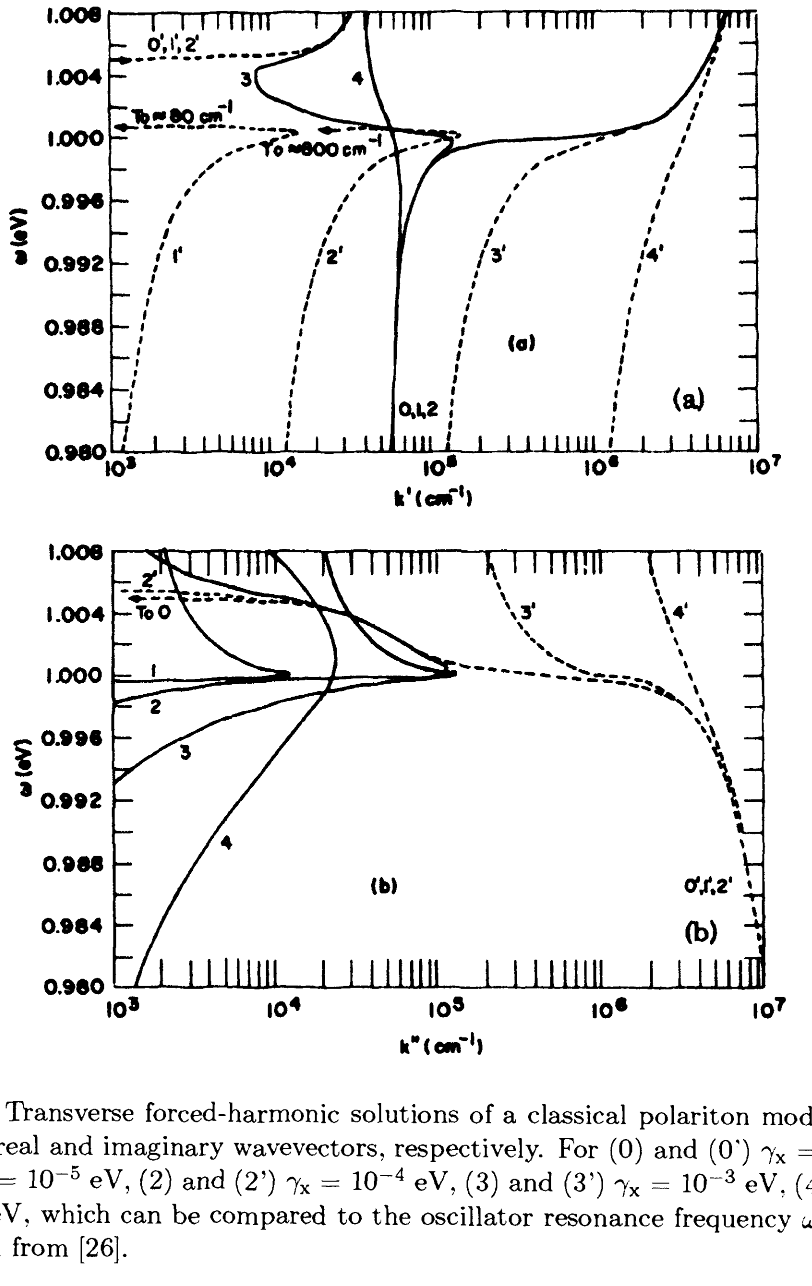

Figure 1.2: Transverse forced-harmonic solutions of a classical polariton model [26]. k' and k'' are real and imaginary wavevectors, respectively. For (0) and (0') $\gamma_x = 0$ eV, (1) and (1') $\gamma_x = 10^{-5}$ eV, (2) and (2') $\gamma_x = 10^{-4}$ eV, (3) and (3') $\gamma_x = 10^{-3}$ eV, (4) and (4') $\gamma_x = 10^{-2}$ eV, which can be compared to the oscillator resonance frequency $\omega_0 = 1$ eV. Reproduced from [26].

though there are restrictions on the choice of λ due to conservation laws [27]. The correct choice of ABC is still a bit controversial, but we will use Pekar's boundary condition, $\mathbf{P} = 0$ at the interface, for the purposes of this research.

1.1.4 Polaritons in Quantum Wells

A quantum well is a thin layer of semiconductor surrounded by thick layers of a different semiconductor with a larger band-gap. Electrons and holes confined within the well can be treated using the envelope-function method [28, 29] and described using an effective-mass equation with a confining potential determined by the band-offsets. The confinement of the charge carriers in the well quantises the motion of excitons perpendicular to the plane of the well (the *growth direction*, z-axis), but leaves them a 2D dispersion, $E_n(\mathbf{k}_{\|})$, called *subbands*, in the plane of the well. The bulk exciton binding energy, $E_{\mathrm{b}} = R^*$, increases monotonically as the well width, L, decreases, reaching a value of $4R^*$ as $L \longrightarrow 0$ assuming the well is surrounded by infinitely high barriers [30]. In true systems the barriers are finite and the exciton wavefunction is able to penetrate into the surrounding material. The binding energy hence reaches a maximum value (with an associated maximum in the oscillator strength) before dropping back to the bulk value as $L \longrightarrow 0$ [31].

For well thicknesses below the exciton Bohr radius, $L < a_{\mathrm{B}}$, the exciton is associated with a pair of electron and hole subbands, each of which is strongly confined by the well. The motion of the electrons and holes must then be treated separately. This is called the strong confinement (or electron-hole) regime. Accurate determination of the binding energy and oscillator strength requires the inclusion of additional physical effects such as heavy-light hole mixing [28], but leads to an increased ground-state binding energy [32, 33]. For wide wells, $L \gg a_{\mathrm{B}}$, we have the *weak confinement* regime. The Coulomb interactions dominates the effect of confinement on the charge carriers, and the exciton can be treated as a point particle (the center-of-mass approximation) [34, 35], which has been experimentally verified in a thin GaAs layer [36].

Polaritons in QWs can be treated semiclassically [37, 38] or quantum mechanically [39]. In contrast to bulk materials, where polaritons form from the interaction of an exciton and photon with the same wavevector $\mathbf{k}_{\mathrm{ex}}$, QW-excitons interact with a photon with the same $\mathbf{k}_{\|}$ and all possible $\mathbf{k}_{\mathrm{z}}$, leading to a density-of-states function for the radiative decay given by:

$$\begin{aligned} \rho\left(\mathbf{k}_{\|}, \omega\right) &\equiv \textstyle\sum_{k_z} \delta\left(\hbar\omega - \frac{\hbar c}{n}\sqrt{k_{\|}^2 + k_z^2}\right), \\ &= \frac{V}{\pi S}\left(\frac{n}{\hbar c}\right)^2 \frac{\hbar\omega}{\sqrt{k_0^2 - k_{\|}^2}}\theta\left(k_0 - k_{\|}\right), \end{aligned} \tag{1.6}$$

where V, S and n are the volume, surface area and index of refraction of the QW, k_0 is the wavevector of light in the QW, and $\theta(x) = 1$ for $x > 0$, $\theta(x) = 0$ for $x < 0$. Only states that lie within the photon cone, $k_{\|} < k_0$, are able to decay radiatively. Nonradiative states that lie outside the photon cone, $k_{\|} > k_0$, do not couple with light propagating along the z-axis, and are analogous to surface states.

The polariton states in QWs are denoted as L, T and Z modes depending on their polarisation vector. Taking $\mathbf{k}_{\|} = k_{\|}\hat{x}$, L-modes have $\hat{\varepsilon}\|\hat{x}$, T-modes $\hat{\varepsilon}\|\hat{y}$ and Z-modes $\hat{\varepsilon}\|\hat{z}$. Plots of the dispersion curves for these modes are given in figure 1.3. Radiative states lie to the left of the photon dispersion (dotted line) and nonradiative states to the right. The large splitting between the Z and L, T is due to the electron-hole exchange interaction [38] and is not a polariton effect. The radiative lifetime of the radiative polaritons can be calculated using Fermi's

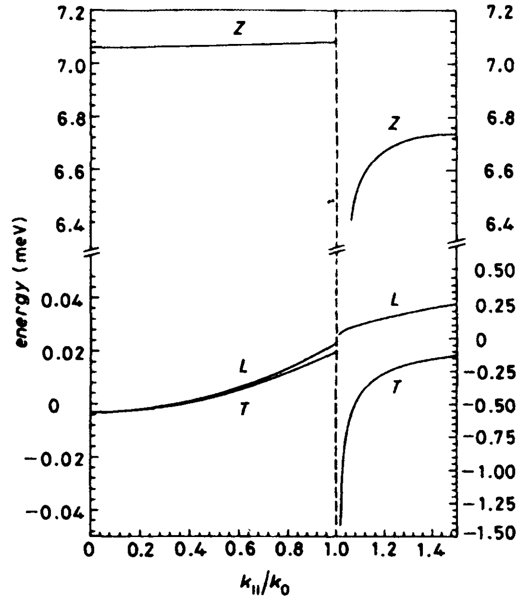

Figure 1.3: Dispersion of radiative (left) and nonradiative (right) polaritons in a 20 Åwide CuCl QW. The dashed line is the light dispersion. Reproduced from [40].

golden rule to be [41, 42]:

$$\begin{aligned}\Gamma_{\mathrm{L}}(k_{\|}) &= \frac{2\pi}{n}\frac{e^2}{m_0 c}\frac{f_{xy}}{S}\frac{k_z}{k_0},\\ \Gamma_{\mathrm{T}}(k_{\|}) &= \frac{2\pi}{n}\frac{e^2}{m_0 c}\frac{f_{xy}}{S}\frac{k_0}{k_z},\\ \Gamma_{\mathrm{Z}}(k_{\|}) &= \frac{2\pi}{n}\frac{e^2}{m_0 c}\frac{f_z}{S}\frac{k_{\|}^2}{k_0 k_z},\end{aligned} \tag{1.7}$$

where $k_z = \sqrt{k_0^2 - k_{\|}^2}$, and f_{xy} and f_z are the oscillator strengths per unit area in the corresponding direction of the polarisation vector. Figure 1.4 shows that as $k_{\|} \rightarrow 0$, the radiative width of the Z-mode vanishes, whilst those of the L and T modes converge to the same value; $2\Gamma_0 = 2\pi e^2 f_{xy}/n m_0 c S \sim 10$ ps for a GaAs/AlGaAs system.

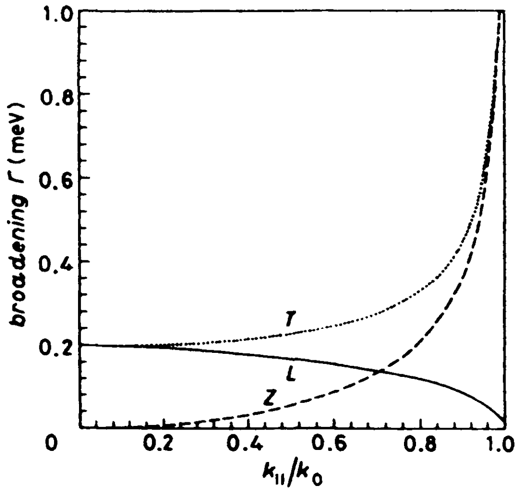

Figure 1.4: Lifetime broadening of radiative polaritons in a 20 Åwide CuCl QW. Reproduced from [40].

1.1.5 Exciton-polaritons in microcavities

Microcavities are structures designed to confine the electromagnetic field. The size and shape of a microcavity is critical; the size will determine what wavelengths of light are confined by the structure, whilst its shape will determine the direction and symmetry of the confinement. Photons inside such structures propagate in *cavity modes*, which can be highly controlled by the design of the structure. Two types of microcavities can be readily identified: planar microcavities in which the electromagnetic field is quantised only along one direction, and photonic dots in which the confinement is fully three-dimensional.

Planar microcavities

The planar microcavity is the optical analog of a QW. Confinement of light in the z-axis (growth direction) is typically achieved by adding high-reflectivity, low-loss *Distributed Bragg Reflectors* (DBRs) above and below the cavity [43]. In-plane confinement is then usually achieved only by the change in refractive index between the cavity and the surrounding air. These structures have been extensively studied and many excellent reviews are available (see, for example, [44, 45]). One of the most exciting applications of planar microcavities is the polariton laser [46, 47, 48].

For the purposes of this work we will note only a few basic features of planar microcavities, before progressing to photonic dots. Polaritons in microstructures are the result of the resonant interaction of excitons with the cavity photon modes, and are a 2D analog of bulk polaritons. Since the cavity photon modes are determined by the size and shape of the cavity, so are the cavity polariton modes. The strong coupling regime, as discussed for bulk materials, has been observed in a planar microcavity with an embedded quantum well [49] as two dips in the reflectivity spectrum, with a vacuum-field Rabi splitting of a few meV, which is considerably less than the splitting for the bulk material (about 16 meV for GaAs). However, polariton effects are generally easier to observer in microcavities than in bulk materials, despite this reduction of the Rabi splitting. This is because the requirement for *spatial coherence* in bulk materials – the coherence length of the exciton being much larger than the wavelength of light – is removed for cavity polaritons [see 40, sections 1.3 and 4.1].

Photonic dots

Photonic dots (PDs) are microcavities that confine the light modes in all three dimensions, and are the photonic analog of quantum dots. Many different theoretical treatments of such structures have been made, due in part to the variety of shapes that can be considered. Cylindrical microcavities, created by etching a planar microcavity, can be treated by decoupling the strong vertical confinement

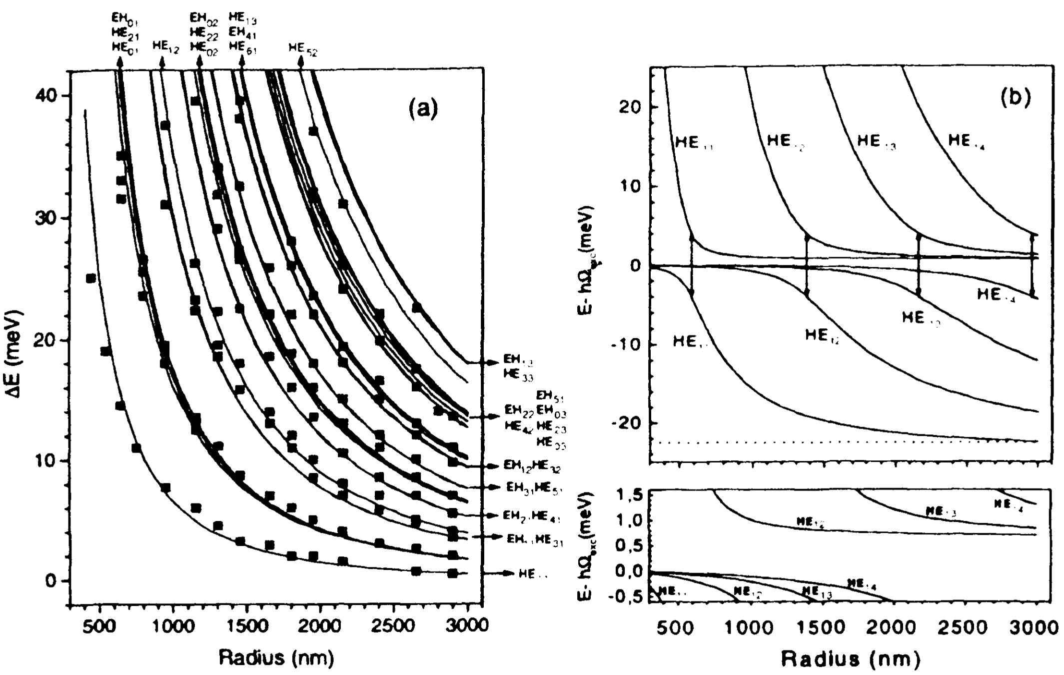

Figure 1.5: (a) Blue-shifts of the lowest-energy modes in GaAs/AlGaAs pillar microcavities with respect to the reference planar cavity, as a function of pillar radius. Points: experimental results [50]; solid lines: theoretical results including the energy dependence of the refractive index. (b) Energies of the cavity polaritons for the lowest HE modes with angular momentum $l = 1$ in pillar microcavities with different radii, measured from the exciton energy $\hbar\Omega_{\mathrm{exc}}$. Vertical arrows denote the Rabi splitting. The energy of the Fabry-Pérot mode of the planar cavity is represented by a dotted line. Lower panel: same plot on an expanded scale, showing the radiative splitting of the exciton state [51]. Reproduced from [40].

provided by the cavity's DBRs, and the lateral confinement resulting from total internal reflection at the pillar/air interface [50, 51]. The polariton frequencies are then given as a function of the height of the planar microcavity, L_c, and the radius of the pillar, a, and the blue-shifts of the polariton energies with respect to a reference planar microcavity are plotted in figure 1.5.

The simplest microcavity geometry is that of a sphere. The structure then becomes geometrically isotropic, and this decoupling becomes unnecessary. Several approaches have been made to treat the polariton optics of spherical PDs [45, 52, 53, 54, 55, 56, 57], and the recent development of the *embedding method* for electromagnetics [58] provides yet another potential scheme in which this problem could be considered. The recent treatment by Bigenwald *et al.* merits particular attention as it models spherical microcavities within a paradigm very similar to that used in this thesis [59]. The results of the different methods do not always completely agree, in contrast to the more well-known bulk and QW systems.

Using the results of Ajiki *et al.* [55] we will review the general features of polaritons in spherical microcavities. The polariton states are identified by 3 quantum numbers: the radial quantum number, n, total angular momentum, l (Ajiki *et al.* choose to denote this as J), and momentum projection, m. For $l \geq 1$ the polariton modes of the PD are transverse, with tranverse-electric (TE) and transverse-magnetic (TM) polarisations. For $l = 0$ the modes are longitudinal, and have zero frequency [60, 61, 62]. These modes are generally not of interest as they are not easily observed experimentally, and in this work we will consider the optics of $l = 1$ modes. m takes integer values between $-l$ and l, and for our purposes we will take $m = 0$.

In the bulk case the polariton frequencies are functions of wavevector, $\omega(\mathbf{k})$, but PD polaritons result from the interaction of excitons with the cavity photon modes, and $\mathbf{k}$ ceases to be a good quantum number. The polariton frequencies are functions of the dot radius, $\omega(a)$. In bulk materials the frequencies are real, but in PDs the transverse frequencies are complex due to leakage of the light out of the PD. The real part gives the energy of the spectral peak, and the imaginary part relates to the spectral width. Polariton dispersions for a CuCl PD surrounded by vacuum are plotted in figure 1.6. Only the polariton modes around the exciton resonance have been plotted, and in general another set of modes, similar to the photon modes of the cavity, should also be present.

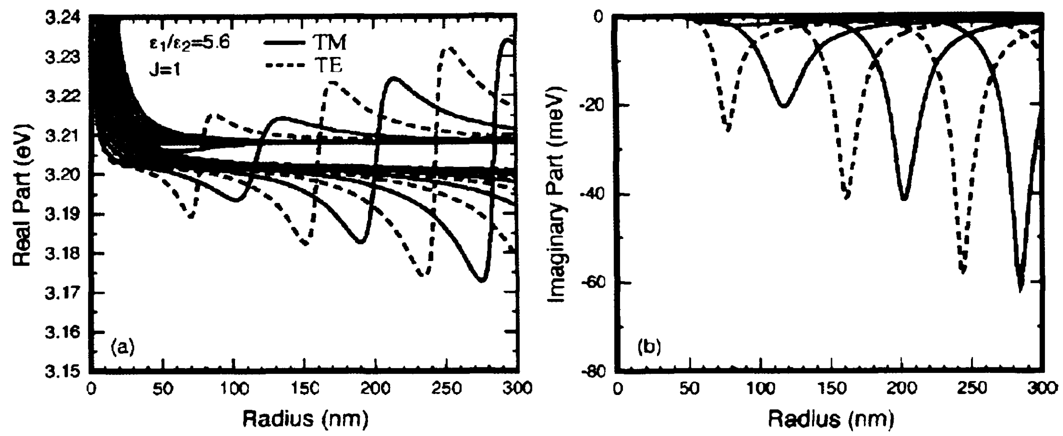

Figure 1.6: Calculated (a) real and (b) imaginary parts of the eigenenergy for $l = 1$, exciton-light coupled modes in a spherical CuCl nanocrystal. The solid and dotted lines represent the TM and TE modes, respectively. Modified from [55].

For small radii the coupling between the confined excitons and the cavity photon modes is very weak, and the polariton frequencies remain very close to the non-interacting exciton frequencies. As the radius is increased, the imaginary part starts to decrease (its modulus increases) and successively reaches a minimum for each mode, indicating a maximum in exciton-photon coupling for that mode. These peaks correspond to radii at which the wavelength of the photon mode coincides with that of the exciton.

Hanamura has shown that the decrease in the imaginary part of the frequency, and hence an increase in the radiative linewidth, goes as a^3 for small radius. His approach considers a sphere of radius which is smaller than the wavelength of light within the PD, but much larger than the exciton Bohr radius: $a_B \ll R_0 \leq \lambda$. The envelope function of the exciton is described as:

$$\Psi_{nlm}(\mathbf{R}, \mathbf{r}) = F_{nlm}(R, \theta, \phi)\Phi_0(r), \qquad (1.8)$$

where $F_{nlm}(\mathbf{R}, \theta, \phi)$ describes the center-of-mass motion, and $\Phi_0(\mathbf{r}$, of the exciton.

The boundary conditions on $\Psi_{nlm}(\mathbf{R}, \mathbf{r})$ should be applied at the "effective radius", $R = R_0 - a_B/2$, which is smaller than the true PD radius due to the finite size of the exciton [63, 64]. However, because of the size regime being considered, $\ll R_0$, the a_B factor is neglected and only R_0 is considered. The exciton-photon interaction is described using a completely resonant Hamiltonian:

$$H' = -\frac{4i}{\sqrt{V}}\Phi_0(0)R_0^{3/2}\sum_n\sum_{\mathbf{k}}\frac{E_n\hat{e}_{\mathbf{k}}\mu_{cv}}{n\sqrt{\hbar ck}}\left(a_{\mathbf{k}}b_n^\dagger - a_{\mathbf{k}}^\dagger b_n\right), \tag{1.9}$$

where $\hat{e}_{\mathbf{k}}$ is a unit polarisation vector of the photon field, μ_{cv} is the transition dipole moment between the conduction and valence bands, and $a_{\mathbf{k}}$ $(a_{\mathbf{k}}^\dagger)$ and b_n $(b_n^\dagger)$ are annihilation (creation) operators for a photon with wavevector $\mathbf{k}$ and exciton of state n, respectively.

The radiative decay rate for the lowest-energy exciton is then calculated using Fermi's golden rule to be:

$$2\gamma = 64\pi\left(\frac{R_0}{a_B}\right)^3\gamma_s, \tag{1.10}$$

where $\hbar\gamma_s$ is the decay rate at the exciton energy. This has been experimentally confirmed by Itoh *et al.* in CuCl microcrystals embedded in a NaCl matrix [65]. Figure 1.7 plots experimental data (open and closed circles) alongside solutions to equation (1.10) expressed as:

$$\frac{1}{\tau_r(a*)} = \frac{64\pi\varepsilon}{3}\left(\frac{a*}{\lambda}\right)^3\frac{\Delta E_{LT}}{\hbar}, \tag{1.11}$$

where ΔE_{LT} is the exciton LT-splitting energy, λ is the wavelength of light at the exciton resonance, ε is the background dielectric constant around the exciton energy, and $a* \equiv R$ is the effective radius of the PD.

There is therefore an R_0^3 dependence to the radiative decay rate, which is

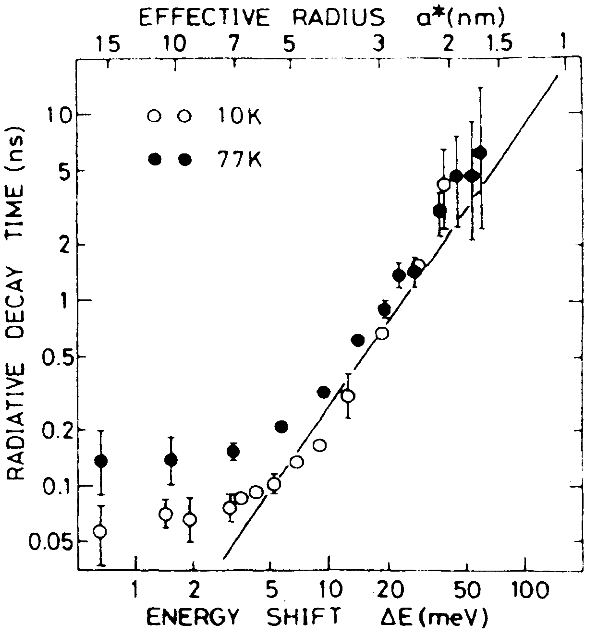

Figure 1.7: Dependence of the exciton radiative decay time on the effective radius both at 10K (open circles) and 77K (closed circles). The solid line represents theoretical values calculated with equation (1.11). Reproduced from [65].

interpreted as the volume-dependent increase of the oscillator strength. However one must take care to note the upper bound on the radii being considered: $R_0 \leq \lambda$, or else it appears that the behaviour continues for ever-increasing radius, when in fact the oscillator strength saturates at around $R_0 \sim \lambda$.

In the course of this thesis we will consider spherical structures over a range of radii as large as several wavelengths, down to the limit that the $a \to 0$. Structures in this small-radius limit are typically referred to as quantum dots rather than photonic dots, but for clarity (and brevity) we will refer to all dots, irrespective of size, as PDs.

1.2 Overview

The aim of this thesis is to add to this accumulated sum of knowledge by performing a theoretical study of polaritons in the simplest 0-dimensional geometry; a sphere. In solving the eigenmodes of a spherical nanostructure we can obtain the frequencies of polaritons resulting from the interaction of excitons with photon modes which are completely resonant with the sphere. By removing all incoherent scattering from the model we also produce a scheme in which the exciton-photon interaction is entirely coherent. The resulting dispersion curves are then classified into the weak and strong coupling regimes, in direct analogy with the same phenomena in bulk-materials. The radiative linewidth of the polariton modes are studied through the coherent distribution of the polariton energy between the excitonic and photonic components of the polariton. Finally, we identify a transition point between the weak and strong coupling regimes, similar to that studied by Tait in bulk materials several decades ago [26]. The conditions under which the transition occur are analysed in order to completely describe this phenomena in a spherical nanostructure.

Chapter 2 is the main base of this research, and covers the polariton optics of a spherical nanostructure in the absence of any spatial dispersion. A theoretical model of the polariton eigenmodes of the structure is developed, neglecting the effect of incoherent scattering in order to produce a picture of the completely coherent polariton optics of the system. This model is used to classify the polariton modes into the weak and strong coupling regimes – in direct analogy with the same concept in bulk materials – and to investigate the radiative lifetime of these modes. This is then extended in Chapter 3 to include spatial dispersion.

This forms the basis for Chapter 4, which defines the transition between the polariton regimes, and proceeds to determine the conditions under which the transition takes place. Observation of the transition point is proposed in order to confirm the theoretical treatment given here, and this section may be of particular interest to experimentalists.

A summary is given at the end of each chapter, culminating in Chapter 5 which concludes the thesis and looks to the future development of this research. A final Appendix, Chapter 6 covers supporting material.

1.3 Mathematica

Mathematica was used exclusively to produce all of the numerical results presented in this thesis. It is a fully integrated environment for technical computing, and offers numerical, algebraic and graphical facilities in a single package. Hence it was not only used to produce numerical results but also all of the figures throughout this thesis, and even aided in the algebraic derivations of the equations.

The most comprehensive source of information on Mathematica is the Mathematica Book [66]. It has been published in many versions, alongside the continual re-releases of new versions of Mathematica itself, and the reference given is for the 5th edition.

The use of Mathematica was only a matter of personal choice and there is no special requirement that Mathematica must be used to reproduce these results. However, aside from the core physics presented in this thesis, notes on specific aspects of the numerical computations involved are included to aid the reproduction of these results. In particular, section 6.3 of the Appendix discusses how features of Mathematica can be used to maintain the accuracy of numerical results, and how these results are best presented. Though these sections will be of most use to readers wishing to reproduce this work using Mathematica, they may still prove useful to readers intending to use other languages and packages.

Chapter 2

Polariton optics of a spherical PD without spatial dispersion

In this chapter we develop a model of the coherent polariton optics of a spherical nanostructure in the absence of any spatial dispersion of the excitonic resonance. Although we will discuss exciton-polaritons in the development of our model, our approach is equally valid for any dispersionless matter excitation, e.g. transverse-optical (TO) phonons. Chapter 3 will extend this model to consider the effect of spatial dispersion.

The first section will describe the model we wish to use, introduce equations we use to describe exciton-photon interaction in the PD, and the resulting polariton dispersion equations. These are the fundamental equations which describe the polariton optics of the system, and their solutions are the eigenmodes of the PD. Numerical solutions will then be presented and the polariton modes shown therein will be classified into strong and weak coupling regimes, in analogy with the bulk polariton case. Section 2.4 then examines the radiative lifetime of the polariton

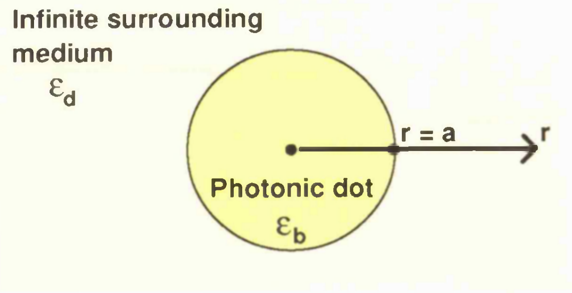

Figure 2.1: An illustration of the PD and surrounding material being modelled.

modes. We will assume that the energy within a mode is distributed coherently between its two polariton branches, in order to maintain our picture of completely coherent polariton optics. The main subject of this section is the asymptotic behaviour of the radiative lifetime with relation to radius. Finally, section 2.5 will summarise the results of this chapter.

2.1 The model

The aim of this model is to find the eigenfunction solutions for the polariton modes of a spherical nanostructure. The structure is modelled as a single sphere surrounded by an infinite expanse of another material. A simple schematic is shown in figure 2.1. The PD is assumed to be made from a semiconductor which is homogeneous and optically isotropic, with no magnetic susceptibility. The surrounding material is also assumed to be homogeneous and optically isotropic, and may be a liquid, gas or even vacuum.

We consider the exciton to be a single-point particle generated within our sphere and travelling freely around it. The internal structure of the exciton, i.e. the relative motion of the electron and hole, is unaffected by the boundary of the sphere and it behaves as though the exciton were in a bulk material. This is the so-called *weak confinement regime.* This regime is applicable as long as the radius does not approach or fall below the exciton Bohr radius, a_x. When the radius is below the Bohr radius, the *strong confinement regime*, the exciton is "squashed" into the sphere, and the relative e-h motion is affected. Although we will consider spheres of any radius, we will model the exciton in the weak confinement regime regardless of its size.

As discussed in the previous chapter, structures of various sizes are currently being studied both experimentally and theoretically. These can be broadly classified into quantum dots (QDs) which have radii much less than the wavelength of light within the material, $a \ll \lambda$, and photonic dots (PDs) which have radii greater than the wavelength of light, $a > \lambda$. The model developed in the following sections is equally applicable to QDs as PDs – though the a_x lower limit must be remembered – and a very broad range of radii will be considered in this work. In particular, spheres with radii of the order of lambda, $a \sim \lambda$, which can be called "small photonic dots", are of particular interest. For simplicity the sphere being modelled will be referred to throughout this thesis as a PD, regardless of its radius.

2.1.1 Exciton-photon interaction

Exciton-photon interaction is described by the set of macroscopic polariton equations for the resonantly interacting light field **E** and excitonic polarisation **P**, given by [13]

$$\begin{aligned} &\frac{\varepsilon_b}{c^2}\frac{\partial^2}{\partial t^2}\mathbf{E}(\mathbf{r},t) + \mathrm{curl}\,\mathrm{curl}\,\mathbf{E}(\mathbf{r},t) = -\frac{1}{\varepsilon_0 c^2}\frac{\partial^2}{\partial t^2}\mathbf{P}(\mathbf{r},t), \\ &\left[\frac{\partial^2}{\partial t^2} + \gamma_{\mathrm{x}}\frac{\partial}{\partial t} + \omega_{\mathrm{T}}^2 - \frac{\hbar\omega_{\mathrm{T}}}{M_{\mathrm{x}}}\nabla^2\right]\mathbf{P}(\mathbf{r},t) = \varepsilon_0\varepsilon_{\mathrm{b}}\omega_{\mathrm{p}}^2\mathbf{E}(\mathbf{r},t). \end{aligned} \tag{2.1}$$

Here ε_b is the high frequency background dielectric constant of the optically-isotropic semiconductor, ω_p is the polariton Rabi frequency, $\hbar\omega_\mathrm{T}$ is the exciton energy, M_x is the effective translational mass of the exciton, and γ_x is the rate of incoherent scattering of excitons.

Dispersionless excitons

Excitons are considered to be "dispersionless" if they have such a large effective mass, M_x, that the effect of spatial dispersion is negligible. This is most applicable to Frenkel excitons (which typically have an effective mass in the region of $5 - 100\ m_e$ [67, 68]) though some Wannier-Mott excitons can also apply. For the purposes of this chapter only dispersionless excitons will be considered, and an extension of the model to include spatial dispersion is left to Chapter 3.

Neglecting the spatial dispersion term, $\frac{\hbar\omega_\mathrm{T}}{M_\mathrm{x}}$, for the transverse ($\mathrm{div}\,\mathbf{E} = 0$) polariton waves of frequency ω and wavevector $\mathbf{k}$ in bulk materials, equations (2.1) yield

$$\frac{k^2c^2}{\omega^2} = \varepsilon(\omega) = \varepsilon_b\left[1 + \frac{\omega_p^2}{\omega_T^2 - i\omega\gamma_\mathrm{x} - \omega^2}\right], \tag{2.2}$$

while the longitudinal mode ($\mathrm{curl}\,\mathbf{E} = 0$) is characterised by $\omega_\mathrm{L} = \sqrt{\omega_\mathrm{T}^2 + \omega_\mathrm{p}^2}$.

Coherent polariton optics

Throughout this chapter incoherent scattering will be neglected, i.e. $\gamma_\mathrm{x} = 0$ in equation (2.2). As we demonstrate below, for the photonic dots we are dealing with, the optical lifetime of PD photons is short – in a sub-picosecond time scale – so that the "optical evaporation" of PD polaritons is rather effective [69, 70], and

$\mathrm{Im}\{\omega^{\mathrm{pol}}\}$ is usually much larger than γ_{x}. Thus, in further analysis we neglect the γ_{x}-terms in equations (2.1) and (2.2). This means that only coherent processes are occurring within our simulations, producing the "coherent polariton optics" of the system. It serves to clarify the source of the results, and makes the interpretation of the underlying physics clear.

2.1.2 Dispersion equations

For a spherical photonic dot, the PD polariton (quasi-) eigenstates are the solutions of equations (2.1), written in spherical co-ordinates and satisfying the boundary conditions for the light field. Two Maxwellian boundary conditions refer to the spherical surface at $r = a$ (a is the PD radius) and require the continuous behaviour of the tangential components of the electric, $\mathbf{E}_{\tau}$, and magnetic, $\mathbf{H}_{\tau}$, fields. The third boundary condition requires the light field at $r \to \infty$ to have an outgoing part only (no incoming field). Note that this third boundary condition causes the PD polariton eigen-frequencies, $\omega = \omega^{\mathrm{pol}}$, to be complex even when the incoherent scattering is neglected, i.e. $\gamma_{\mathrm{x}} = 0$. A full derivation of the following dispersion equations is given in the Appendix (section 6.1).

For the transverse light field ($\mathrm{div}\,\mathbf{E} = 0$), the PD polariton dispersion equations are given by [71, 72]

$$j_l(k_1 a) H_l^{(1)'}(k_2 a) - h_l^{(1)}(k_2 a) J_l'(k_1 a) = 0, \tag{2.3}$$

for the TE modes, and

$$\varepsilon j_l(k_1 a) H_l^{(1)'}(k_2 a) - \varepsilon_{\mathrm{d}} h_l^{(1)}(k_2 a) J_l'(k_1 a) = 0, \tag{2.4}$$

for the TM modes. Here $J_l(z) = zj_l(z)$ and $H_l^{(1)}(z) = zh_l^{(1)}(z)$, where $j_l(z)$ and $h_l(z)$ are spherical Bessel and Hankel functions of the first kind; $k_1 = k_1(\omega) = \omega\sqrt{\varepsilon}/c$, where $\varepsilon = \varepsilon(\omega)$ is given by equation (2.2); $k_2 = k_2(\omega) = \omega\sqrt{\varepsilon_\text{d}}/c$, where ε_d is the constant dielectric permittivity of the material surrounding the sphere. The dispersion equations (2.3) and (2.4) are similar to those discussed in [73] for PDs without excitonic resonance. The subscript l refers to the angular momentum of the modes, which are frequency degenerate with respect to the momentum projection quantum number, m.

In this work only modes with the lowest possible angular momentum number, $l = 1$, [60, 61, 62] (TE_1 and TM_1) will be considered. For $l = 1$, the PD polariton dispersion equations (2.3) and (2.4) reduce to

$$k_1 a = \arctan\left[\frac{k_1 k_2^2 a}{ik_1^2 k_2 a - k_1^2 + k_2^2}\right] + n\pi, \tag{2.5}$$

for the TE_1 modes, and

$$k_1 a = \arctan\left[\frac{-ik_1 a[k_1^2 k_2^2 a^2 + (1 - ik_2 a)(k_2^2 - k_1^2)]}{k_1^2 k_2^3 a^3 + (k_2 a + i)(k_1^2 - k_2^2)}\right] + n\pi, \tag{2.6}$$

for the TM_1 modes. Here n is the energy (radial) quantum number; $n \geq 0$ for TM modes, $n \geq 1$ for TE modes.

Dimensionless parameters

In the following analysis we will frequently use dimensionless, normalised variables. The natural frequency scale for our model is that of the transverse exciton frequency, ω_T, and all frequencies are scaled to this; polariton frequency $\tilde{\omega} = \omega/\omega_\text{T}$, and Rabi frequency $\tilde{\omega}_\text{p} = \omega_\text{p}/\omega_\text{T}$. Since these frequencies can be expressed as energies, the same normalisation is used for all energy scales including, for example, the radiative linewidth, $\tilde{\Gamma} = \Gamma/\omega_{\mathrm{T}}$. The PD radius is scaled to the wavelength of light within the PD; $\tilde{a} = \sqrt{\varepsilon_b}\omega_{\mathrm{T}} a/c$. This makes it easier to identify and interpret physical phenomena arising from the resonant interaction of the light field with the PD, as they will occur at radii which are multiples of $\pi/2$. Finally, the dielectric permittivity is normalised to the background dielectric permittivity inside the PD, ε_{b}, and we define the ratio of the background dielectric constants outside and inside the dot as $\tilde{\varepsilon} = \varepsilon_{\mathrm{d}}/\varepsilon_{\mathrm{b}}$.

We can substitute these dimensionless parameters into the dispersion equations to put them in the form:

$$\tilde{\omega}\tilde{a} = \arctan\left[\frac{\tilde{\omega}\tilde{a}\tilde{\varepsilon}}{i\tilde{\omega}\tilde{a}\sqrt{\tilde{\varepsilon}} - 1 + \tilde{\varepsilon}}\right] + n\pi, \tag{2.7}$$

for the TE$_1$ modes, and

$$\tilde{\omega}\tilde{a} = \arctan\left[\frac{-i\tilde{\omega}\tilde{a}[\tilde{\omega}^2\tilde{a}^2\tilde{\varepsilon} + (1 - i\tilde{\omega}\tilde{a}\sqrt{\tilde{\varepsilon}})(\tilde{\varepsilon} - 1)]}{\tilde{\omega}^3\tilde{a}^3\tilde{\varepsilon}^{3/2} + (\tilde{\omega}\tilde{a}\sqrt{\tilde{\varepsilon}} + i)(1 - \tilde{\varepsilon})}\right] + n\pi, \tag{2.8}$$

for the TM$_1$ modes. Though this form of the dispersion equations is no simpler than that given by equations (2.5) and (2.6), it serves to more clearly illustrate the nature of the results we obtain from them; polariton frequencies as a function or radius, $\tilde{\omega}(\tilde{a})$.

2.1.3 Obtaining numerical solutions

The materials of the PD and surrounding medium of a specific being modelled determines the values of $\tilde{\varepsilon}$ and $\tilde{\omega}_{\mathrm{p}}$. For a specific PD the radius, $\tilde{a}$, might also be set, but here the radius will be used as a parameter to plot the dispersion curves of the polariton frequencies, $\tilde{\omega}(\tilde{a})$. The eigenmode solutions can therefore be considered to lie within a 3D solution space consisting of radius, $\tilde{a}$, and the real and imaginary parts of the polariton frequencies, Re($\tilde{\omega}$) and Im($\tilde{\omega}$).

A priori we know that Re($\tilde{\omega}$) must not be negative, and Im($\tilde{\omega}$) must not be positive. The former corresponds to waves travelling in the opposite radial direction, i.e. towards the center of the PD instead of away from it. Similarly, the latter corresponds to waves leaking into the PD from outside, which is impossible since we only have an outgoing wave. Since we are considering the interaction of photons and excitons, we can expect – even without resorting to the published literature – that modes will exist around the exciton resonance, $\tilde{\omega} = 1$, but how close is unknown.

The Mathematica function FindRoot is extremely useful in searching for the roots to the dispersion equations. It will aim to find the root of a given equation using specified starting point. An example command could look like:

```
In:= FindRoot[f[x]==0,x,0]
```

This would attempt to find the solution $f(x) = 0$ starting at $x = 0$. In general terms, the gradient at the point is taken, a "step" taken "downhill", and the process repeated until a minima is found. In this case the size of the step is automated, as discussed in the Mathematica Book's section on "Unconstrained Optimisation". FindRoot is not limited to using real numbers and so can be used to find the complex frequency solutions, however it is restricted to discrete numerical operations. The arguments used in FindRoot, including the starting point, can have infinite precision, but the results cannot (see Appendix 6.3.2 for a discussion of accuracy and precision in Mathematica). The FindRoot option

"WorkingPrecision" is set to "MachinePrecision" by default, and all output from the function will be given to this degree of accuracy. However, WorkingPrecision (along with "AccuracyGoal" and "PrecisionGoal") can be set to higher values in order to obtain more accurate results.

For a first calculation, the starting points, or *guesses*, used to search for solutions can be spread throughout the solution space. A linear spread in the real domain and an exponential spread in the imaginary domain is recommended. However, this brute force approach is inefficient, and in general will not yield a full set of solutions. It is still possible for entire areas of solutions to be missed.

A similar but more comprehensive technique is to take *complex slices* through the solutions space. Although we want to find the solutions of the dispersion equations, the values of the dispersion equations away from the roots can help indicate where those roots lie. In other words, it is beneficial to examine the topography of the solution space. However, this produces a 4D solution space: $\tilde{a}$, $Re(\tilde{\omega})$, $Im(\tilde{\omega})$, $f[\tilde{\omega}, \tilde{a}]$, where f is the dispersion equation for the relevant modes, i.e. equation (2.3) or (2.4). Visually displaying a 4D space is extremely difficult, so this is simplified by considering only a single value of the radius, i.e. taking a slice through the solution space and plotting $f[\tilde{\omega}, \tilde{a}]$ over a complex plane of frequencies.

An example complex slice solution for TE_1 modes at $\tilde{a} = 5$ is shown in figure 2.2. The polariton mode solutions lie at $\mathrm{Abs}(f[\tilde{\omega}, \tilde{a}]) = 0$ and can clearly be identified as the minima of this plot, lying at the center of the red "dots". Whilst interpreting this figure it should be noted that the topology of the complex plane is plotted only within a narrow band of values of the function near to zero; $0 \leq \mathrm{Abs}(f[\tilde{\omega}, \tilde{a}]) \leq 0.5$. Points on the plot which have values above this maximum are plotted at the maximum value, creating the broad blue areas of the plot.

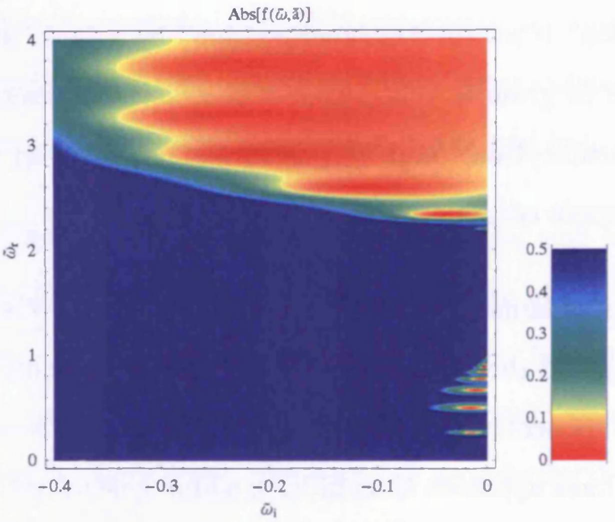

Figure 2.2: A *complex slice* contour plot of the absolute value of the TE_1 dispersion equation. The polariton modes can be identified as $\mathrm{Abs}(f[\tilde{\omega},\tilde{a}]) = 0$, and hence appear in the figure within the red "dots". The simulation parameters are $\tilde{\omega}_\mathrm{p} = 1.95$ and $\tilde{\varepsilon} = 0.52$, corresponding to TO-phonon-polaritons in a LiF PD surrounded by vacuum.

Such complex slices serve two purposes. Firstly, they are a good way to visually identify regions of the complex plane in which solutions reside, and allow guesses for FindRoot to be chosen accordingly. Secondly, a more detailed plot helps to check that FindRoot has been able to find all the expected solutions.

However it must be stressed that, even using the methods discussed here, there is no guaranteed method for obtaining a full set of numerical solutions. Only through the algebraic analysis of the dispersion equations can we be certain that all of the solutions have been found.

2.2 Classification of the PD modes

A variety of different types of mode result from solutions of the dispersion equations. They can be classified according to their properties and behaviour, which in turn result from the underlying physics of the mode in question. Classifying modes allows us to group modes together according to these attributes, and allows us to discuss the underlying physics of specific modes or groups of modes quickly and clearly.

2.2.1 Resonant photon modes

This simplest possible solution to the dispersion equations is to remove the interaction with the excitonic resonance altogether, i.e. $\tilde{\omega}_{\mathrm{p}} = 0$. This produces the pure photonic modes resonant with the sphere. The photon eigen-frequencies $\tilde{\omega}_n^0$ against the dot radius $\tilde{a}$, calculated with equations (2.5)-(2.6) for $\tilde{\varepsilon} = 1/2$ are plotted in figure 2.3.

For a given PD radius $\tilde{a}$, the photon n-eigen-harmonics can be interpreted in terms of the interference pattern of the order n, which arises due to the partial reflection of the light field at the PD spherical boundary. The contrast of the interference pattern as well as the radiative lifetime of PD photons, $\tau_n = -1/(2\mathrm{Im}\{\omega_n^0\})$, strongly depend upon $\tilde{\varepsilon}$, i.e. upon the jump of the dielectric constant from ε_{b} at $r \leq a$ to ε_{d} at $r > a$.

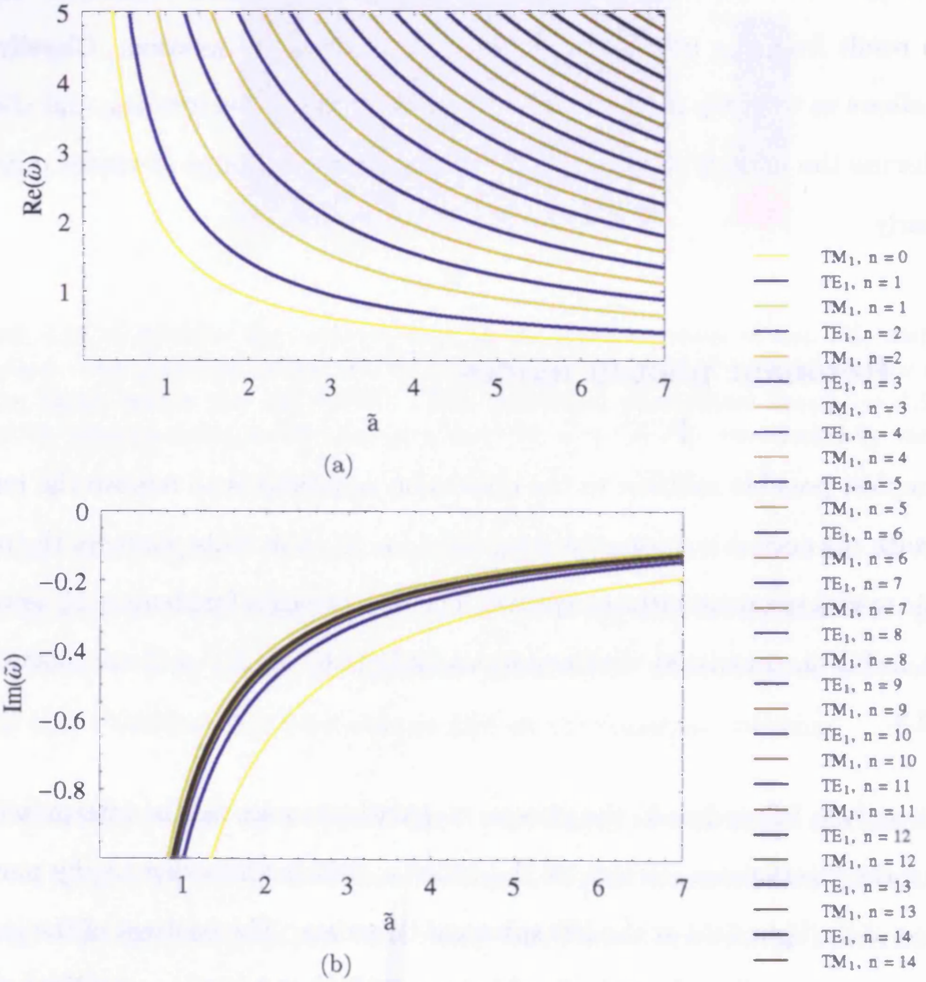

Figure 2.3: The dependence of the frequency of the (a) real, and (b) imaginary parts of the complex photon mode frequencies against the PD radius. TM$_1$ modes are shown in yellow, TE$_1$ modes in blue. $\tilde{\omega}_{\mathrm{p}} = 0$ and $\tilde{\varepsilon} = 0.5$.

2.2.2 Polariton modes

While the polariton dispersion in bulk semiconductors, $\tilde{\omega}^{\mathrm{pol}}_{\mathrm{bulk}} = \tilde{\omega}^{\mathrm{pol}}_{\mathrm{bulk}}(\mathbf{k})$, deals with the dependence of the polariton frequency against the polariton wavevector $\mathbf{k}$ [1, 3, 26, 74], the PD polariton dispersion refers to the PD-radius dependence, $\omega^{\mathrm{pol}}_{n} = \omega^{\mathrm{pol}}_{n}(a)$. Similar to the former case, when for a given $\mathbf{k}$ only two initial eigenstates (photon $\mathbf{k}$ and exciton $\mathbf{k}$) couple each other, in the spherical PD of a given radius a only two energy states (the photon mode ω^{0}_{n}, and the exciton at ω_{T}) interact resonantly and independently of the other energy states. This can easily be illustrated by equations (2.5) and (2.6) where the energy number n appears on the right-hand-side of the equations and labels the pairs of the resonantly interacting PD states. If the maximum number of the energy states we examine is N, the factor N degeneracy should be attributed to the non-dispersive exciton state. In this case the resonant exciton-photon interaction removes the degeneracy of the initial exciton term even in the limit of weak exciton-photon coupling (see figure 2.5), and a single non-degenerate exciton resonance is only recovered if exciton-photon interaction is excluded entirely.

In the presence of the dipole-active dispersionless exciton state with frequency $\tilde{\omega}_{\mathrm{T}} = 1$, the PD photon frequencies $\tilde{\omega}^{0}_{n}$ no longer characterise the true eigenstates, due to the resonant exciton-photon interaction. Within the completely coherent picture of exciton-photon coupling ($\gamma_{\mathrm{x}} = 0$), the uncoupled photon and exciton states are replaced by PD polariton eigenwaves. In this case the dispersion equations (2.3)-(2.4) yield the PD polariton eigen-frequencies $\tilde{\omega} = \tilde{\omega}^{\mathrm{pol}}_{n}(\tilde{a})$. By analysing how the topology of the PD polariton dispersion arises from the initial exciton and photon terms, $\tilde{\omega}_{\mathrm{T}}(\tilde{a}) = 1$ and $\tilde{\omega}^{0}_{n}(\tilde{a})$, and develops with increasing Rabi frequency $\tilde{\omega}_{\mathrm{p}}$, we distinguish two limits of exciton-photon interaction in PDs: the weak (small

$\tilde{\omega}_{\mathrm{p}}$) and strong (large $\tilde{\omega}_{\mathrm{p}}$) coupling regimes.

Weak coupling regime

The dispersion curves of the polariton modes of the sphere, calculated with equations (2.3) and (2.4), are illustrated in figure 2.4 for the weak coupling limit. The interaction between the photon and exciton does not lead to any drastic topological changes of the PD polariton dispersion curves in this regime. The PD polariton dispersion curves can naturally be classified in terms of photon-like, $\tilde{\omega}_n^{\mathrm{pol}} = \tilde{\omega}_n^{\gamma}$, and exciton-like $\tilde{\omega}_n^{\mathrm{pol}} = \tilde{\omega}_n^{x}$ polariton branches: $\tilde{\omega}_n^{\gamma}(\tilde{a})$ and $\tilde{\omega}_n^{x}(\tilde{a})$ are nearly identical to $\tilde{\omega}_n^{0}(\tilde{a})$ and $\tilde{\omega}_{\mathrm{T}}(\tilde{a}) = 1$, respectively. The most significant change in the dispersion curves occurs in the region of the resonant crossover between the PD photon and exciton eigen-frequencies, which occurs when $\mathrm{Re}\{\tilde{\omega}_n^{0}(\tilde{a} = \tilde{a}_n)\} = 1$. This deviation is most clearly seen in the fine structure of the exciton-like modes, which is illustrated in figure 2.5. The photon- and exciton-like polariton dispersion branches thus can be interpreted as $\tilde{\omega}_n^{0}(\tilde{a})$ and $\tilde{\omega}_{\mathrm{T}}(\tilde{a})$, respectively, slightly deformed near $\tilde{a} = \tilde{a}_n$.

The condition $\mathrm{Re}\{\tilde{\omega}_n^{0}(\tilde{a})\} = 1$ yields;

$$\tilde{a}_n \simeq \begin{cases} (n+1/2)\,\pi,\ (n = 0, 1, 2, \ldots) & \text{for } \mathrm{TM}_1\,(\tilde{\varepsilon} < 1) \text{ and } \mathrm{TE}_1\,(\tilde{\varepsilon} > 1), \\ n\pi,\ (n = 1, 2, \ldots) & \text{for } \mathrm{TM}_1\,(\tilde{\varepsilon} > 1) \text{ and } \mathrm{TE}_1\,(\tilde{\varepsilon} < 1). \end{cases} \tag{2.9}$$

For the PD radius $\tilde{a} \simeq \tilde{a}_n$, a negative imaginary part of the exciton-like n-polariton eigen-harmonics, $\mathrm{Im}\{\tilde{\omega}_n^{x}\}$, has a local minimum, as shown in figure 2.5(b). In this region the excitonic state resonates with its corresponding PD photon eigen-harmonic, and can more effectively decay into the bulk photon modes.

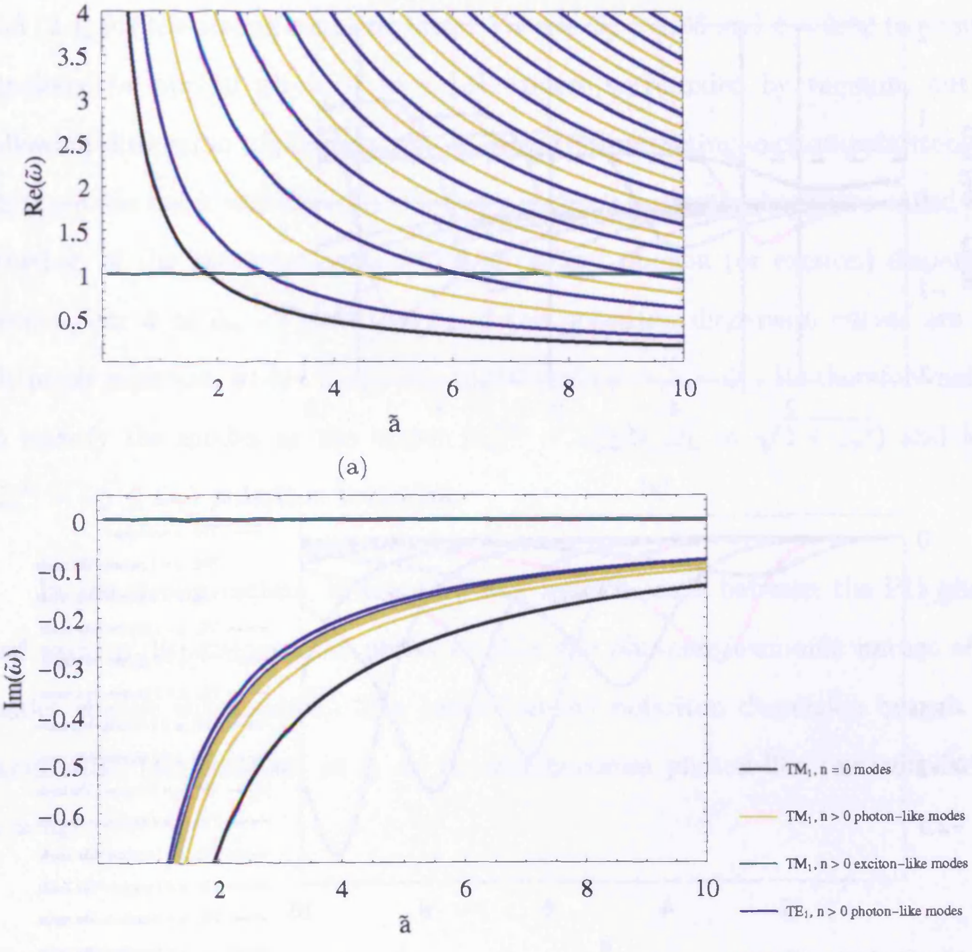

(a)

(b)

Figure 2.4: The (a) real, and (b) imaginary parts of the complex PD polariton eigenfrequencies in the weak coupling regime obtained using $\tilde{\omega}_p = 0.01$ and $\tilde{\varepsilon} = 0.5$. The photon-like (exciton-like) dispersion curves are shown in blue (red) for the TE$_1$ modes, and yellow (green) for the TM$_1$ modes. The exciton-like modes around Re($\tilde{\omega}$) = 1 are so close in frequency that the plots overlap, and only the final mode to be plotted – a TM$_1$ mode – can be seen. The true structure of the exciton-like modes is more clearly seen in figure 2.5.

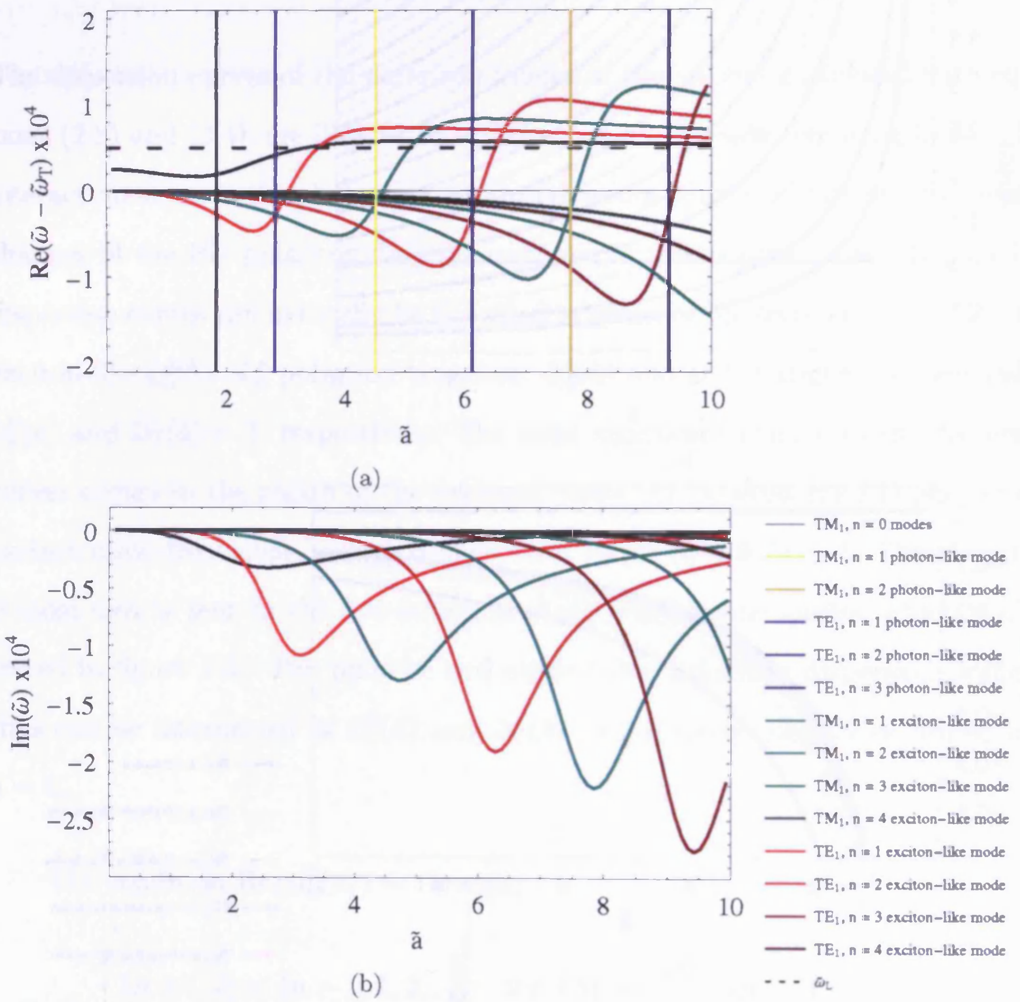

Figure 2.5: The (a) real, and (b) imaginary parts of the complex PD polariton eigenfrequencies in the weak coupling regime obtained using $\tilde{\omega}_p = 0.01$ and $\tilde{\varepsilon} = 0.5$. The frequency axes have been rescaled to clearly illustrate the fine structure of the exciton-like modes. Only a few of the lowest ordered modes have been plotted in order to maintain clarity.

Strong coupling regime

In figure 2.6 we plot the PD polariton dispersions calculated with equations (2.3) and (2.4) for the strong coupling limit. We use $\tilde{\omega}_p = 1.95$ and $\tilde{\varepsilon} = 0.52$ to simulate dipole-active optical phonons in a LiF sphere surrounded by vacuum, but the following discussion applies equally to strongly interacting exciton-polaritons. In this case one has a well-developed polariton effect: a drastic change, so-called anti-crossing, of the non-interacting PD photon and phonon (or exciton) dispersions occurs near $\tilde{a} \simeq \tilde{a}_n$. The real part of the polariton dispersion curves are now distinctly separate, with a frequency splitting $\Delta_{\mathrm{LT}} = \tilde{\omega}_{\mathrm{L}} - \tilde{\omega}_{\mathrm{p}}$. Its therefore natural to classify the modes as the upper ($\tilde{\omega}_n^{\mathrm{pol}} = \tilde{\omega}_n^U > \tilde{\omega}_{\mathrm{L}} = \sqrt{1 + \tilde{\omega}_p{}^2}$) and lower ($\tilde{\omega}_n^{\mathrm{pol}} = \tilde{\omega}_n^L \leq \tilde{\omega}_{\mathrm{T}}$) polariton branches.

In the strong regime, interaction and hybridisation between the PD photon and exciton dispersions take place, so that the photonic/excitonic nature of the modes change with radius. The lower (upper) polariton dispersion branch n is exciton-like (photon-like) at $\tilde{a} \ll \tilde{a}_n$ and becomes photon-like (exciton-like) at $\tilde{a} \gg \tilde{a}_n$.

The Fröhlich mode

For the TM_1 polariton eigen-states, in both the strong and weak coupling regimes, there is one extra mode which has no TE_1 equivalent. This is a well-known Fröhlich surface mode [71, 72], with frequency $\tilde{\omega}_S^{pol} = \tilde{\omega}_{n=0}^{pol}$ in the optical "stop band", $1 \leq \tilde{\omega}_S^{pol} \leq \tilde{\omega}_{\mathrm{L}}$. Its frequency $\tilde{\omega}_S^{pol} \rightarrow [1 + \tilde{\omega}_{\mathrm{p}}^2/(1 + 2\tilde{\varepsilon})]^{1/2}$ when $\tilde{a} \rightarrow 0$. It is shown along with its associated photon-like mode (or upper mode, depending on the regime) in figures 2.4, 2.5 and 2.6 as solid black lines.

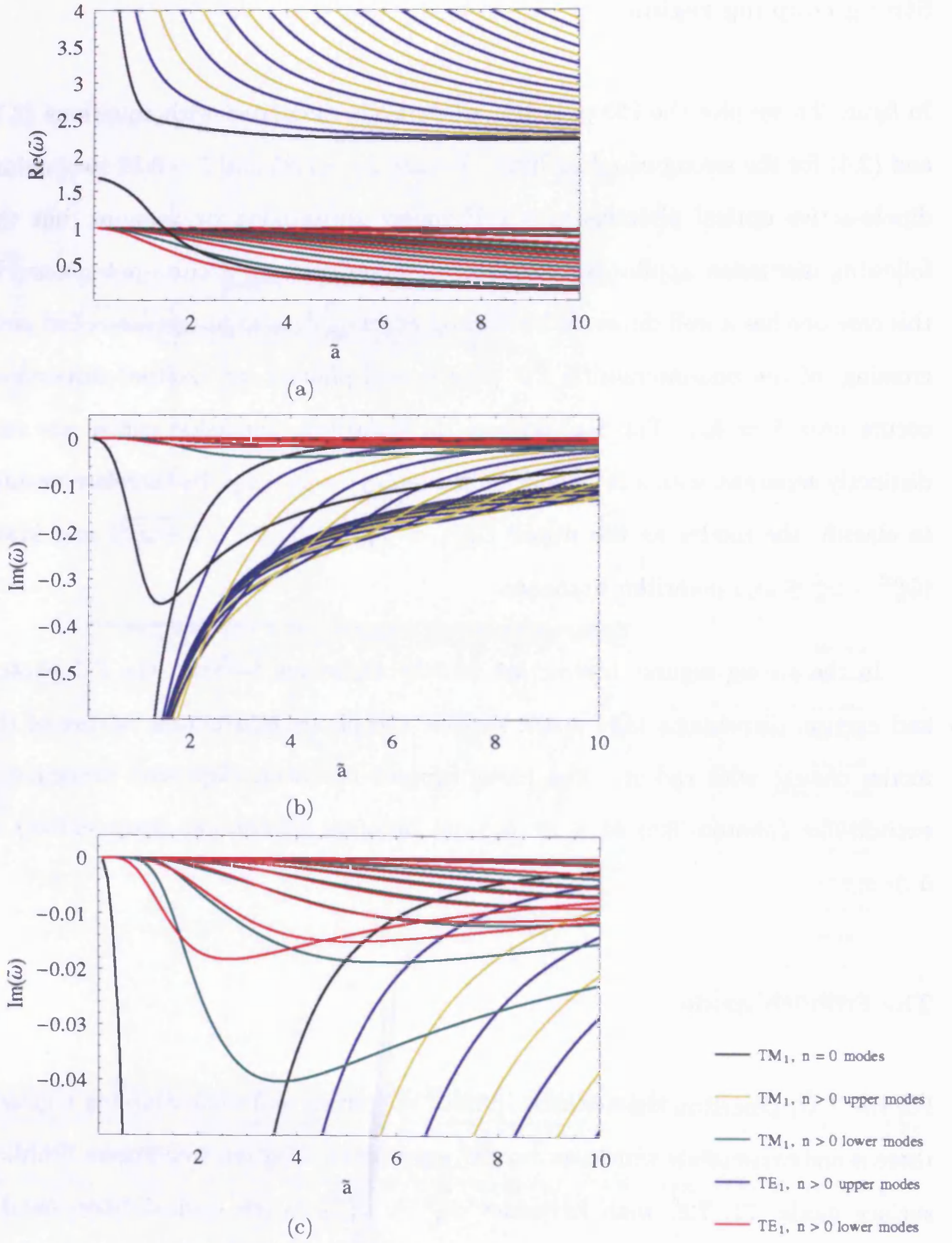

(a)

(b)

(c)

Figure 2.6: The (a) real, and (b) imaginary parts of the complex PD polariton eigenfrequencies in the strong coupling regime, obtained using $\tilde{\omega_p} = 1.95$ and $\tilde{\varepsilon} = 0.52$. In (c) the frequency axis has been rescaled to show the fine detail of the imaginary parts of the lower modes.

Complex slices have been used to prove that, using our model, the Fröhlich mode does not exist for the TE_1 case. The complex slices shown in figure 2.7 cover a section of the complex plane around the stop band for relatively low radius, $\tilde{a} = 2$. In order to help interpret these slices note that the parameters of the system are set to model our cyanine-dye J aggregate. In the TM_1 case, figure 2.7(a), the Fröhlich mode is clearly identified, along with higher-order exciton-like modes and the longitudinal mode with real frequency, $\tilde{\omega}_{\mathrm{L}}$. For the TE_1 case, the longitudinal and higher-order frequencies are present, but the Fröhlich mode is absent, as expected.

2.2.3 Characteristic complex slices

A complex slice taken over a wide area of the complex plane is a very quick method to determine what regime is present for a given radius. The characteristics of the dispersion curves for both weak and strong coupling, shown in figures 2.4 and 2.6, translate into similar features in the complex slice. This is illustrated with typical complex slices for TM_1 modes shown in figures 2.8 and 2.9.

In the weak coupling example, the wide plot is dominated by a continuous vertical string of modes, figure 2.8(a); these are the photon-like modes seen in figure 2.4. The fact that this string of modes runs straight through $\mathrm{Re}(\tilde{\omega}) = 1$ immediately indicates that the modes are in the weak coupling regime. The photon-like modes can be seen more clearly in figure 2.8(b), which has been zoomed-in to a smaller section of the complex plane, and the z-axis height re-scaled. However, the exciton-like modes are obscured because they have a very small imaginary part, and lie close to $\mathrm{Re}(\tilde{\omega}) = 1$. Figure 2.8(c) shows this region, and the modes can be compared with those shown in figure 2.4.

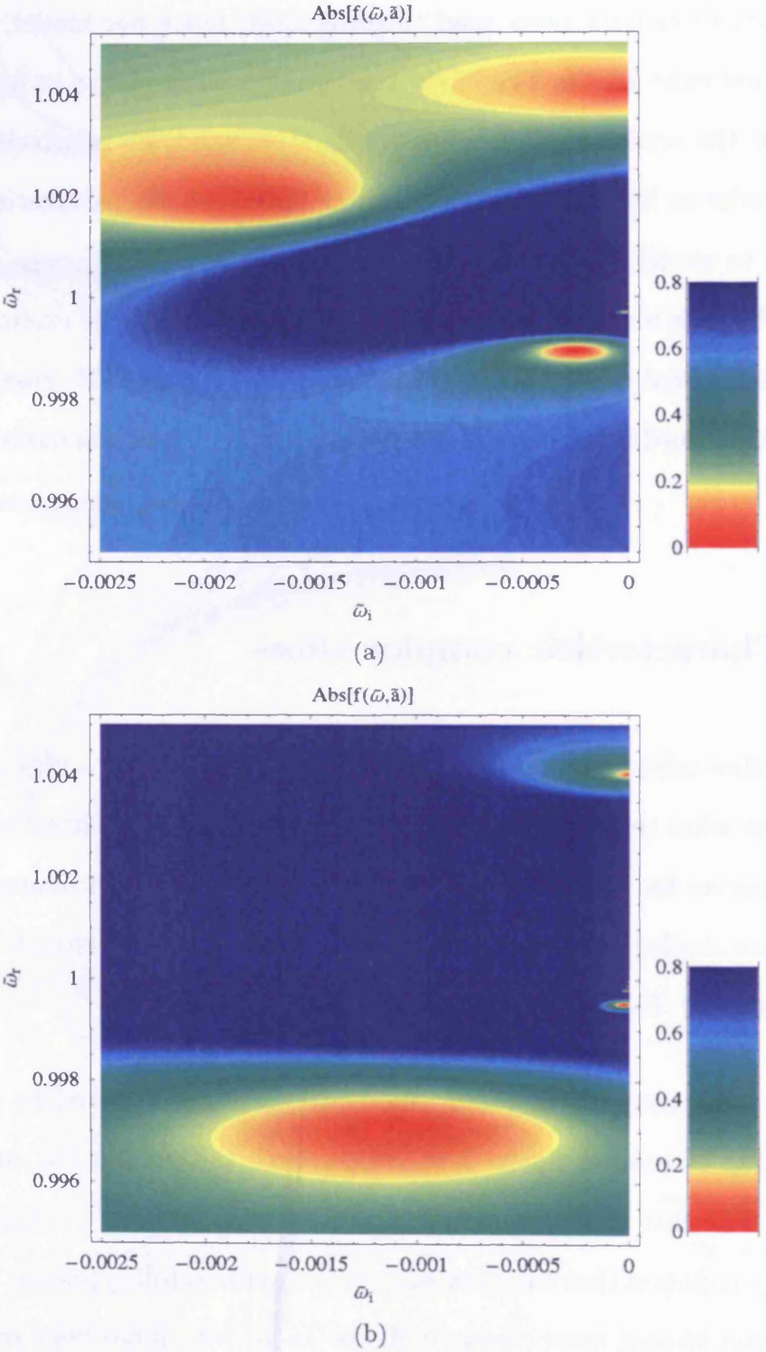

(a)

(b)

Figure 2.7: Complex slices of (a) TM_1 and (b) TE_1 modes around the stop band region. The modes observed in (a) are the Fröhlich mode (top left), higher-order exciton-like modes (lower right) and the longitudinal mode (upper right). The modes observed in (b) are exciton-like modes of order $n \geq 1$ (lower right) and the longitudinal mode (upper right).

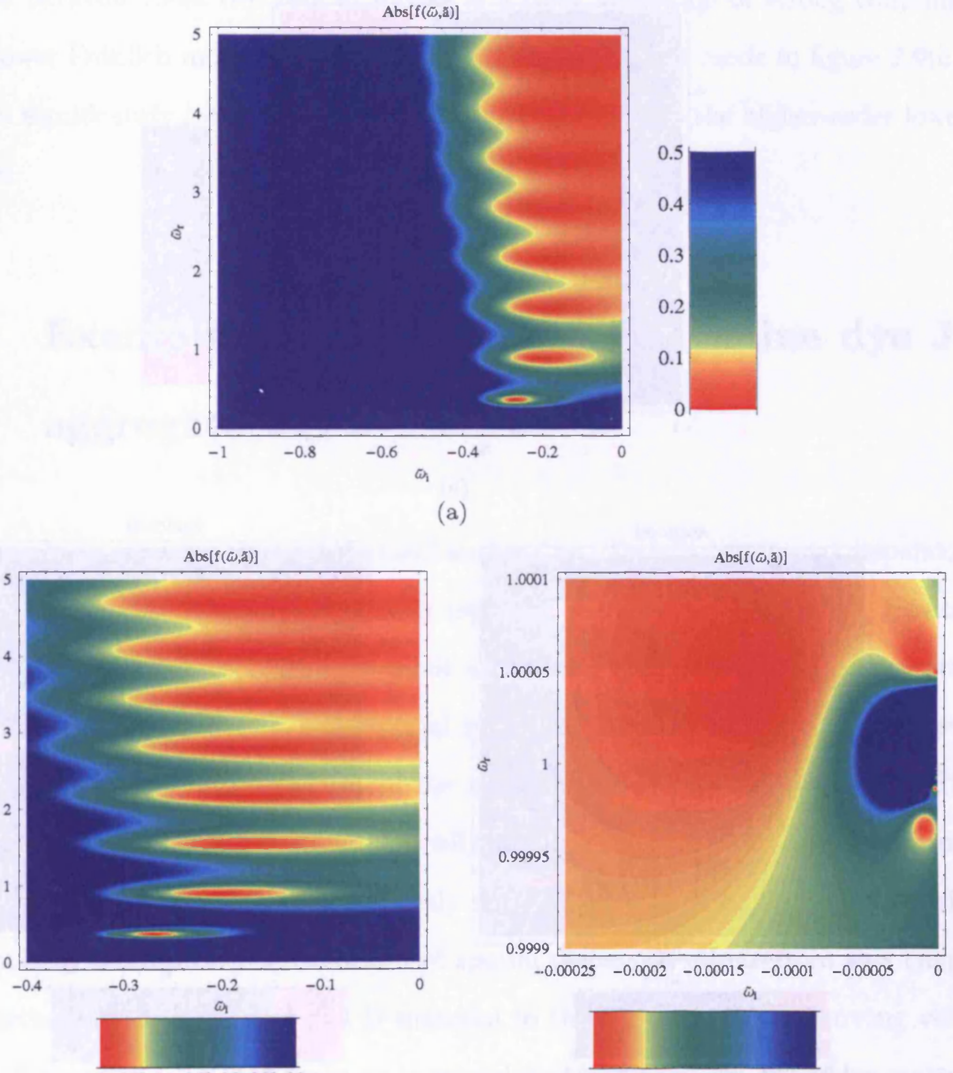

(a)

(b)

(c)

Figure 2.8: Plots of a typical complex slices for modes in the weak coupling regime. The plots illustrate (a) the topology of the complex plane over a wide range of frequency, (b) the characteristic continuous string of photon-like modes, and (c) the exciton-like modes.

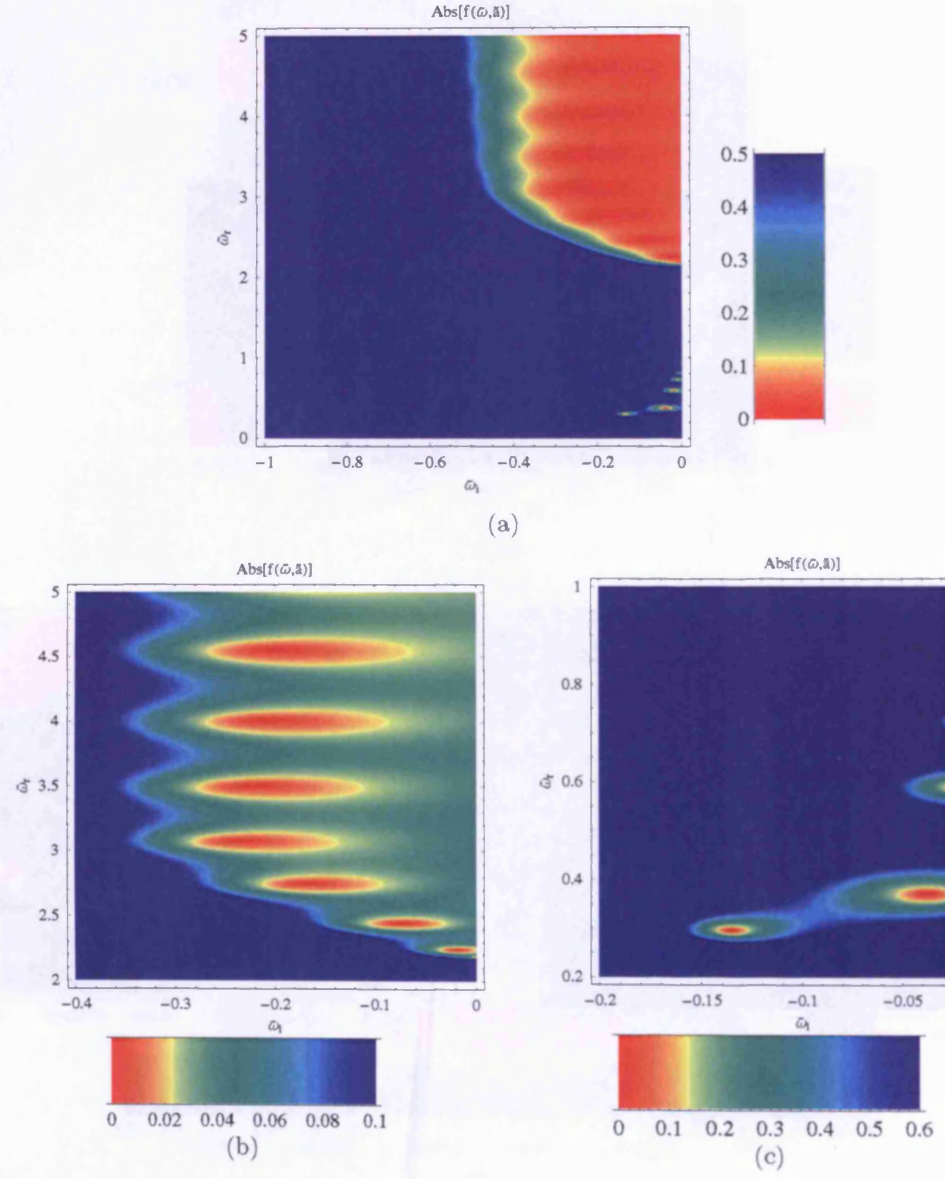

(a)

(b)

(c)

Figure 2.9: Plots of a typical complex slices for modes in the strong coupling regime. The plots illustrate (a) the topology of the complex plane over a wide range of frequency, (b) the upper modes, and (c) the lower modes.

The complex slice of the strong coupling regime, figure 2.9, shows clears sets of upper and lower modes, in direct comparison with figure 2.6, and the stop band visible between these two sets of modes is a clear indication of strong coupling. The lower Fröhlich mode can be identified as the lowest-left mode in figure 2.9(c), with a significantly lower imaginary frequency compared to the higher-order lower modes.

2.3 Example material system: a cyanine dye J-aggregate PD

The model developed above can be used to describe PDs without spatial dispersion made from any homogeneous, optically isotropic semiconductor material. Having classified the resulting modes into weak and strong coupling regimes in the previous section, a single example material system will be used throughout the rest of this chapter. The requirement of the model that the materials (both the PD and the surrounding medium) be optically isotropic limits our choice of semiconductor materials. Broadly speaking, only semiconductors with a cubic lattice will be optically isotropic. The exclusion of spatial dispersion effects from this chapter further limits our choice of PD material to those with excitons showing very high effective translational mass, or to considering non-spatially-dispersive matter excitations such as TO-phonons.

The material chosen for the PD was a cyanine dye J-aggregate. This group of materials are disordered organic semiconductors and have attracted a lot of attention in recent studies because they exhibit very large Rabi splitting between about 80 meV and 300 meV at room temperature, compared to about 5 to 10 meV

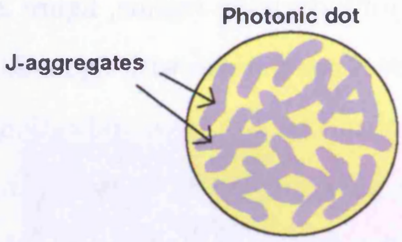

Figure 2.10: An illustration of a spherical PD made from a cyanine dye J-aggregate.

for inorganic materials [75, 76].

Although individual J-aggregates will have dipole moments directed along the length of the aggregate chain, we assume that the orientations of the aggregate chains are random, producing a PD which is optically isotropic on average. This assumption is valid because the length scale of the disorder is very small compared to λ, and is supported by experimental results [76]. Figure 2.10 illustrates such a PD and its constituent J-aggregates. It is shown with no surrounding material because we will consider – at least for the remainder of this section – that the PD is surrounded by vaccuum. The background dielectric permittivity is $\varepsilon_{\mathrm{b}} = 2.6$ [76] giving $\tilde{\varepsilon} = 0.385$. The exciton absorption line lies around 1.8 eV and Rabi splitting as high as 180 meV has been observed [77, 78], so we choose to take $\tilde{\omega}_{\mathrm{p}} = 0.09$ as a comfortable value.

Plots of the modes for the cyanine dye J-aggregate PD are shown in figures 2.11 and 2.12. The range of the plots in figure 2.12 have been chosen to illustrate the fine structure of the lower/exciton-like modes, and these plots have been restricted to $n \leq 4$ for the lower/exciton-like modes in order to maintain clarity. The crossing of the real parts of the dispersion curves, figure 2.12(a), shows that the $n = 1$ and $n = 2$ modes are within the weak coupling regime, whilst the anti-crossing of the higher-order modes show that they are in the strong coupling regime.

The change between weak and strong coupling as the mode number is increased is attributed to the increasing size of the PD leading to a greater amount of exciton-photon coupling. The intrinsic properties of the materials; the Rabi frequency, $\tilde{\omega}_{\mathrm{p}}$, and the ratio of dielectric permittivities, $\tilde{\varepsilon}$, remain the same. The unit-volume oscillator strength remains constant, but the increasing radius results in an increasing total oscillator strength. Thus, at some radius the degree of light-matter interaction becomes high enough to move from weak coupling to the strong coupling, and modes below and above this radius are in the corresponding regimes.

The transition between the weak and strong coupling regimes and the parameters which govern it are the subject of Chapter 4, and will be covered there in much greater detail.

2.4 The radiative linewidth of PD polaritons and coherent excitons

In our model the incoherent damping rates due to phonon scattering, etc. are neglected ($\gamma_{\mathrm{x}} = 0$), but the eigenfrequencies given by the dispersion equations (2.3) and (2.4) are complex. This is due to the intrinsic escape of photons from the photonic dot. In this case $\mathrm{Im}\{\tilde{\omega}_n\} < 0$, and $\Gamma_n = -2\mathrm{Im}\{\tilde{\omega}_n\}$ is the width of the mode, or the inverse optical lifetime $\tau_n = 1/\Gamma_n$ [79]. Numerical values for the radiative linewidth, Γ_n, can be calculated directly from numerical solutions of the dispersion equations discussed in the previous section. In figure 2.13 we plot Γ_n as a function of PD radius, numerically calculated for a cyanine-dye J-aggregate PD

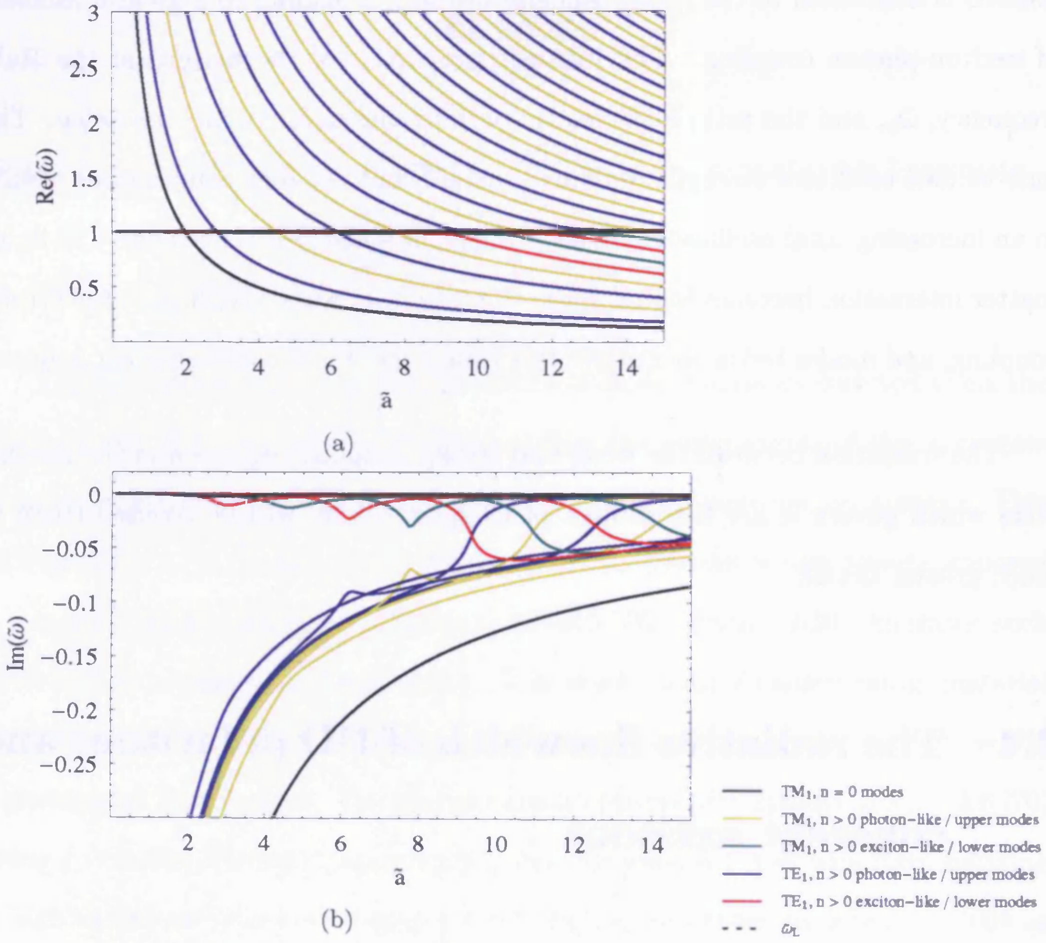

(a)

(b)

Figure 2.11: Dispersion curves of the (a) real and (b) imaginary parts of the polariton frequencies of a cyanine dye J-aggregate PD surrounded by vacuum. Although the fine structure of the real parts of the dispersion curves are not visible (see figure 2.12) the weak (strong) coupling character of the $n = 1$ and $n = 2$ ($n = 3$ and $n = 4$) modes can still be identified via the high-radius asymptotic behaviour of the real parts and the crossing (anti-crossing) behaviour of the imaginary parts of the dispersion curves. Lower modes with $n > 4$ have been omitted for clarity.

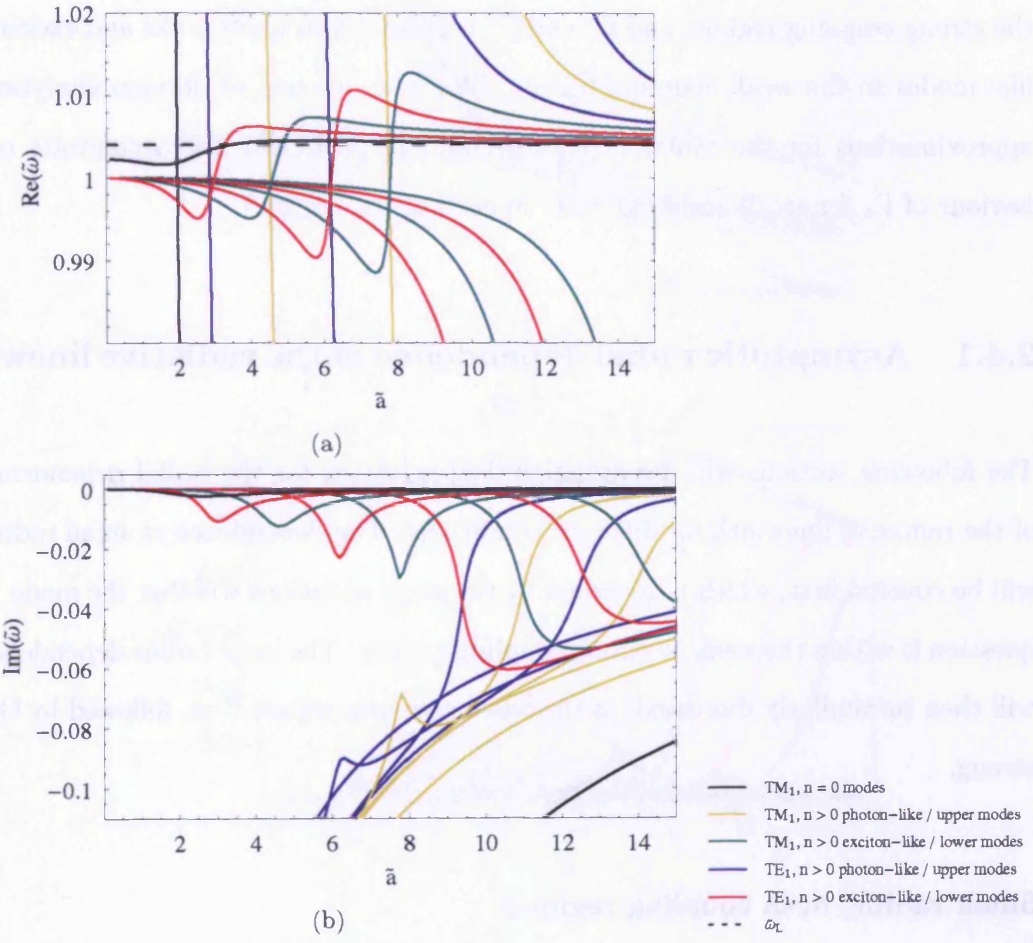

Figure 2.12: Selected portions of the dispersion curves of the polariton frequencies of a cyanine dye J-aggregate PD surrounded by vacuum. The ranges of the graphs have been chosen to illustrate the fine structure of the modes, and the lower and exciton-like modes in particular. The crossing of the $n = 1$ and $n = 2$ exciton-like modes in (a) indicate that these modes are in the weak coupling regime, whilst the anti-crossing of $n = 3$ and $n = 4$ is indicative of the strong coupling regime. Lower modes with $n > 4$ have been omitted for clarity.

surrounded by vacuum.

We classify the radiative linewidths according to their corresponding modes. Hence Γ_n^U and Γ_n^L are the radiative linewidths of upper and lower polariton modes in the strong coupling regime, and Γ_n^γ and Γ_n^x correspond to photon-like and exciton-like modes in the weak coupling regime. We now proceed to develop analytical approximations for the radiative lifetime, and in particular the asymptotic behaviour of Γ_n for small and large radii in each of the regimes.

2.4.1 Asymptotic radial dependence of the radiative linewidth

The following sections will discuss analytical solutions for the radial dependence of the radiative linewidth for different conditions. The dependence at small radius will be covered first, which is governed by the same equations whether the mode in question is within the weak or strong coupling regime. The large radius dependence will then be similarly discussed, in the weak coupling regime first, followed by the strong.

Small radius, both coupling regimes

For a small radius ($\tilde{a} \ll 1$) in both the weak and strong coupling limits, one has

$$\Gamma_n^{\gamma,U} = 2B_n\omega_{\mathrm{T}}/\tilde{a}\,, \tag{2.10}$$

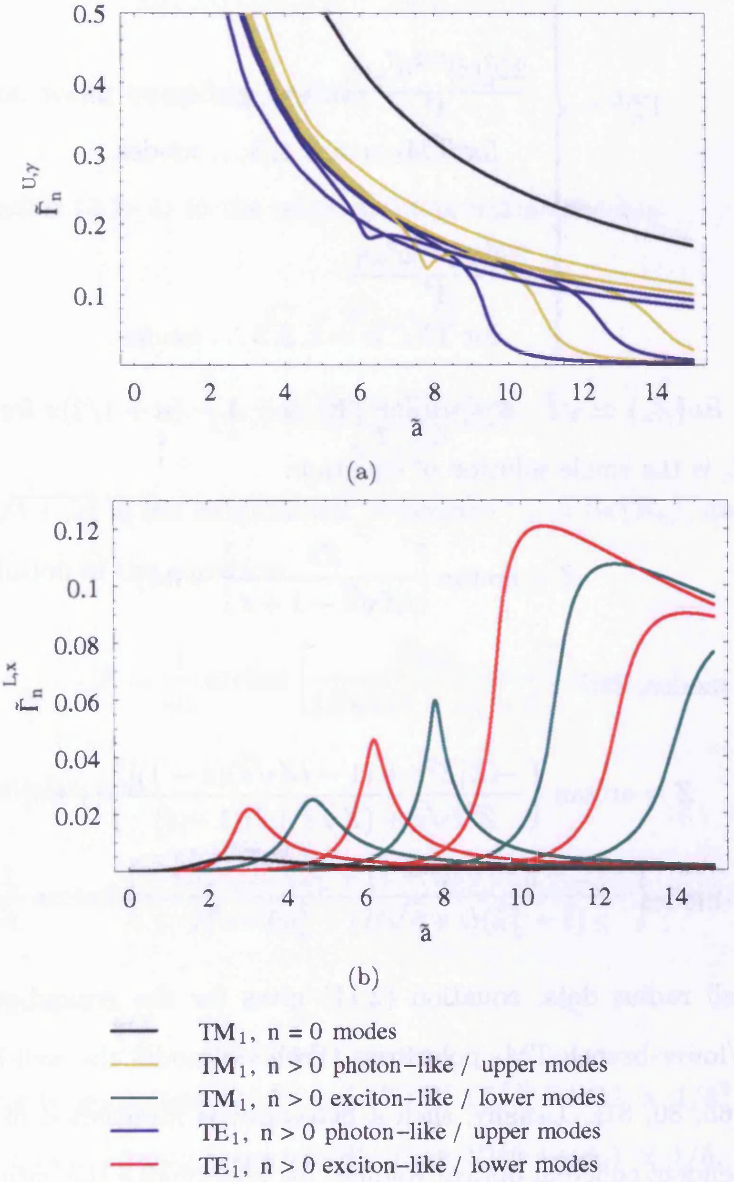

Figure 2.13: The dimensionless polariton radiative widths of (a) upper/photon-like and (b) lower/exciton-like TE and TM modes for $n \leq 4$. The calculation parameters simulate a cyanine-dye J-aggregate sphere surrounded by vacuum; $\tilde{\omega}_\mathrm{p} = 0.09$ and $\tilde{\varepsilon} = 0.385$.

$$\Gamma_n^{x,L} = \begin{cases} \dfrac{2\tilde{\omega}_{\mathrm{p}}^2[(1+2\tilde{\varepsilon})+\tilde{\omega}_{\mathrm{p}}^2]^2(\tilde{\varepsilon})^{5/2}\tilde{a}^3\omega_{\mathrm{T}}}{(1+2\tilde{\varepsilon})^2[(1+2\tilde{\varepsilon})^2+\tilde{\omega}_{\mathrm{p}}^2]} \\ \text{for } \mathrm{TM}_1,\ n=0 \text{ (Fröhlich) mode.} \\ \\ \dfrac{2\tilde{\omega}_{\mathrm{p}}^2(\tilde{\varepsilon})^{5/2}\tilde{a}^7\omega_{\mathrm{T}}}{A^4} \\ \text{for } \mathrm{TM}_1, n=1,2,3\ldots \text{ modes}, \\ \\ \dfrac{2\tilde{\omega}_{\mathrm{p}}^2(\tilde{\varepsilon})^{3/2}\tilde{a}^5\omega_{\mathrm{T}}}{A^4} \\ \text{for } \mathrm{TE}_1,\ n=1,2,3\ldots \text{ modes}. \end{cases} \tag{2.11}$$

where $B_n = \mathrm{Re}\{Z_n\} \simeq \sqrt{\tilde{\varepsilon}}$. $A = n\pi$ for TE_1 and $A = (n+1/2)\pi$ for TM_1 modes. Here $Z = Z_n$ is the single solution of equation:

$$Z = \arctan\left[\frac{Z\tilde{\varepsilon}}{iZ\sqrt{\tilde{\varepsilon}} - 1 + \tilde{\varepsilon}}\right] + n\pi, \tag{2.12}$$

for the TE_1 modes, and

$$Z = \arctan\left\{\frac{-iZ[Z^2\tilde{\varepsilon} + (1 - iZ\sqrt{\tilde{\varepsilon}})(\tilde{\varepsilon}-1)]}{Z^3\tilde{\varepsilon}\sqrt{\tilde{\varepsilon}} + (Z\sqrt{\tilde{\varepsilon}} + i)(1-\tilde{\varepsilon})}\right\} + n\pi, \tag{2.13}$$

for the TM_1 modes.

For small radius dots, equation (2.11) gives for the ground-state ($n = 0$) exciton-like/lower-branch TM_1 polaritons (Fröhlich mode) the well-known result, $\Gamma_{n=0}^{x,L} \propto \tilde{a}^3$ [65, 80, 81]. Usually, such a behaviour is interpreted in terms of the PD-size-dependent coherent optical volume: for very small $\tilde{a}$ the optically coherent area is given by the PD volume, i.e. is $\propto \tilde{a}^3$. With increasing $\tilde{a}$ towards $\tilde{a} \sim 1$, the volume-dependent PD oscillator strength saturates, approaching the strength of exciton-photon interaction in the (PD) bulk material. According to equation (2.11) for $n \geq 1$ one has $\Gamma_n^{x,L}(\tilde{a} \to 0) \propto \tilde{a}^7$ for the TM_1 modes and $\Gamma_n^{x,L}(\tilde{a} \to 0) \propto \tilde{a}^5$ for the TE$_1$ modes. Thus, for a small PD radius, $\Gamma^{x,L}_{n=0} \propto \tilde{a}^3$ absolutely dominates over $\Gamma^{x,L}_n$ associated with the energy modes $n > 0$.

Large radius, weak coupling regime

For a large radius ($\tilde{a} \gg 1$) in the weak coupling regime one has:

$$\Gamma^{\gamma}_n = 2C_n\omega_{\mathrm{T}}/\tilde{a}\,, \tag{2.14}$$

$$\Gamma^{x}_n = \frac{2(A+\pi/2)^2\tilde{\omega}_{\mathrm{p}}^2\omega_{\mathrm{T}}}{\sqrt{\tilde{\varepsilon}}\tilde{\omega}_{\mathrm{L}}^4\tilde{a}^3}\,. \tag{2.15}$$

Here $\tilde{\omega}_{\mathrm{L}} = \sqrt{1+\tilde{\omega}_{\mathrm{p}}^2}$ is the longitudinal frequency, $C_n = \mathrm{Re}\{R_n\}$, and $R = R_n$ is the single solution of the equation:

$$R = \frac{1}{\tilde{\omega}_{\mathrm{L}}}\arctan\left[\frac{R\tilde{\varepsilon}\tilde{\omega}_{\mathrm{L}}}{iR\sqrt{\tilde{\varepsilon}}\tilde{\omega}_{\mathrm{L}}^2 - \tilde{\omega}_{\mathrm{L}}^2 + \tilde{\varepsilon}}\right] + n\pi, \tag{2.16}$$

for the TE$_1$ modes, and

$$R = \frac{1}{\tilde{\omega}_{\mathrm{L}}}\arctan\left\{\frac{-iR\tilde{\omega}_{\mathrm{L}}[R^2\tilde{\varepsilon}\tilde{\omega}_{\mathrm{L}}^2 + (1-iR\sqrt{\tilde{\varepsilon}})(\tilde{\varepsilon}-\tilde{\omega}_{\mathrm{L}}^2)]}{R^3\tilde{\varepsilon}\sqrt{\tilde{\varepsilon}}\tilde{\omega}_{\mathrm{L}}^2 + (R\sqrt{\tilde{\varepsilon}}+i)(\tilde{\omega}_{\mathrm{L}}^2-\tilde{\varepsilon})}\right\} + n\pi, \tag{2.17}$$

for the TM$_1$ modes.

According to equations (2.14) and (2.15), $\Gamma^x_n(\tilde{a} \to \infty) \propto 1/\tilde{a}^3$ decays with increasing dot radius much more rapidly than $\Gamma^{\gamma}_n(\tilde{a} \to \infty) \propto 1/\tilde{a}$, i.e. at large $\tilde{a}$ one has $\Gamma^x_n/\Gamma^{\gamma}_n \ll 1$. The radiative lifetime for the photon-like polaritons at large radius, $\tau^{\gamma}_n = 1/\Gamma^{\gamma}_n = \tilde{a}/2C_n\omega_{\mathrm{T}}$, is $2C_n$ times smaller than the time which is needed for the propagation of the light from the center of the sphere to the surface; $\tau_{ball} = \tilde{a}/\omega_{\mathrm{T}}$. Usually $C_n \sim 1$, so that we interpret $\tau^{\gamma}_n(\tilde{a} \to \infty)$ in terms of the time needed for ballistic escape of photon-like polaritons from the large radius PD sphere. A similar ballistic decay channel is absent for the exciton-like polaritons because in our model the exciton state is assumed to be without translational spatial dispersion, i.e. the excitons are "mechanically" non-propagating modes.

The behaviour of $\Gamma^{\gamma,x}_{n=1}$ in the limits of small and large PD radius is highlighted in figure 2.14 for a cyanine-dye J-aggregate sphere surrounded by vacuum. The agreement between numerical solutions obtained by direct solution of the dispersion equations, and the approximations derived above, for both small and large radii, is shown to be very good.

In the weak coupling limit, according to equations (2.10)-(2.15), the ratio between the radiative lifetimes of photon-like and exciton-like PD polaritons, associated with the energy level $n = 0$ (TM_1 Fröhlich mode), for a small radius is

$$\tau^x_0/\tau^\gamma_0 = \frac{B_0[(1+2\tilde{\varepsilon})^2 + \tilde{\omega}^2_{\mathrm{p}}]}{\tilde{\omega}^2_{\mathrm{p}}\left[1 + \tilde{\omega}^2_{\mathrm{p}}/(1+2\tilde{\varepsilon})\right]^2 \tilde{\varepsilon}^{5/2}\tilde{a}^4}, \tag{2.18}$$

and for a large radius:

$$\tau^x_n/\tau^\gamma_n = \frac{C_n\sqrt{\tilde{\varepsilon}}\tilde{\omega}^4_{\mathrm{L}}\tilde{a}^2}{(A+\pi/2)^2\tilde{\omega}^2_{\mathrm{p}}}, \tag{2.19}$$

for levels with the energy number n. Thus for both limits of the radius, the radiative lifetime of the exciton-like polaritons is greater than that of the photon-like polaritons.

Large radius, strong coupling regime

Numerical evaluation of equations (2.3) and (2.4) shows that, for the weak coupling regime, the real parts of the frequencies of the photon- and exciton-like polariton branches approach asymptotic values, $\tilde{\omega}^\gamma_n \to 0$ and $\tilde{\omega}^x_n \to \tilde{\omega}_{\mathrm{L}}$, as $\tilde{a} \to \infty$. In the strong coupling regime these asymptotic limits are swapped and become $\tilde{\omega}^U_n \to \tilde{\omega}_{\mathrm{L}}$

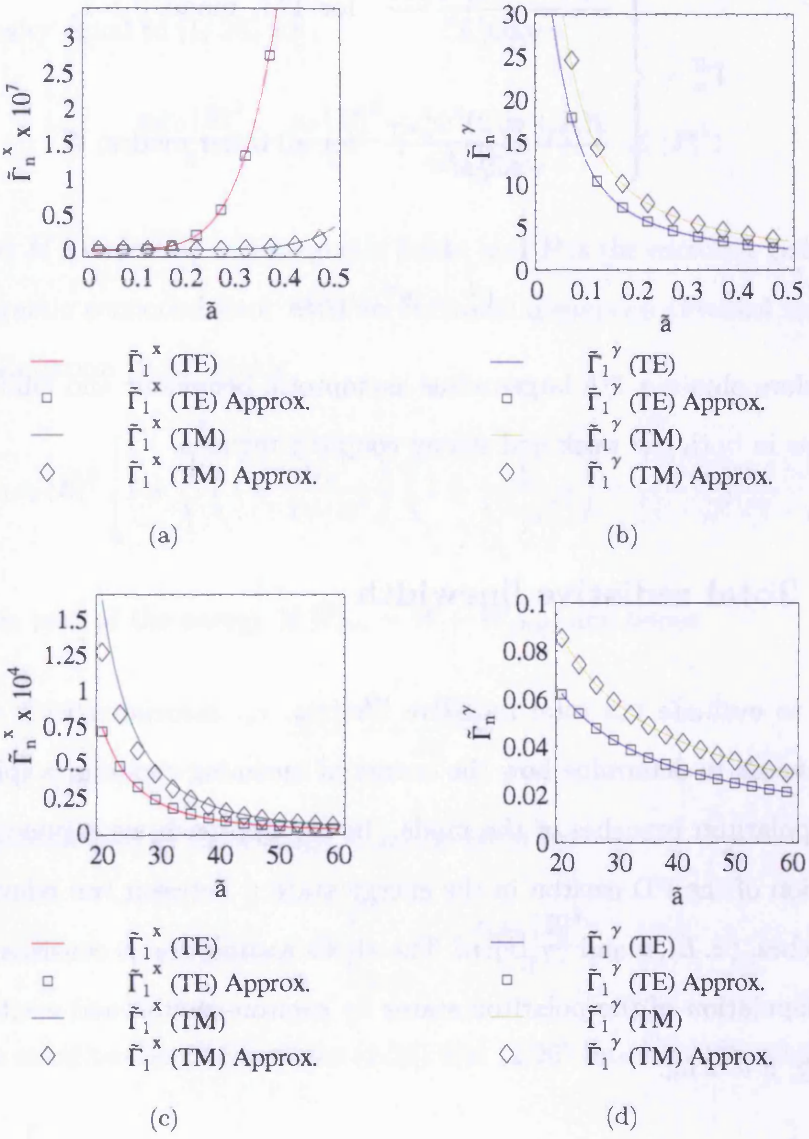

(a) (b)

(c) (d)

Figure 2.14: Plots illustrating the asymptotic behaviour of radiative linewidth, $\tilde{\Gamma}^{x,\gamma}_{n=1}$, at small radii ($\tilde{a} \ll 1$) for the (a) exciton-like and (b) photon-like modes, and at large radii ($\tilde{a} \ll 1$) for the (c) exciton-like and (d) photon-like branches. The solid lines are results from numerical solutions of the dispersion equations. Points depicted by open squares and diamonds are approximations using equations (2.10)-(2.17). Note that the y-axes of (a) and (c) have been rescaled for clarity. The calculation parameters simulate a cyanine-dye J-aggregate sphere surrounded by vacuum; $\tilde{\omega}_\mathrm{p} = 0.09$ and $\tilde{\varepsilon} = 0.385$.

and $\tilde{\omega}_n^L \to 0$, as $\tilde{a} \to \infty$. Thus in the strong coupling regime and for $\tilde{a} \gg 1$ one has

$$\Gamma_n^U = \begin{cases} \dfrac{2(A-\pi/2)^2\tilde{\omega}_p^2\omega_T}{\sqrt{\tilde{\varepsilon}}\tilde{\omega}_L^4\tilde{a}^3} & \text{for TM}_1 \text{ mode, } \tilde{\varepsilon} > 1, \\ \\ \dfrac{2(A+\pi/2)^2\tilde{\omega}_p^2\omega_T}{\sqrt{\tilde{\varepsilon}}\tilde{\omega}_L^4\tilde{a}^3} & \text{for all other modes,} \end{cases} \tag{2.20}$$

$$\Gamma_n^L = 2C_n\omega_T/\tilde{a}\,. \tag{2.21}$$

We therefore obtain a $1/\tilde{a}$ large-radius asymptotic behaviour and ballistic escape of photons in both the weak and strong coupling regimes.

2.4.2 Total radiative linewidth

In order to evaluate the total radiative lifetime, τ_n, associated with a PD exciton, one needs to determine how the energy of incoming excitons is split between the two polariton branches of the mode. In our approach we assume a coherent distribution of the PD exciton in the energy state n between two relevant polariton branches, $(x, L), n$ and $(\gamma, U), n$. The above assumption is consistent with the kinetic population of the polariton states by exciton-exciton and exciton-phonon scattering, if $\tilde{a} \simeq \tilde{a}_n$.

The excitonic and photonic components of each polariton dispersion branch, X_n and Y_n, satisfy the polariton sum rule [3]:

$$\begin{aligned} X_n^{\gamma,U} + X_n^{x,L} = 1, \quad Y_n^{\gamma,U} + Y_n^{x,L} = 1, \\ X_n^{\gamma,U} + Y_n^{\gamma,U} = 1, \quad X_n^{x,L} + Y_n^{x,L} = 1. \end{aligned} \tag{2.22}$$

The excitonic component is given by $X = W_{exc}/W$, where W_{exc} is the energy density associated with the excitonic polarisation, and W is the total electromagnetic energy density equal to [1, 26, 82]

$$W = \frac{\varepsilon_b \varepsilon_0 \left|\boldsymbol{E}\right|^2}{4} + \frac{\mu_0 \left|\boldsymbol{H}\right|^2}{4} + \frac{1}{4\varepsilon_0 \omega_p^2}\left(\left|\omega \boldsymbol{P}\right|^2 + \omega_T^2 \left|\boldsymbol{P}\right|^2\right). \tag{2.23}$$

Here $\boldsymbol{E}$ and $\boldsymbol{H}$ are electric and magnetic fields, and $\boldsymbol{P}$ is the excitonic polarisation. A non-magnetic semiconductor with no excitonic dispersion (Frenkel excitons) is assumed. Equation (2.23) yields

$$W = \frac{1}{4}\varepsilon_{\mathrm{b}}\varepsilon_0 \left|\boldsymbol{E}\right|^2 \left[1 + \sqrt{\left(1 + \frac{\tilde{\omega}_p{}^2}{1 - \tilde{\omega}^2}\right)\left(1 + \frac{\tilde{\omega}_p{}^2}{1 - \tilde{\omega}^{*2}}\right)} + \frac{(\tilde{\omega}\tilde{\omega}^* + 1)\tilde{\omega}_p{}^2}{(1 - \tilde{\omega}^2)(1 - \tilde{\omega}^{*2})}\right]. \tag{2.24}$$

The exciton part of the energy is $W_{exc} = W - W_{phot}$, and hence

$$X = \frac{W - W_{phot}}{W}. \tag{2.25}$$

Here the photon part of the energy, W_{phot}, is given by

$$W_{phot} = W\bigg|_{\tilde{\omega}_p = 0} = 2\,\frac{\varepsilon_0 \varepsilon_{\mathrm{b}} \left|\boldsymbol{E}\right|^2}{4}, \tag{2.26}$$

and simple substitution of equations (2.24) and (2.26) into equation (2.25) gives

$$X = 1 - \left[\frac{2}{1 + \sqrt{\left(1 + \frac{\tilde{\omega}_p{}^2}{1 - \tilde{\omega}^2}\right)\left(1 + \frac{\tilde{\omega}_p{}^2}{1 - \tilde{\omega}^{*2}}\right)} + \frac{(\tilde{\omega}\tilde{\omega}^* + 1)\tilde{\omega}_p{}^2}{(1 - \tilde{\omega}^2)(1 - \tilde{\omega}^{*2})}}\right]. \tag{2.27}$$

Note that equations (2.22)-(2.27) deal with intrinsically complex polariton frequencies $\tilde{\omega} = \tilde{\omega}_n$, due to a finite radiative lifetime of PD polaritons. Nevertheless,

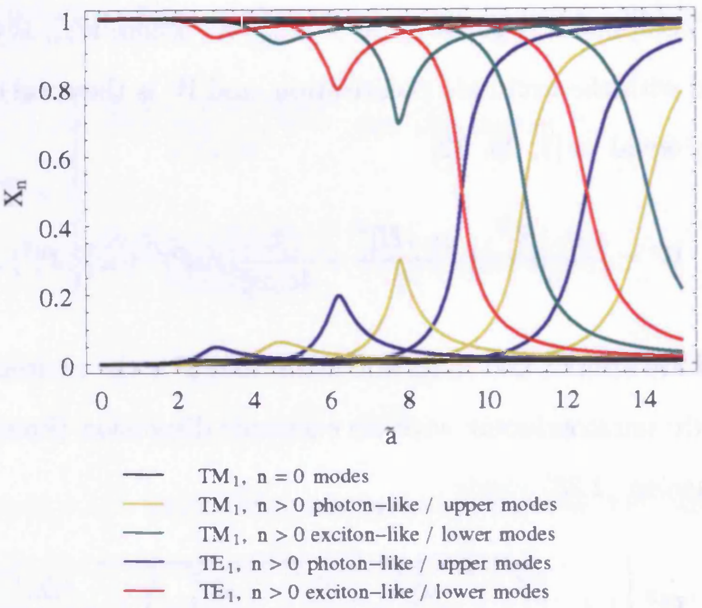

Figure 2.15: Plot $X_n(\tilde{a})$ for the $n \leq 4$ modes of a cyanine dye J-aggregate sphere surrounded by vacuum.

the result of equation (2.27) will always be a real number between 0 and 1 as it is simply a coefficient indicating the relative proportions in which the energy of any given mode, n, is coherently distributed between the two polariton branches. The dispersion of $X_n(\tilde{a})$ is shown in figure 2.15 for the low-order ($n \leq 4$) modes of a cyanine-dye J-aggregate sphere surrounded by vacuum. By definition, the branch with frequency which is closest to the excitonic-resonance line, for any given mode and radius, will have a higher X_n value than the other corresponding branch. Thus the lines in figure 2.15 cross for modes which exhibit anti-crossing in their dispersion curves, and anti-crossing for those that exhibit crossing. Or, in other words, the nature of the lines in figure 2.15 is the same as that of the *imaginary* parts of the dispersion curves. The Fröhlich mode may be difficult to discern in the plot, but its exciton-like mode maintains a value very close to 1 for all radii, and correspondingly its photon-like mode remains close to 0.

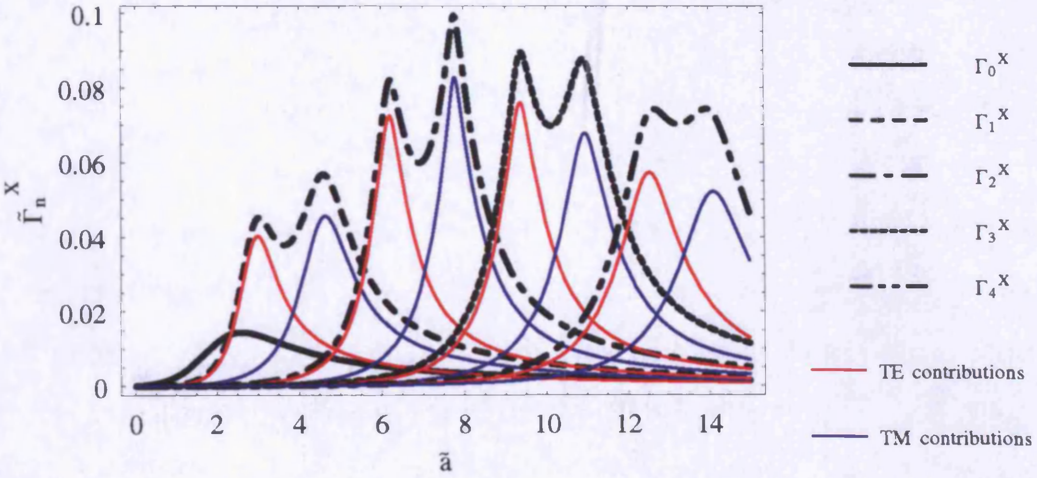

Figure 2.16: The total radiative linewidth, $\tilde{\Gamma}_n^X$, calculated with equation (2.28), for polariton modes with $n \leq 4$. The contributions to the total radiative width from TE and TM contributions are shown, except for $\tilde{\Gamma}_0^X$ which is entirely TM. This simulation models a cyanine dye J-aggregate PD surrounded by vacuum, with $\tilde{\omega}_{\mathrm{p}} = 0.09$ and $\tilde{\varepsilon} = 0.385$.

Within our picture of the coherent distribution of incoming PD excitons among the relevant polariton dispersion branches, the lifetime τ_n^X of level n is $\tau_n^X = 1/\Gamma_n^X$, where Γ_n^X is given by

$$\Gamma_n^X = X_n^{\gamma,U}\Gamma_n^{\gamma,U} + X_n^{x,L}\Gamma_n^{x,L} . \tag{2.28}$$

In figure 2.16 we plot the dependence of $\Gamma_n^X = \Gamma_n^X(\tilde{a})$ for $n = 0$ to 4. The TE and TM components, as well as the sum total, are plotted. The maximum values of Γ_n^X refer to the PD radius $2a \simeq 2a_n \simeq n\lambda/2$, where $\lambda = (2\pi c)/(\omega_{\mathrm{T}}\sqrt{\varepsilon_{\mathrm{b}}})$ is the wavelength of the light field resonant with the exciton state. In this case, the photon spatial quasi-eigen-harmonics $n\lambda/2$, which can be interpreted in terms of constructive interference giving the standing light field pattern inside the spherical photonic dot, resonates with the exciton state. In each double-peak structure, for $\Gamma_{n\neq 0}^X(\tilde{a})$, the first, less-developed maximum is due to the TE$_1$ mode, while the second one, which occurs at larger values of $\tilde{a}$, is attributed to the TM$_1$ mode.

2.4.3 Analytical approximations for small and large radius

Our model is mostly relevant to $\tilde{a} \simeq \tilde{a}_n$. For either very small, $\tilde{a} \ll 1$, or very large, $\tilde{a} \gg 1$, PD radius, the excitonic radiative width Γ_n^X, evaluated by equation (2.28), is dominated by the photon-like polariton branches. In this case, the relevant polariton energies are rather far from the energy $\tilde{\omega}_{\rm T} = 1$ of the optically-undressed excitonic state, and, therefore, the coherent distribution of the incoming excitons among the polariton states is unlikely to occur. Nevertheless, to complete our description of Γ_n^X, below we examine analytic approximations of equation (2.28) for $\tilde{a} \ll 1$ and $\tilde{a} \gg 1$.

For $\tilde{a} \ll 1$, in both weak and strong limits of exciton-photon interaction, we obtain from the equations for the small-radius dependence, (2.10) and (2.11), and from equations (2.25) and (2.28):

$$X_n^{\gamma,U} = \frac{\tilde{\omega}_{\rm p}^2(\tilde{a}^2 + B_n^2)\tilde{a}^2}{[(\tilde{a}^2 + B_n^2) - D_n^2]^2 + 4D_n^2 B_n^2}, \quad X_n^{x,L} = 1 - X_n^{\gamma,U} \simeq 1,$$

$$\Gamma_n^X = X_n^{x,L}\Gamma_n^{x,L} + \frac{2B_n\omega_{\rm T}\tilde{\omega}_p^2(\tilde{a}^2 + B_n^2)\tilde{a}}{[(\tilde{a}^2 + B_n^2) - D_n^2]^2 + 4D_n^2 B_n^2} \simeq \frac{2\omega_{\rm T}\tilde{\omega}_p^2 B_n^3 \tilde{a}}{(B_n^2 + D_n^2)^2}, \tag{2.29}$$

where $D_n = \mathrm{Im}\{Z_n\}$ and Z_n is given by equations (2.12) and (2.13). Equation (2.29) shows that coherent distribution between the polariton branches results in the linear dependence $\Gamma_n^X \propto \tilde{a}$. This is due to the strongly dominant contribution to the optical decay from the photon-like/upper-branch polariton levels, i.e. in equation (2.28) one has $X_n^{\gamma,U}\Gamma_n^{\gamma,U} \gg X_n^{x,L}\Gamma_n^{x,L}$, if $\tilde{a} \ll 1$.

For $\tilde{a} \gg 1$ in the weak coupling regime, equations (2.14), (2.15), (2.25) and

(2.28) yield

$$X_n^{\gamma} = \frac{\tilde{\omega}_p^2}{(1+\tilde{\omega}_{\mathrm{p}}^2)}, \qquad X_n^{x} = 1 - X_n^{\gamma} = \frac{1}{(1+\tilde{\omega}_{\mathrm{p}}^2)},$$

$$\Gamma_n^X = \frac{2C_n\omega_{\mathrm{T}}\tilde{\omega}_{\mathrm{p}}^2}{(1+\tilde{\omega}_{\mathrm{p}}^2)\tilde{a}} + \frac{2(A+\pi/2)^2\tilde{\omega}_{\mathrm{p}}^2\omega_{\mathrm{T}}}{\sqrt{\tilde{\varepsilon}}\tilde{\omega}_{\mathrm{L}}^4(1+\tilde{\omega}_{\mathrm{p}}^2)\tilde{a}^3}. \tag{2.30}$$

In a similar way, for $\tilde{a} \gg 1$ and the strong coupling regime, one derives from equations (2.20), (2.21), (2.25) and (2.28):

$$X_n^{U} = \frac{1}{(1+\tilde{\omega}_{\mathrm{p}}^2)}, \qquad X_n^{L} = 1 - X_n^{U} = \frac{\tilde{\omega}_p^2}{(1+\tilde{\omega}_{\mathrm{p}}^2)},$$

$$\Gamma_n^X = \frac{2C_n\omega_{\mathrm{T}}\tilde{\omega}_{\mathrm{p}}^2}{(1+\tilde{\omega}_{\mathrm{p}}^2)\tilde{a}} + \frac{2\tilde{\omega}_{\mathrm{p}}^2\omega_{\mathrm{T}}}{\sqrt{\tilde{\varepsilon}}\tilde{\omega}_{\mathrm{L}}^4(1+\tilde{\omega}_{\mathrm{p}}^2)\tilde{a}^3}\begin{cases} (A-\pi/2)^2 & \text{for TM}_1\text{ mode, } \tilde{\varepsilon} > 1, \\ (A+\pi/2)^2 & \text{for all other modes.} \end{cases} \tag{2.31}$$

Thus for $\tilde{a} \to \infty$ equations (2.30) and (2.31) are approximated by the same formula:

$$\Gamma_n^X \simeq \frac{2C_n\omega_{\mathrm{T}}\tilde{\omega}_{\mathrm{p}}^2}{(1+\tilde{\omega}_{\mathrm{p}}^2)\tilde{a}}. \tag{2.32}$$

Equation (2.32) yields $\tau_n^X \propto \tilde{a}$, which can be interpreted in terms of the ballistic escape ("optical evaporation") of optically-dressed excitons from large-size spherical photonic dots. The ratio between radiative time $\tau_n^X = 1/\Gamma_n^X$ and the time for the propagation of the light from the center of the sphere to the surface, τ_{ball}, is given by:

$$\frac{\tau_n^X}{\tau_{ball}} = \frac{1}{\Gamma_n^X\tau_{ball}} = \frac{(1+\tilde{\omega}_{\mathrm{p}}^2)\tilde{a}\,\omega_{\mathrm{T}}}{2C_n\omega_{\mathrm{T}}\tilde{\omega}_{\mathrm{p}}^2\,\tilde{a}} = \frac{1+\tilde{\omega}_{\mathrm{p}}^2}{2C_n\tilde{\omega}_{\mathrm{p}}^2}. \tag{2.33}$$

In this expression the term $\tilde{\omega}_{\mathrm{p}}^2/(1+\tilde{\omega}_{\mathrm{p}}^2)$ takes into account the excitonic component of the polariton branch with zero asymptotic frequency as $\tilde{a} \to \infty$ (photon-like branch for the weak interaction regime, lower-branch for the strong). Hence, for the weak coupling regime the exciton part is very small and $\tau_n^X/\tau_{ball} \gg 1$. For the strong coupling regime, when $\tilde{\omega}_{\mathrm{p}} \simeq 1$, the excitonic component is of the order of unity so that $\tau_n^X/\tau_{ball} \simeq 1/2C_n \sim 1$.

2.5 Summary

The aim of this chapter has been to examine the polariton optics of a spherical nanostructure without considering the effects of the spatial dispersion of excitons. By also neglecting incoherent scattering the model is somewhat simplistic but produces a picture of the completely coherent polariton optics of the system. The relative simplicity of the model allows for a clear and precise understanding of the underlying physics to be obtained.

The assumptions used in the derivation of this model limits its applicability. The requirement that the PD and surrounding material be optically isotropic, homogeneous, non-magnetic materials does limit the scope of the model's applicability. However, a great many semiconductors – both organic and inorganic – still satisfy these conditions, including very popular materials such as gallium arsenide and copper chloride. The use of the weak-confinement regime to model the excitons as point particles, discarding the need to consider the relative electron-hole motion, sets a lower limit on the size of the PD that can be truly simulated by this model. Although this may make the model unsuitable for small quantum dots, the most interesting aspects of polariton optics occur at larger radii, where the excitonic and photonic frequencies converge. The greatest limitation of the model arises from our exclusion of spatial dispersion. Only excitons with very high effective translational mass, $M_{\mathrm{x}} \rightarrow \infty$, or truly dispersionless matter excitations such as TO-phonons, can be considered, though this restriction can be relaxed for radii large enough that the effects of spatial dispersion become negligible.

Our model produces the frequencies of the polariton branches as a function of radius; $\tilde{\omega}(\tilde{a})$, for any given set of simulation parameters. With suitable selection of the Rabi frequency, $\tilde{\omega}_{\mathrm{p}}$ and the ratio of dielectric permittivities, $\tilde{\varepsilon}$, we can model any materials that fall within the models limits for both the PD and the surrounding medium. Of course, any radius range is possible, also within the limits of applicability outlined above.

By analysing the topology of the dispersion curves produced for different values of the material parameters we have defined the weak and strong polariton coupling regimes, in direct analogy with the bulk material case, and illustrated how modes can hence be easily be identified and classified accordingly. As a direct consequence of this classification, the terminology used to identify a mode is thus strictly defined and we have stressed the use of *exciton-like* and *photon-like* modes to refer to modes in the weak coupling regime, and *upper* and *lower* modes for use in the strong coupling regime. This removes any ambiguity that would be caused by using *upper* and *lower* when discussing weak-coupled modes, which exhibit crossing in their dispersion curves and hence could be thought of either *upper* or *lower* depending on the radius in question. Our terminology is also very succinct, as it conveys both the mode's regime and branch-type in a single word.

For determining the radiative lifetime of the modes we have maintained a paradigm of completely coherent polariton optics by coherently distributing the energy of each mode between the corresponding two polariton branches. This is in contrast to an incoherent distribution as would result, for example, from direct optical pumping near the exciton resonance. We have shown that the radial dependence of the inverse radiative lifetime, Γ_n^X, at small radius is dominated by the cubic dependence, $\tilde{a}^3$, of the Fröhlich mode, whilst higher order modes exhibit high-order behaviour of $\tilde{a}^5$ and $\tilde{a}^7$. Γ_n^X thus increases to a maximum point at $2a = 2a_n \sim n\lambda/2$, and decays $\propto 1/a$ as the radius is further increased. We have thus reproduced the well-known conclusions that the behaviour at low radius can be attributed to the volume-dependent increase of the oscillator strength, whilst the large radius behaviour results from the ballistic escape of optically-dressed excitons from the PD.

Chapter 3

Polariton optics of spherical nanostructures including spatial dispersion

In this chapter we extend our treatment of the polariton optics of a spherical PD to include the effects of the spatial dispersion of excitons. The confinement of the exciton wavefunction within the PD causes the allowed energy levels of the exciton to rise. If the radius of the PD is reduced towards zero, the exciton energy levels rise rapidly towards infinity.

The following section will introduce the dispersion equations for polaritons including spatial dispersion. These will be used to plot the dispersion curves for a CuCl PD surrounded by vacuum, and the data compared to results published in the literature. Section 3.3 derives equations for the dispersion of excitons in the absence of any photon field, which are then used to form analytical expression for the polariton frequencies. These are used in Section 3.5 to calculate the radiative lifetime of the polariton modes. During this latter section we will investigate the radial dependence of the modes, in a similar manner to Section 2.4.1, using three different approaches: analytical, semi-analytical and purely numerical. From this we will conclude that, as $a \rightarrow 0$, the a^3 dependence does not apply in the presence of spatial dispersion due to the rise of the excitonic frequencies towards infinity, and the subsequent breach of the Long-Wavelength Approximation (LWA).

3.1 Polariton dispersion equations

In Chapter 2 we neglected the effect of spatial dispersion by removing the M_{x} from the macroscopic polariton equations, (2.1). Reintroducing this term we can identify three types of waves: two are transverse with propagation constants k_1 and k_2 given by solutions to:

$$\begin{aligned} \frac{k^2c^2}{\omega^2} &= \varepsilon(\omega, k) \\ &= \varepsilon_{\mathrm{b}}\left[1 + \frac{\omega_{\mathrm{p}}^2}{\omega_{\mathrm{T}}^2 + (\hbar\omega_{\mathrm{T}}/M_{\mathrm{x}})k^2 - i\omega\gamma_{\mathrm{x}} - \omega^2}\right], \end{aligned} \tag{3.1}$$

and the third is longitudinal with propagation constant k_3 defined by the root of the equation:

$$\varepsilon(\omega, k) = 0. \tag{3.2}$$

We will continue to neglect incoherent scattering, $\gamma_{\mathrm{x}} = 0$, removing this term from equation (3.1) and maintaining our picture of the completely coherent polariton optics.

In order to solve the macroscopic polariton equations within spherical coordinates we must apply the boundary conditions used in Chapter 2 (continuous behaviour of the tangential components of the electric and magnetic fields at the surface of the sphere, and the light field at $r \to \infty$ has an outgoing part only) plus an additional boundary condition (ABC) [52]. We use Pekar's boundary condition according to which the excitonic polarisation becomes zero at the surface of the sphere; $\mathbf{P}_{\mathrm{r=a}} = 0$ [83]. This is most applicable when the size of the PD is large compared to the Bohr radius of the exciton, and the potential difference at the surface of the PD is large, such that the exciton wavefunction is strongly confined within the PD.

The polariton eigenfrequencies in the presence of spatial dispersion can be classified as TM and TE modes [52, 55, 72]. The TM modes have mixed character (they are neither pure transverse, nor pure longitudinal). The dispersion equation is:

$$\begin{vmatrix} [k_0 a h_l(k_0 a)]' & [k_1 a j_l(k_1 a)]' & [k_2 a j_l(k_2 a)]' & -j_l(k_3 a) \\ (k_0 a)^2 h_l(k_0 a) & (k_1 a)^2 j_l(k_1 a) & (k_2 a)^2 j_l(k_2 a) & 0 \\ 0 & (\varepsilon_1 - \varepsilon_{\mathrm{b}})[k_1 a j_l(k_1 a)]' & (\varepsilon_2 - \varepsilon_{\mathrm{b}})[k_2 a j_l(k_2 a)]' & \varepsilon_{\mathrm{b}} j_l(k_3 a) \\ 0 & (\varepsilon_1 - \varepsilon_{\mathrm{b}}) l(l+1) j_l(k_1 a) & (\varepsilon_2 - \varepsilon_{\mathrm{b}}) l(l+1) j_l(k_2 a) & \varepsilon_{\mathrm{b}} k_3 a [j_l(k_3 a)]' \end{vmatrix} = 0, \tag{3.3}$$

where k_1, k_2 and k_3 are the propagation constants given above, $\varepsilon_1 = k_1^2 c^2/\omega^2$, $\varepsilon_2 = k_2^2 c^2/\omega^2$, a is the radius of the sphere, $k_0 = \omega\sqrt{\varepsilon_{\mathrm{d}}}/c$, ε_{d} is the dielectric permittivity of the medium surrounding the sphere, and $j_l(k_i a)$ and $h_l(k_i a)$ are spherical Bessel and Hankel functions of the first kind, as described in the previous chapter. In solving these dispersion equations we will again restrict ourselves to the case of lowest angular momentum, $l = 1$, in order to minimise the energy of the polariton modes.

Equation (3.3) was derived by Ruppin when he was investigating the frequency of the TM $l = 1$ surface mode [72, equation (97)]. In his earlier work he found the light scattering coefficients from a sphere including and excluding spatial dispersion ([52] and [72] respectively). We believe that the dispersion equation (3.3) should be identical to the denominator of the scattering coefficient, Q [see 52, equation (24)] despite Ruppin's omission of a prime to indicate a derivative in the last term of the determinant.

TE modes have transverse character (divE $= 0$), and are described by the dispersion equation:

$$\begin{vmatrix} h_l(k_0a) & j_l(k_1a) & j_l(k_2a) \\ [k_0ah_l(k_0a)]' & [k_1aj_l(k_1a)]' & [k_2aj_l(k_2a)]' \\ 0 & (\varepsilon_1 - \varepsilon_b)j_l(k_1a) & (\varepsilon_2 - \varepsilon_b)j_l(k_2a) \end{vmatrix} = 0. \tag{3.4}$$

It can be derived by taking equations (92) and (93) in [72], relevant to TM case, and exchanging the positions of $\mathbf{N}_{lm}$ and $\mathbf{M}_{lm}$, and either by equating the coefficients C^i_{lm} to zero, or by equating the denominator S to zero [see 52, equation (23)]. Dispersion equations can also be obtained using spherical vector harmonics $\mathbf{Y}_{JLM}$ instead of vectors $\mathbf{N}_{lm}$ and $\mathbf{M}_{lm}$ [84], however the dispersion equations obtained there are not the same as Eqs. (3.3) and (3.4) due to the approximations used.

3.1.1 Dimensionless parameters

The results shown in this chapter will be recognisable and comparable to those shown in Chapter 2, and we therefore will not rely on dimensionless parameters in order to understand the physical processes underlying the numerical results. Where possible we will plot the resulting polariton frequencies in dimensional parameters in order to give a clearer indication of the actual values of the parameters concerned, in particular the radius of the PD and the polariton frequencies.

However the same dimensionless parameters as used in the previous chapter will be used once again, particularly in the analytical solutions for the radiative linewidth (Section 3.5). They are repeated here for clarity: frequency $\tilde{\omega} = \omega/\omega_{\mathrm{T}}$, Rabi frequency $\tilde{\omega_{\mathrm{p}}} = \omega_{\mathrm{p}}/\omega_{\mathrm{T}}$, PD radius $\tilde{a} = \sqrt{\varepsilon_{\mathrm{b}}}\omega_{\mathrm{T}}a/c$, and ratio of dielectric permittivities $\tilde{\varepsilon} = \varepsilon_{\mathrm{d}}/\varepsilon_{\mathrm{b}}$. We also introduce a dimensionless parameter which measures the degree of spatial dispersion; $\tilde{D} = (\hbar\omega_{\mathrm{T}}\varepsilon_{\mathrm{b}})/(M_{\mathrm{x}}c^2)$.

3.2 Example material system: Copper Chloride (CuCl)

Since we are no longer constrained to modelling dispersionless excitons there is a much wider range of materials that can be considered, however the material must still be homogenous and optically isotropic. CuCl is a natural choice as an example material system because it is one of the most thoroughly investigated materials for the physics of excitons. The parameters for modelling a CuCl PD surrounded by vacuum are: $\omega_{\mathrm{T}} = 3.203\,\mathrm{eV}$, $\omega_{\mathrm{p}} = 0.191\,\mathrm{eV}$ and $\varepsilon_{\mathrm{b}} = 5.6$ [54, 85]. We use $M_{\mathrm{x}} = 2.3\ m_e$ [54] to obtain $\tilde{D} = 1.35 \times 10^{-5}$.

Plots of the TE modes of a CuCl PD, for $n = 1$ to 4, are shown in figure 3.1. Modes including spatial dispersion, calculated with equations (3.3) and (3.4), are plotted as dashed coloured lines over the same modes without spatial dispersion (solid black lines). Figures 3.1(a) and 3.1(b) show that the real and imaginary parts of the dispersion curves of modes calculated with spatial dispersion agree with those calculated without, with the exception of the close vicinity of $a \rightarrow 0$.

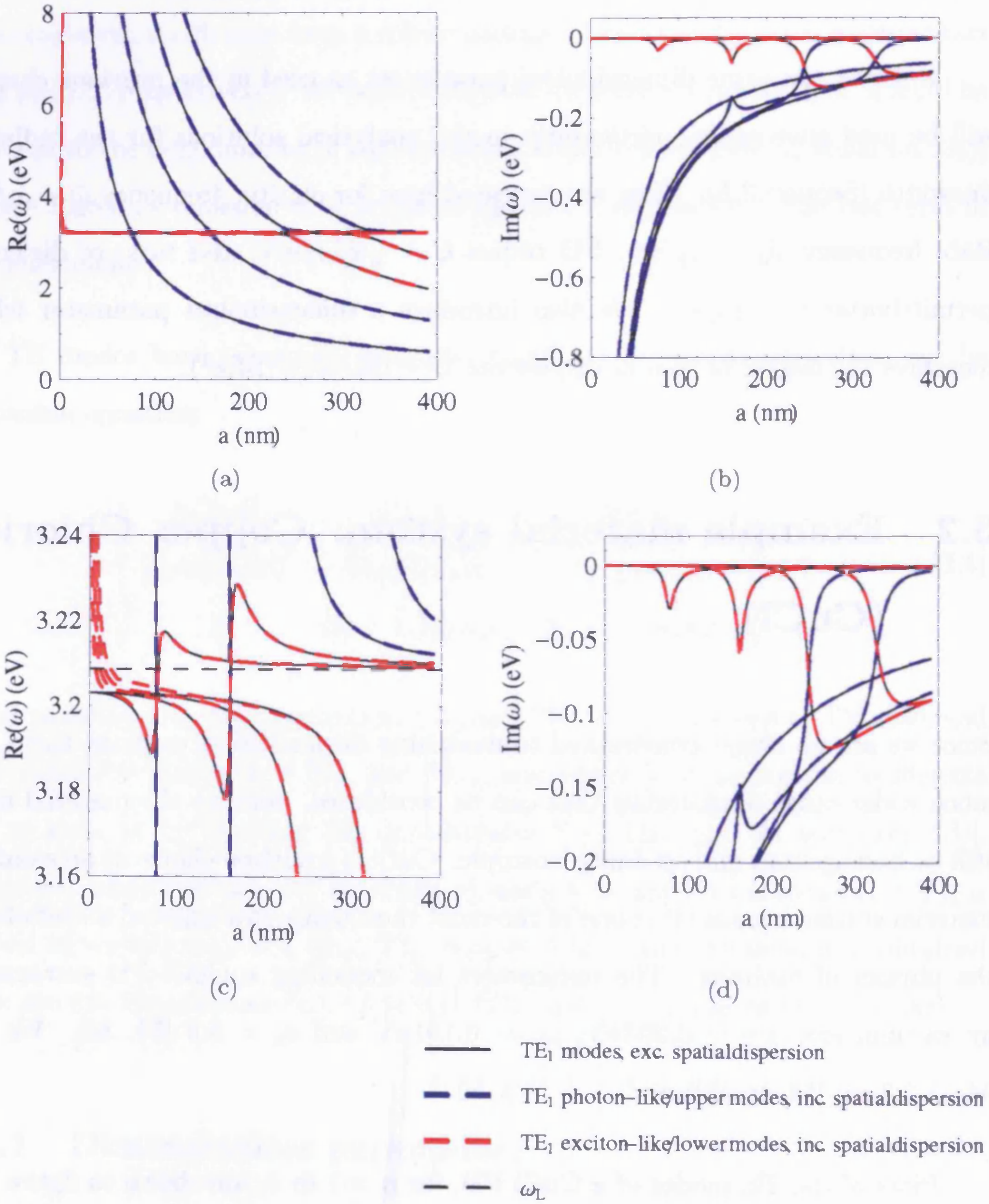

Figure 3.1: Plots of the TE$_1$, $n = 1, 2, 3, 4$ polariton dispersion curves for a CuCl PD surrounded by vacuum excluding (black solid lines) and including (dashed red and blue lines) spatial dispersion. The position of the longitudinal frequency, ω_L is indicated by a horizontal dotted line. (a) and (b) show the real and imaginary parts of the polariton frequencies over a wide radius range, making the effect of spatial dispersion almost impossible to see. The frequency axis is rescaled in (c) and (d) in order to show the states around the exciton line and illustrate the effect of spatial dispersion.

Figure 3.1(c) shows the effect of spatial dispersion more clearly. For small radius the real parts of the exciton-like/lower branches rapidly rise towards infinity, whilst the imaginary parts are left almost unchanged.

Figures 3.1(c) and 3.1(d) show that the $n = 1$ and 2 modes exhibit crossing and are in the weak coupling regime, whilst $n = 3$ and 4 anti-cross and are in the strong coupling regime. This is in direct contradiction to CuCl dispersion curves plotted by Ajiki *et al.* which are purely in the weak coupling regime [55]. This discrepancy is due to the ω dependence of coefficient $\tilde{A}_{\xi\xi'}(\omega)$ being neglected in equation (62) of that reference. The coefficient $\tilde{A}_{\xi\xi'}(\omega)$ is the interaction energy between the exciton and photon field and the removal of the omega-dependence introduces the assumption that this interaction is constant, directly leading to all modes being found in the same coupling regime. If the omega-dependence is included in the method described by Ajiki *et al.*, the more detailed behaviour shown by our results is revealed.

3.3 Spatial dispersion of excitons

Equations (3.3) and (3.4) can be solved numerically to give the frequencies of polariton modes including spatial dispersion. However for analytical purposes and the determination of the total radiative lifetime (Section 3.5) we derive expressions for the frequencies of exciton modes in the absence of any transverse light field.

We solve the Hopfield equation for the polarisation (2.1) with the Pekar boundary condition and obtain two types of solution. The first is purely transverse, div**P** = 0, and corresponds to TE polaritons:

$$j_l(k'a) = 0, \tag{3.5}$$

where $(k')^2 = (\omega^2 - \omega_{\mathrm{T}}^2)/(\hbar\omega_{\mathrm{T}}/M_{\mathrm{x}})$. It immediately follows that

$$\omega_{nl}^2 = \omega_{\mathrm{T}}^2 + \frac{\hbar\omega_{\mathrm{T}} X_{nl}^2}{M_{\mathrm{x}} a^2}, \tag{3.6}$$

where X_{nl} is the n^{th} root of the function j_l, i.e., $j_l(X_{nl}) = 0$.

If we consider these levels coupled with TE photon modes to form TE polaritons, using the approximation $\omega_{\mathrm{T}} \gg \hbar X_{nl}^2/M_{\mathrm{x}} a^2$ we reproduce the result:

$$\omega_{nl} = \omega_{\mathrm{T}} + \hbar X_{nl}^2 / 2M_{\mathrm{x}} a^2 \tag{3.7}$$

obtained in [54]. It is clear that at large radius the frequency of the exciton levels tend to the frequency of dispersionless excitons, i.e., $\omega_{nl} \to \omega_{\mathrm{T}}$ when $a \to \infty$.

The second solution has mixed character (div**P** $\neq 0$ and curl**P** $\neq 0$, applicable to TM polaritons) with dispersion equation

$$l(l+1) j_l(k'a) j_l(k''a) - k''a \frac{d[k'a j_l(k'a)]}{d(k'a)} \frac{d[j_l(k''a)]}{d(k''a)} = 0, \tag{3.8}$$

where $(k')^2 = (\omega^2 - \omega_{\mathrm{T}}^2)/(\hbar\omega_{\mathrm{T}}/M_{\mathrm{x}})$ and $(k'')^2 = (\omega^2 - \omega_{\mathrm{p}}^2 - \omega_{\mathrm{T}}^2)/(\hbar\omega_{\mathrm{T}}/M_{\mathrm{x}})$. Solutions of Eq. (3.8) can only be obtained numerically, but the asymptotic values of these solutions coincide with results obtained in previous works: for small radius and frequencies higher than ω_{L}, with

$$\omega_{nl} = \omega_{\mathrm{T}} + \frac{\hbar \pi^2 n^2}{2M_{\mathrm{x}} a^2}, \tag{3.9}$$

derived in [84]. For large radii, solutions of equation (3.8) asymptotically coincide with frequencies:

$$\omega_{nl} = \omega_{\mathrm{T}} + \frac{\hbar(n\pi)^2}{2M_{\mathrm{x}}a^2}, \tag{3.10}$$

and

$$\omega_{nl} = \omega_{\mathrm{T}} + \Delta_{\mathrm{LT}} + \frac{\hbar(n\pi)^2}{2M_{\mathrm{x}}a^2}, \tag{3.11}$$

obtained in [54, see figure 4], where longitudinal splitting is $\Delta_{\mathrm{LT}} = \omega_{\mathrm{p}}^2/(2\omega_{\mathrm{T}})$. It can be seen that at large radius there are two asymptotic frequencies; $\omega_{nl} \to \omega_{\mathrm{T}}$ and $\omega_{nl} \to \omega_{\mathrm{L}}$ as $a \to \infty$.

3.4 Total radiative linewidth

We can now determine the total polariton radiative linewidth in a similar manner to that presented in Section 2.4.2. The excitonic component of the polariton energy is described by the Hopfield transformation coefficients [3, 74] modified for complex frequency:

$$X = \frac{\omega_{\mathrm{p}}^2\omega_{\mathrm{ex}}^2}{\omega_{\mathrm{p}}^2\omega_{\mathrm{ex}}^2 + (\omega_{\mathrm{ex}}^2 - \omega^2)(\omega_{\mathrm{ex}}^2 - \omega^{*2})}, \tag{3.12}$$

$$Y = 1 - X,$$

where ω_{ex} is equal to ω_{nl} from one of equations (3.6),(3.9),(3.10) or (3.11). The radiative lifetime of level n is then $\tau_n^{\mathrm{X}} = 1/\Gamma_n^{\mathrm{X}}$ given by

$$\Gamma_n^{\mathrm{X}} = X_n^{\gamma,\mathrm{U}}\Gamma_n^{\gamma,\mathrm{U}} + X_n^{\mathrm{x,L}}\Gamma_n^{\mathrm{x,L}}. \tag{3.13}$$

Equation (3.13) assumes that the energy is distributed between one photonic branch and one excitonic branch, which entirely describes the TE case. However,

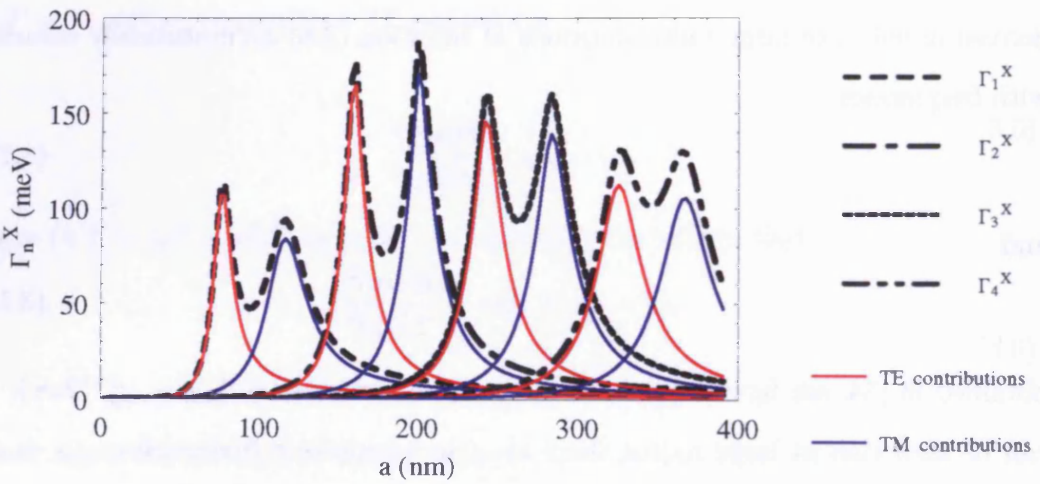

Figure 3.2: The total radiative linewidth, $\tilde{\Gamma}_n^X$, calculated with equation (3.13), for polariton modes with $n \leq 4$, with the TE and TM contributions. This simulation models a CuCl PD surrounded by vacuum.

for TM modes there are two excitonic branches; one that asymptotically approaches ω_T, and one which approaches ω_L. However, the excitonic mode near the longitudinal frequency have radiative lifetimes two or three times larger than the radiative lifetimes of the branch close to ω_T; their contribution to Γ_n^X is negligibly small. The resulting radiative linewidths are plotted in figure 3.2.

3.5 Asymptotic radial dependence of the radiative linewidth

The effect of spatial dispersion has been shown to be limited to small radii. As the radius is increased the polariton frequencies rapidly approach those calculated without spatial dispersion, and hence the radial dependence at large radius is the same as described in Section 2.4.1. Spatial dispersion also has no effect on the photon branches, so we must now consider only the effect of spatial dispersion on the excitonic branch at small radius. In the following sections we will undertake three different approaches: the first approach is a purely analytical expansion of the dispersion equations in a similar manner to that used in Section 2.4.1, the second approach is a semi-analytical analysis of the dispersion equations to identify negligible terms, and the last approach is a purely numerical analysis of the polariton frequencies.

3.5.1 Analytical expansion

If we expand the dispersion equation in terms of the complex frequency, as outlined in Section 2.4.1, we can isolate the imaginary parts of the dispersion equations to derive equations for Γ_n at small radius. Though we take radius a to be small it is possible to identify two possible approximations; $\tilde{a}^2 < X_{nl}^2\tilde{D}$ and $\tilde{a}^2 > X_{nl}^2\tilde{D}$. The resulting equations for the radiative linewidth are:

$$\Gamma_n^{x,L} \cong C_n \begin{cases} \dfrac{2X_{nl}^2\tilde{D}^2\tilde{\omega}_{\mathrm{p}}^2(\tilde{\varepsilon})^{3/2}\tilde{a}}{9} & (\mathrm{TE}_1 \text{ modes}, \tilde{a}^2 < X_{nl}^2\tilde{D}), \\[2ex] \dfrac{2(n\pi)^2\tilde{D}^2\tilde{\omega}_{\mathrm{p}}^2(\tilde{\varepsilon})^{5/2}\tilde{a}^3}{9} & (\mathrm{TM}_1 \text{ modes}, \tilde{a}^2 < X_{nl}^2\tilde{D}), \end{cases} \tag{3.14}$$

and

$$\Gamma_n^{x,L} \cong C_n \begin{cases} \dfrac{2\tilde{\omega}_{\mathrm{p}}^2(\tilde{\varepsilon})^{3/2}\tilde{a}^5}{9X_{nl}^2} & (\mathrm{TE}_1 \text{ modes}, \tilde{a}^2 > X_{nl}^2\tilde{D}), \\[2ex] \dfrac{2\tilde{\omega}_{\mathrm{p}}^2(\tilde{\varepsilon})^{5/2}\tilde{a}^7}{9(n\pi)^2} & (\mathrm{TM}_1 \text{ modes}, \tilde{a}^2 > X_{nl}^2\tilde{D}). \end{cases} \tag{3.15}$$

The proportionality coefficient $C_n \approx 1$ is a complicated function of n and $\tilde{\varepsilon}$, and for certain parameters it can have a large deviation from unity. However, most importantly it is not a factor of radius.

Although our desire to find a small radius dependence suggests that $\tilde{a}^2 < X_{nl}^2\tilde{D}$ would be an appropriate condition, $\tilde{D}$ takes very small values (1.53×10^{-5} for CuCl) such that these equations can, at best, only be considered applicable exceptionally close to $a \rightarrow 0$. The condition $\tilde{a}^2 > X_{nl}^2\tilde{D}$ produces equations with a^5 and a^7 in agreement with similar equations excluding spatial dispersion.

3.5.2 Semi-analytical expansion

Dr. Nikolaev (Cardiff University) has performed a semi-analytical approach to finding the small-radius dependence. By expanding the dispersion equations and examining the magnitude of each term for different radii, small-magnitude terms were identified and removed, whilst plots of the resulting dispersion curves were made to ensure that accuracy was not lost. The resulting dispersion equations were considerably reduced and yielded:

$$\Gamma_n^{\mathrm{x,L}} \cong \begin{cases} \dfrac{12\tilde{\omega}_{\mathrm{p}}^2(\tilde{\varepsilon})^{5/2}\omega_{\mathrm{T}}\tilde{a}^3}{(n\pi)^2(2\tilde{\varepsilon}+1)^2} & (\mathrm{TM}_1 \text{ modes}), \\[2ex] \dfrac{2}{9}\dfrac{\tilde{\omega}_{\mathrm{p}}^2(\tilde{\varepsilon})^{3/2}\omega_{\mathrm{T}}\tilde{a}^5}{[(n+0.5)\pi]^2} & (\mathrm{TE}_1 \text{ modes}). \end{cases} \tag{3.16}$$

This reproduces the a^5 dependence for TE$_1$ modes produced by the analytical method. An a^3 dependence is produced for TM$_1$ modes, similar to the Fröhlich mode in the absence of spatial dispersion. However, the Fröhlich mode does not exist in the presence of spatial dispersion, and instead appears as an anti-crossing interaction in the other TM modes ($n > 0$) at frequencies corresponding to the dispersionless Fröhlich mode [54]. The Fröhlich mode can be described as being "distributed" across the other modes. If we sum up all the TM$_1$ modes, ie. sum over all n in equation (3.16), we get:

$$\sum_{n=1}^{\infty} \Gamma_n^{\mathrm{x,L}} \cong \sum_{n=1}^{\infty} (n^2\pi^2) \times \frac{12\tilde{\omega}_{\mathrm{p}}^2(\tilde{\varepsilon})^{5/2}\omega_{\mathrm{T}}\tilde{a}^3}{(2\tilde{\varepsilon}+1)^2} = \frac{2\tilde{\omega}_{\mathrm{p}}^2(\tilde{\varepsilon})^{5/2}\omega_{\mathrm{T}}\tilde{a}^3}{(2\tilde{\varepsilon}+1)^2}. \tag{3.17}$$

This numerical agreement is reinforced by the fact that this summation agrees analytically with our expression for the dispersionless Fröhlich mode in equation (2.11) if $\tilde{\omega}_{\mathrm{p}}^2$ is taken to be small in comparison to $(1 + 2\tilde{\varepsilon})$. Our radiative linewidth summed from the TM_1 modes:

$$\frac{1}{\tau_r} = \sum_{n=1} \Gamma_n^{\mathrm{x,L}} \simeq 32\pi^3 \frac{\tilde{\varepsilon}\omega_{\mathrm{T}}^2}{(2\tilde{\varepsilon}+1)^2} \left(\frac{a}{\lambda}\right)^3 \frac{\Delta \mathrm{E}_{\mathrm{LT}}}{\hbar}, \tag{3.18}$$

recovers the well-known result of Hanamura [65, 81], where λ is the wavelength of the excitonic resonance and $\Delta\mathrm{E}_{\mathrm{LT}}$ is the longitudinal-transverse splitting energy. Note, however, that we use the true radius of the PD, a, rather than the effective radius, a^*.

3.5.3 Numerical analysis

We will now analyse the behaviour of Γ_{x} directly from the numerical results calculated from the dispersion equations. If we consider the radiative linewidth to be proportional to the radius to some unknown degree, x:

$$\Gamma_n^{\mathrm{X}} = Ka^x, \tag{3.19}$$

where K is an unknown constant. We take the natural logarithm of both sides:

$$\ln(\Gamma_n^{\mathrm{X}}) = \ln(K\tilde{a}^x) = \ln(K) + x\ln(\tilde{a}), \tag{3.20}$$

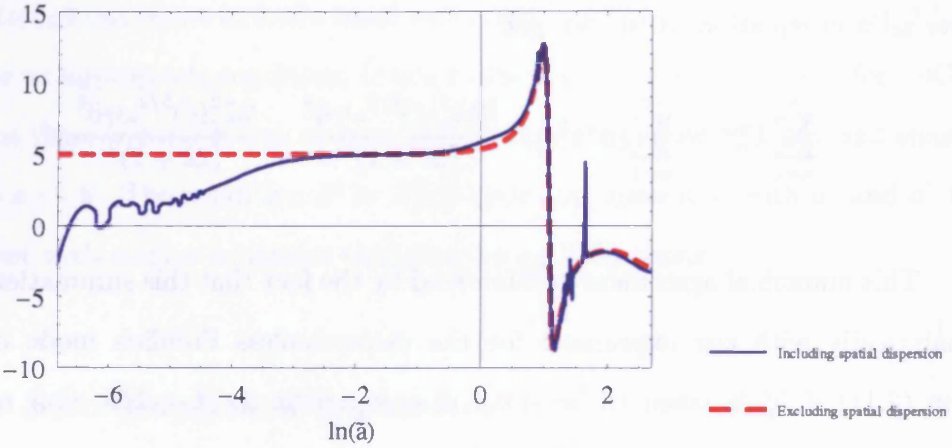

Figure 3.3: Plots of $x = \frac{d}{d[\ln(a)]}\ln(\Gamma_n^{\mathrm{X}})$ against $\ln(a)$ including (solid-blue line) and excluding (dashed-red line) spatial dispersion for the TE_1, $n = 1$ exciton-like/lower mode of a CuCl PD surrounded by vacuum.

which has the form of a straight line. In order to find x we take the derivative:

$$\frac{d}{d[\ln(\tilde{a})]}\ln(\Gamma_n^{\mathrm{X}}) = x. \tag{3.21}$$

Not only is this analysis elegantly straightforward, but plotting x against $\ln(\tilde{a})$ serves to highlight the low-radius section of the dispersion. We choose to use the dimensionless radius rather than its dimensional form to make it easier to identify sections of the curve.

Figure 3.3 plots x against $\ln(a)$ for the TE_1, $n = 1$ exciton-like mode, including and excluding spatial dispersion (solid-blue and dashed-red lines respectively). The jagged fluctuations in the curve including spatial dispersion are the result of numerical inaccuracies. General features of both curves are a peak in x at a radius corresponding to the resonant cross-over, which then immediately inverts and remains negative at high radius. Excluding spatial dispersion we see a constant value of $x = 5$ at low radius, confirming the a^5 dependence given by equation (2.11). When spatial dispersion is included the a^5 dependence tapers down to about a^1

(averaging out the numerical fluctuations) as $a \to 0$. This corroborates *both* equations (3.14) and (3.15) given by our analytical expansion.

Figure 3.4 plots similar curves for the $n = 2, 3$ and 4 modes. These graphs show clearly that at high radius the modes all approach value of $x = -1$, confirming the $1/a$ dependence derived in Section 2.4.1. They also show decreases in x around $\ln(\tilde{a}) = 1$. This is far enough away from $a = 0$ that this region should not be considered to be at "small radius" and hence there is no conflict with the equations derived either by our analytical or semi-analytical approach. It serves, however, to illustrate that the behaviour of the radiative linewidth is not as simple as the low-radius dependencies alone.

3.6 Summary

The purpose of this chapter has been to expand on the analysis done in Chapter 2 to include the effects of spatial dispersion of excitons. We have used the dispersion equations derived by Ruppin to plot the dispersion curves for a CuCl PD surrounded by vacuum. In doing so we have shown that the weak and strong coupling regimes apply just as discussed in the previous chapter. We show that the $n = 1, 2$ modes are in the weak regime, whilst $n = 3, 4$ are in the strong regime, in contrast with the work of Ajiki *et al.* where all modes are in the weak regime due to the approximations used [55].

We have shown that the dispersion of non-interacting excitons agree with the results of Ajiki *et al.*, and used these equations to plot the radiative linewidth using the coherent distribution of energy between the polariton modes.

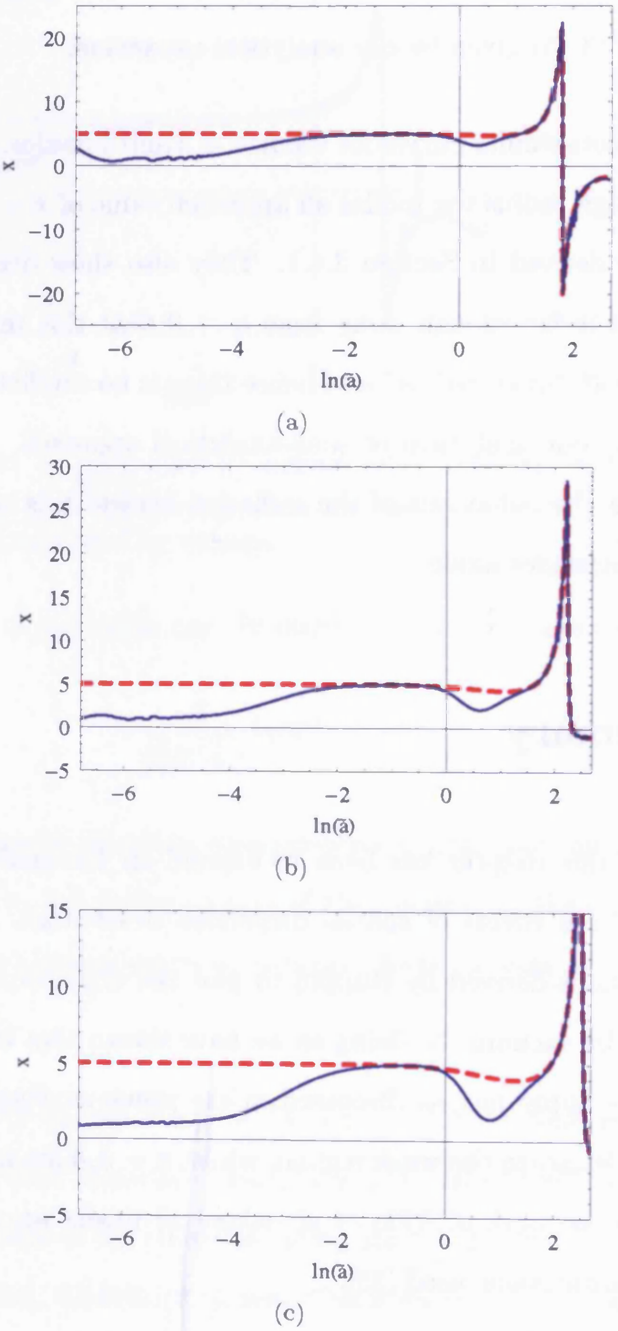

Figure 3.4: Plots of $x = \frac{d}{d[\ln(a)]}\ln(\Gamma_n^X)$ against $\ln(a)$ including (solid-blue line) and excluding (dashed-red line) spatial dispersion for the TE$_1$, (a) $n = 2$, (b) $n = 3$ and (a) $n = 4$ exciton-like/lower mode of a CuCl PD surrounded by vacuum.

Since spatial dispersion of excitons only affects the excitonic polariton branch, and only at low radius, the asymptotic behaviour of the radiative linewidth of the photonic branch (and the excitonic branch at high radius) is the same as the dispersionless case. We have analysed the asymptotic behaviour of the radiative linewidth of the excitonic branch at low radius using a purely analytical, semi-analytical and purely numerical approach. We obtain an a^3 dependence for TM_1 modes, which can be attributed to the interaction of the TM_1 modes with the Fröhlich surface mode in the infinite-mass, dispersionless case.

Numerical results support the result of the analytical approach that the behaviour of the TE_1 modes drops towards an a^1 dependence as $a \to 0$. This dependence would dominate even the a^3 dependence, and appears to contradict observed data [65]. However, Hanamura's a^3 dependence is only valid in the Long-Wavelength Approximation, $a_\mathrm{B} \ll a \leq \lambda$. In the presence of spatial dispersion the real frequencies of the excitonic polariton branches rapidly rise towards infinity, $\mathrm{Re}(\omega) \to \infty$ as $a \to 0$, quickly becoming comparable to the frequency of the photonic branches; $\mathrm{Re}(\omega_n^{x,L}) \sim \mathrm{Re}(\omega_n^{\gamma,U})$, and the LWA is no longer valid. Our a^1 dependence is just an interesting artifact of our continuous model because the radii over which it applies are smaller than the size of real quantum dots. In the extreme limit, as $a \to 0$, the radius becomes smaller than the lattice constant of the crystal, and the existence of excitons this small – let alone a nanostructure to confine them – is impossible.

In the next chapter we will investigate the conditions that determine whether any given mode is in the weak or strong regime, and the transition between these regimes. From our results in this chapter it will be useful to note that the effect of spatial dispersion is restricted to very small values of radius. Whilst the radius at which spatial dispersion becomes truly negligible will vary depending on the simulation parameters, i.e. the materials be modelled, we can note that for CuCl spatial dispersion becomes negligible long before a given mode reaches its resonant cross-over point.

Chapter 4

Transition between the polariton coupling regimes

In Chapter 2 we classified polaritons into the weak and strong coupling regimes, depending on the topology of their dispersion curves within a three-dimensional space; Re(ω), Im(ω) and a. This classification is equally applicable to the modes including spatial dispersion shown in Chapter 3. In the weak coupling regime the real parts of the dispersion curves cross whilst the imaginary parts anti-cross, but in the strong coupling regime this is reversed. These different dispersion curves all result from the same dispersion equations, and it is possible to move smoothly from one regime to another simply by changing the simulation parameters. Therefore a transition must occur between the two regimes, and the purpose of this chapter is to define this transition and the conditions at which it occurs.

In either the weak or strong regime, the two polariton branches of any given mode never have the same complex frequency. Whilst the real parts of the polariton frequencies cross in the weak regime, the imaginary parts do not and the branches never meet. The reverse behaviour in the strong coupling regime has the same effect. However, as the transition between regimes occurs the different topologies must swap over. It is therefore very natural to define the transition between the two regimes as the point at which the two polariton branches of a given mode have the same frequency:

$$\tilde{\omega}_n^{\gamma,\mathrm{U}} = \tilde{\omega}_n^{\mathrm{x},\mathrm{L}}. \tag{4.1}$$

Our simulations in previous chapters have shown that the regime in which a mode resides is determined by the parameters of the simulation; simply compare figures 2.4 and 2.6. Within a completely coherent picture, one can easily move between the coupling regimes simply by changing ω_p, i.e. the oscillator strength of exciton-photon interaction, and keeping all other parameters unchanged. The topology of the polariton dispersion curves changes at $\omega_\mathrm{p} = \omega_\mathrm{p}^\mathrm{cr}$, so that for $\omega_\mathrm{p} \leq \omega_\mathrm{p}^\mathrm{cr}$ ($\omega_\mathrm{p} \geq \omega_\mathrm{p}^\mathrm{cr}$) one has the "crossing" ("anti-crossing") behaviour of the real parts of the polariton frequencies, i.e. the weak (strong) coupling regime. The transition is illustrated in figure 4.1. This transition is simple to comprehend, since an increasing oscillator strength will result in greater exciton-photon interaction. Since $\omega_\mathrm{p} = 0$ must give purely photonic modes, and a high ω_p must give strongly interacting polaritons, the transition due to ω_p is clearly logical.

The dispersion curves in in figure 4.1(b) are, strictly speaking, plotted *near* the transition, as it is numerically impossible to plot the curves exactly at the transition point. A close inspection of the real parts of the dispersion curves reveals a small gap between the lines, indicating that the mode is just inside the strong coupling regime, and the lines on the graph are coloured accordingly. Nevertheless, the 3D plot of the dispersion curves illustrates the two modes intersecting at the transition point, whilst a clear gap remains in both figure 4.1(b) and (c).

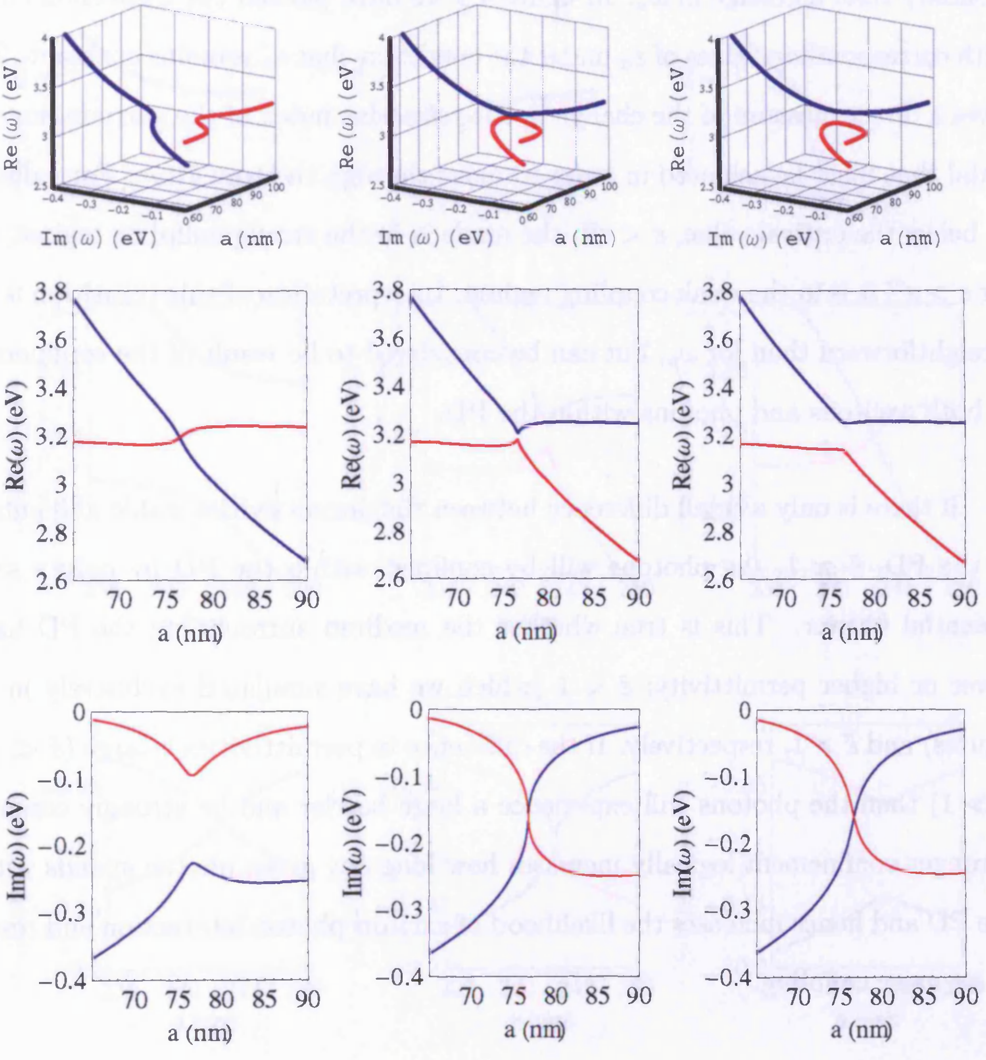

(a) $\omega_{\mathrm{p}} = 0.3$ (b) $\omega_{\mathrm{p}} = \omega_{p}^{\mathrm{cr}} = 0.323$ (c) $\omega_{\mathrm{p}} = 0.35$

Figure 4.1: Transition between the weak and strong coupling limits for the TE$_1$, $n = 1$ mode and $\tilde{\varepsilon} = 0.178$, corresponding to a CuCl sphere surrounded by vacuum. The mode is seen to be (a) in the weak coupling regime, $\tilde{\omega}_{\mathrm{p}} < \tilde{\omega}_{\mathrm{p}}^{\mathrm{cr}}$, (b) very near the transition point, $\tilde{\omega}_{\mathrm{p}} = \tilde{\omega}_{\mathrm{p}}^{\mathrm{cr}}$ and (c) in the strong coupling regime, $\tilde{\omega}_{\mathrm{p}} > \tilde{\omega}_{\mathrm{p}}^{\mathrm{cr}}$. The photon-like / upper branches are shown in blue, whilst the exciton-like / lower branches are shown in red.

A similar transition can be achieved by changing the ratio of the background dielectric permittivities, $\tilde{\varepsilon} = \varepsilon_{\mathrm{d}}/\varepsilon_{\mathrm{b}}$, which is considerably easier to achieve experimentally than a change in ω_{p}. In figure 4.2 we have plotted the dispersion curves with corresponding values of ε_{d} under the condition that ε_{b} remains constant. This gives a direct measure of the change in the refractive index of the surrounding material that must be achieved in order to move through the transition. For values of ε_{d} below the critical value, $\varepsilon < \varepsilon^{\mathrm{cr}}$, the mode is in the strong coupling regime, and for $\varepsilon > \varepsilon^{\mathrm{cr}}$ it is in the weak coupling regime. Interpretation of this transition is less straightforward than for ω_{p}, but can be considered to be result of the confinement of both excitons and photons within the PD.

If there is only a small difference between the permittivities inside and outside of the PD, $\tilde{\varepsilon} \simeq 1$, the photons will be confined within the PD by only a small potential barrier. This is true whether the medium surrounding the PD has a lower or higher permittivity; $\tilde{\varepsilon} < 1$ (which we have simulated exclusively in our figures) and $\tilde{\varepsilon} > 1$, respectively. If the difference in permittivities is large ($\tilde{\varepsilon} \ll 1$ or $\tilde{\varepsilon} \gg 1$) then the photons will experience a large barrier and be strongly confined. Stronger confinement logically increases how long any given photon spends within the PD and hence increases the likelihood of exciton-photon interaction and results in stronger coupling.

The transition point for a given mode occurs at $\tilde{a} = \tilde{a}_n^{\mathrm{cr}} \simeq \tilde{a}_n$, where crossing of the polariton frequencies takes place, whether it is crossing of the real parts of the dispersion curves in the weak regime or imaginary parts in the strong regime. We can therefore attribute the transition to a discrete point at which the simulation parameters have these specific, *critical* values; $\tilde{\omega}_{\mathrm{p}}^{\mathrm{cr}}, \tilde{\varepsilon}^{\mathrm{cr}}$ and $\tilde{a}^{\mathrm{cr}}$.

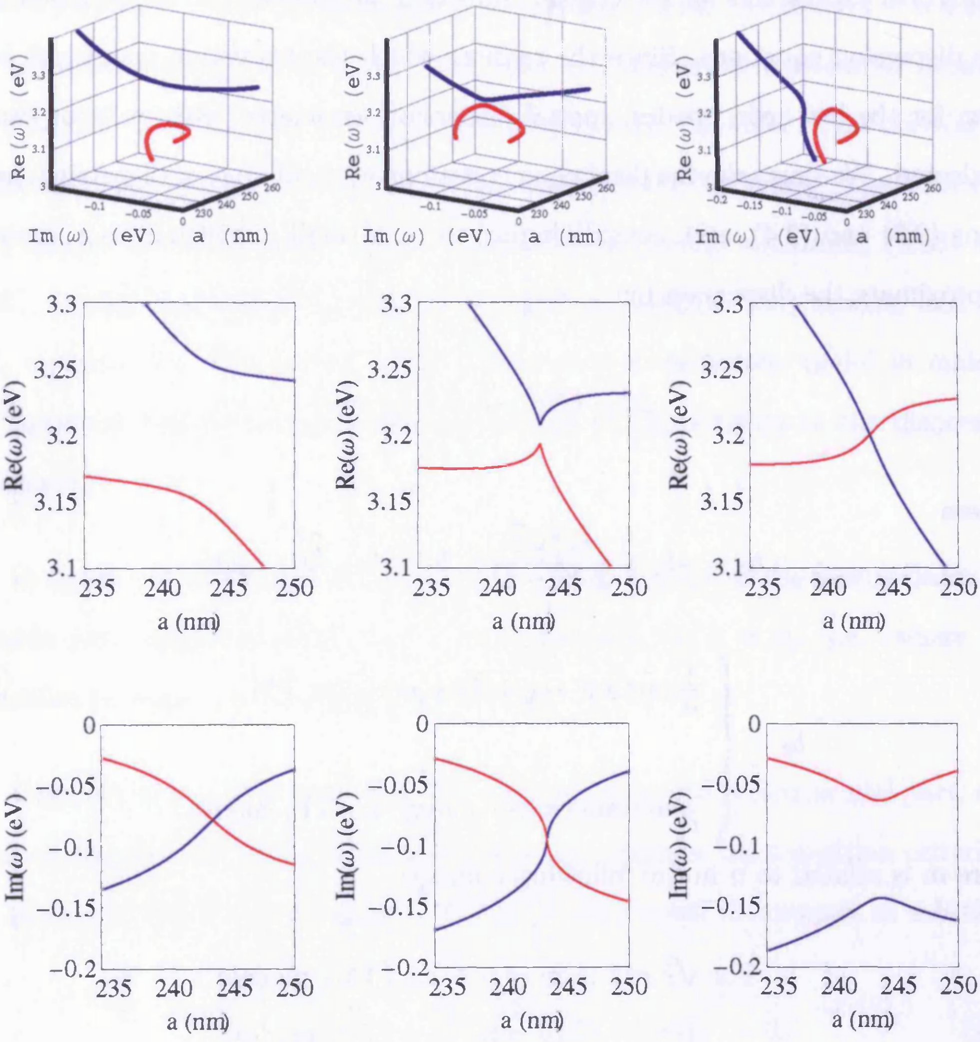

(a) $\varepsilon_{\mathrm{d}} = 1.1$ (b) $\varepsilon_{\mathrm{d}} = \varepsilon_{\mathrm{d}}^{\mathrm{cr}} = 1.495$ (c) $\tilde{\varepsilon} = 1.7$

Figure 4.2: Transition between the weak and strong coupling regimes, induced by changing ε_{d}, and hence $\tilde{\varepsilon}$, for the TE$_1$ mode, $n = 3$ and $\tilde{\omega}_{\mathrm{p}} = 0.0596$, corresponding to a CuCl sphere. The critical value of the relative dielectric constant, $\tilde{\varepsilon}^{\mathrm{cr}} = \varepsilon_{\mathrm{d}}^{\mathrm{cr}}/\varepsilon_{\mathrm{b}} = 1.495/5.6 = 0.267$. (a) strong coupling regime, $\varepsilon_{\mathrm{d}} < \varepsilon_{\mathrm{d}}^{\mathrm{cr}}$, (b) $\varepsilon_{\mathrm{d}} = \varepsilon_{\mathrm{d}}^{\mathrm{cr}}$ and (c) weak coupling regime, $\varepsilon_{\mathrm{d}} > \varepsilon_{\mathrm{d}}^{\mathrm{cr}}$. The photon-like / upper branches are shown in blue, whilst the exciton-like / lower branches are shown in red.

4.1 Critical parameters of the transition point

Analytical expressions for the critical transition parameters can be obtained from the dispersion equations. Since the radii at which the transition occurs are large even for the low order modes, spatial dispersion associated with excitons can be neglected. We thus take the dispersion equations without spatial dispersion, equations (2.3) and (2.4), and, considering $\tilde{\omega}_{\mathrm{p}}^2$ to be a small dimensionless parameter, approximate the dispersion by:

$$\tilde{\omega}^3 - b_2\tilde{\omega}^2 - b_1\tilde{\omega} - b_0 = 0, \tag{4.2}$$

where

$$b_0 = -b_2 + \frac{i\tilde{\omega}_{\mathrm{p}}^2\sqrt{\tilde{\varepsilon}}}{2\tilde{a}(\tilde{\varepsilon}-1)}, \quad b_1 = 1 + \frac{\tilde{\omega}_{\mathrm{p}}^2}{2}, \quad \text{and}$$

$$b_2 = \begin{cases} \frac{1}{\tilde{a}}[\arctan(-i\sqrt{1/\tilde{\varepsilon}}) + m\pi] & \text{for TM}_1, \\ \\ \frac{1}{\tilde{a}}[\arctan(-i\sqrt{\tilde{\varepsilon}}) + m\pi] & \text{for TE}_1 \text{ modes.} \end{cases} \tag{4.3}$$

Here m is related to n in the following manner:

$$\begin{array}{lll} \text{For } \sqrt{\tilde{\varepsilon}} < 1: & m = n+1, & (\text{TM}_1 \text{ modes}) \\ & m = n, & (\text{TE}_1 \text{ modes}) \\ \\ \text{For } \sqrt{\tilde{\varepsilon}} > 1: & m = n, & (\text{TM}_1 \text{ modes}) \\ & m = n+1. & (\text{TE}_1 \text{ modes}) \end{array} \tag{4.4}$$

This inelegant correspondence between m and the radial quantum number arises because the definition of b_2 is rooted in the dispersion equations for $l = 0$

photon modes. During the derivation of the above approximation we take the Rabi frequency to be small, and take this to the limit of $\omega_{\rm p} = 0$ to substitute in a photon frequency term, ω_n^0, for a polariton frequency term. Although $l = 0$ modes are unphysical within a spherical PD, there is a numerical correlation between $l = 0$ and $l = 1$ modes which allows us to swap one for the other. This correlation is discussed and proved numerically in Section 6.2 in the Appendix. The definition of b_2 should be compared to the $l = 0$ photon dispersion equations, (6.56) and (6.57), noting that the TE_0 equation is used to describe TM_1 modes, and the TM_0 equation for TE_1 modes. This substitution is extremely useful in making the equations tractable because of the absence of any k-terms in the dispersion equations.

In figure 4.3 we show that, although it loses accuracy as the radius decreases towards zero, approximation (4.2) is very accurate for $\tilde{a} \simeq \tilde{a}_n$, i.e. where the transition between two coupling limits occurs.

One root of Eq. (4.2) yields a polariton frequency with negative real part, and is hence unphysical. The remaining double root satisfies the transition criterion, Eq. (4.1), and hence we can obtain the transition critical parameters as solutions to:

$$\left(\frac{1}{3}b_1 + \frac{1}{9}b_2^2\right)^3 - \left[\frac{1}{6}(b_1 b_2 + 3b_0) + \frac{1}{27}b_2^3\right]^2 = 0\,. \tag{4.5}$$

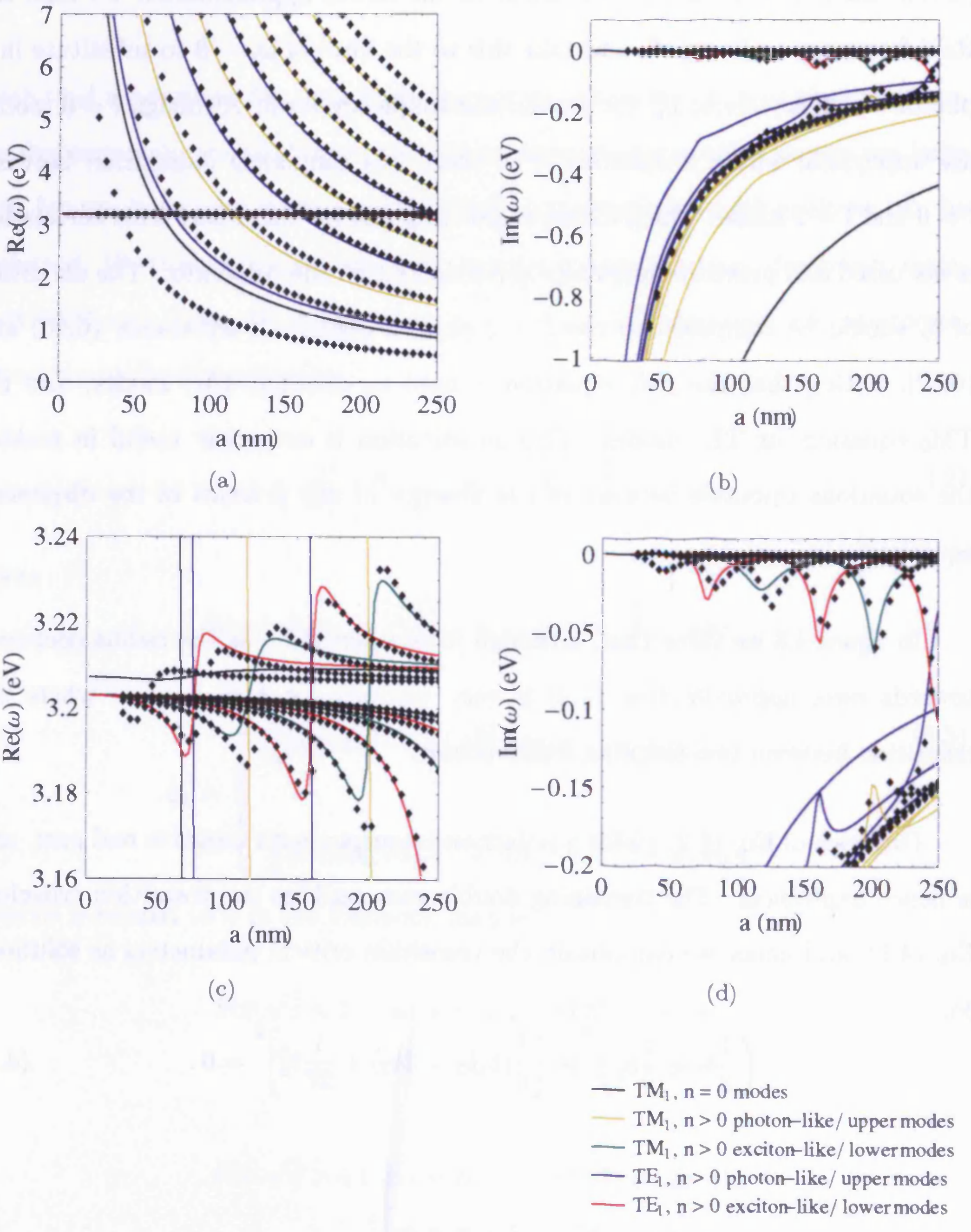

(a) (b)

(c) (d)

Figure 4.3: Comparison between numerical solutions of the dispersion equations (solid lines) and the third-order approximation, equation (4.2) (diamond points). (c) and (d) illustrate the good agreement for radii around the transition point, $a \simeq a_n$. The simulation is for the lower-order modes, $n \leq 4$, of a CuCl PD surrounded by vacuum; $\tilde{\varepsilon} = 0.179$ and $\tilde{\omega}_\mathrm{p} = 0.0596$.

This can be further approximated to:

For $\sqrt{\tilde{\varepsilon}} < 1$:

$$\tilde{a}_n^{\mathrm{cr}} = n\pi \text{ (TE}_1\text{ modes)} \tag{4.6a}$$

$$\tilde{a}_n^{\mathrm{cr}} = (n+0.5)\pi \text{ (TM}_1\text{ modes)} \tag{4.6b}$$

$$\tilde{\omega}_{\mathrm{p}}^{\mathrm{cr}} = \frac{1}{2\tilde{a}_n^{\mathrm{cr}}} \ln \frac{1+\sqrt{\tilde{\varepsilon}}}{1-\sqrt{\tilde{\varepsilon}}}, \tag{4.6c}$$

$$\tilde{\varepsilon}^{\mathrm{cr}} = \frac{[1-\exp(2\tilde{\omega}_{\mathrm{p}}\tilde{a}_n^{\mathrm{cr}})]^2}{[1+\exp(2\tilde{\omega}_{\mathrm{p}}\tilde{a}_n^{\mathrm{cr}})]^2}. \tag{4.6d}$$

For $\sqrt{\tilde{\varepsilon}} > 1$:

$$\tilde{a}_n^{\mathrm{cr}} = (n+0.5)\pi \text{ (TE}_1\text{ modes)} \tag{4.7a}$$

$$\tilde{a}_n^{\mathrm{cr}} = n\pi \text{ (TM}_1\text{ modes)} \tag{4.7b}$$

$$\tilde{\omega}_{\mathrm{p}}^{\mathrm{cr}} = \frac{1}{2\tilde{a}_n^{\mathrm{cr}}} \ln \frac{1+\sqrt{\tilde{\varepsilon}}}{\sqrt{\tilde{\varepsilon}}-1} \tag{4.7c}$$

$$\tilde{\varepsilon}^{\mathrm{cr}} = \frac{[1+\exp(2\tilde{\omega}_{\mathrm{p}}\tilde{a}_n^{\mathrm{cr}})]^2}{[1-\exp(2\tilde{\omega}_{\mathrm{p}}\tilde{a}_n^{\mathrm{cr}})]^2}. \tag{4.7d}$$

The approximate equations (4.6a) and (4.7a) are plotted alongside direct numerical solutions of (4.1) in figure 4.4. It shows that the approximations remain accurate for small values of ω_{p}, but become progressively less accurate as ω_{p} increases, or as ε_{d} approaches $\varepsilon_{\mathrm{b}} = 5.6$ ($\tilde{\varepsilon} = 1$).

Figures 4.4(c) and 4.4(d) can be used to determine which modes will be in which regime. Find the point on either graph corresponding to any given values of ω_{p} and ε_{d}, and note where the transition lines for different modes lie relative to that point. In figure 4.4(c) modes lying above the point will be in the weak coupling regime, whilst those below will be in the strong regime. Similarly with figure 4.4(d) modes to the left of the point will be strong, and those to the right

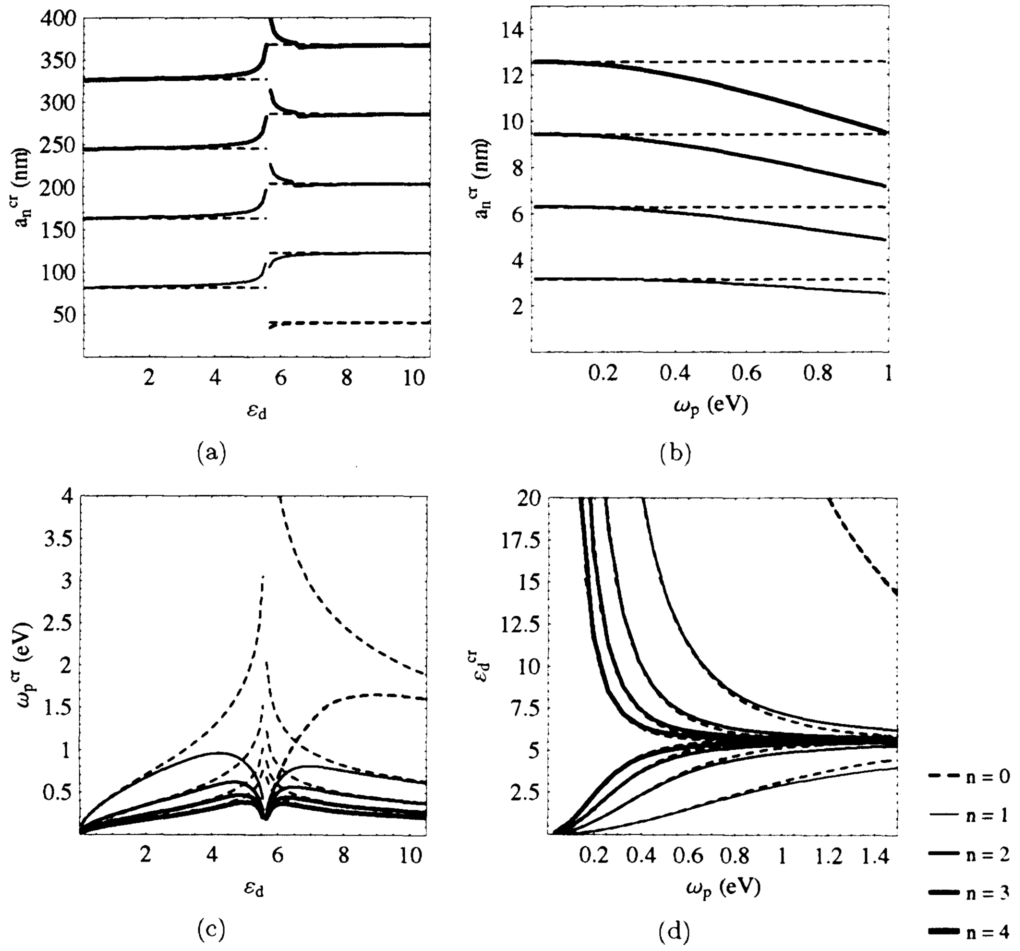

(a) (b)

(c) (d)

Figure 4.4: Graphs of the transition critical parameters calculated using equation (4.5) (blue lines, see legend) and approximations (4.6a) and (4.7a) (black dashed lines); (a) $a_n^{\rm cr} = a_n^{\rm cr}(\varepsilon_{\rm d})$, (b) $a_n^{\rm cr} = a_n^{\rm cr}(\omega_{\rm p})$, (c) $\omega_{\rm p}^{\rm cr} = \omega_{\rm p}^{\rm cr}(\varepsilon_{\rm d})$, and (d) $\varepsilon_{\rm d}^{\rm cr} = \varepsilon_{\rm d}^{\rm cr}(\omega_{\rm p})$. Parameters kept constant in each graph are set at values corresponding to a CuCl PD surround by vacuum; (a) $\omega_{\rm p} = 0.191\,{\rm eV}$, (b) $\varepsilon_{\rm d} = 1$, and for (c) and (d) the radius took the appropriate values given by equations (4.6a) and (4.7a).

will be weak.

4.2 Possible experimental observation of the transition point

Any theoretical model of the transition point will remain strictly that – a *theory* – until such time as experimental evidence that supports it can be obtained. Unfortunately, our description of the transition point using dispersion curves does not lend itself to experimental verification, since dispersion curves are notoriously difficult to map experimentally. To solve this problem we have identified the transition point within a quantity that is more easily observed: the total radiative linewidth.

As an example for the rest of this chapter we will consider the transition of a single mode; the TE$_1$, $n = 3$ mode of a CuCl PD. We have chosen CuCl as the PD material because it is cheap and widely used, particularly for making colloidal dots. The $n = 3$ mode was chosen because, as shown in figure 3.1, it is the first mode to lie within the strong coupling regime when a CuCl PD is surrounded by vacuum. Since the addition of a non-vacuum surrounding material will inevitably lead towards weaker-interacting modes, it is the natural choice.

Simulating a CuCl PD, just as in Chapter 3, we plot $\Gamma_n^{\mathrm{X}}(a)$ for values of ε_{d} above, below, and on the critical value, for a constant ω_{p}. The results are shown in figure 4.5. For $\varepsilon_{\mathrm{d}} = \varepsilon_{\mathrm{d}}^{\mathrm{cr}} = 1.495$ the plot forms a sharp "vertical wedge" shape, which is indicative of the transition point. When we differentiate the data with respect to the radius, this wedge produces a sharp jump in $d\Gamma_n^{\mathrm{X}}/da$ at the transition point, illustrated in figure 4.6. A similar discontinuity occurs in $d\Gamma_n^{\mathrm{X}}/d\varepsilon_{\mathrm{d}}$,

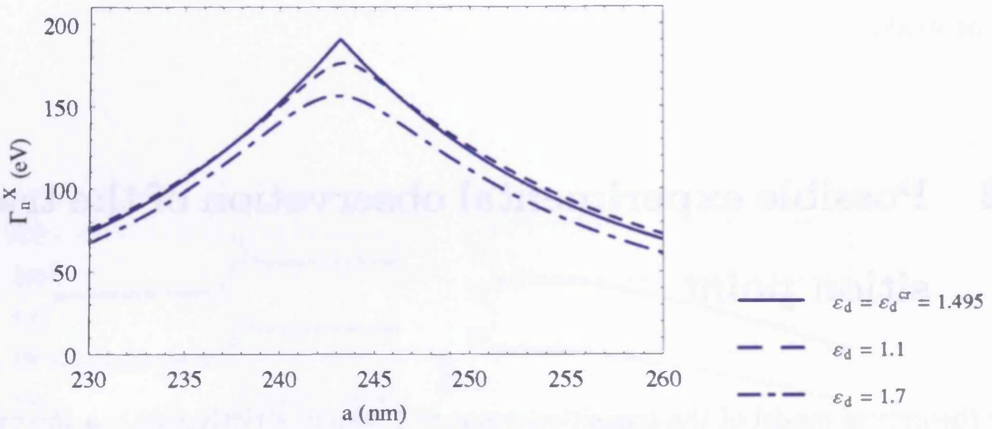

Figure 4.5: The total radiative linewidth of the $n = 3$ mode of a CuCl sphere as a function of the PD radius for different values of ε_{d}. The thick solid line shows that a sharp wedge forms at the transition point when the mode is at the transition point; $\varepsilon_{\mathrm{d}} = \varepsilon_{\mathrm{d}}^{\mathrm{cr}} = 1.495$.

shown in figure. 4.7, and we therefore propose that the transition point should be experimentally observable via these discontinuities, derived from the total radiative lifetime, using high-precision modulation spectroscopy methods [85].

In order to experimentally reproduce the figures discussed above it would be necessary to modulate ε_{d}. This may be achieved through sinusoidal temperature changes of a dielectric liquid surrounding the PD [86]. Alternatively, a pressure variation may be used, but this is less likely to be able to produce a wide change in ε_{d} for the transition to be easily observed. Other methods, such as modulation of an electric field, are undesirable as they will alter the excitonic states within the PD.

Whatever material is chosen to surround the PD it must have ε_{d} close to $\varepsilon_{\mathrm{d}}^{\mathrm{cr}} = 1.495$ and be transparent at 3.203 eV. Refractive index liquids, such as Cargille Laboratories' "immersion liquids", are strong candidates. These liquids are stable perfluorocarbons and their optical properties have been thoroughly measured and documented.

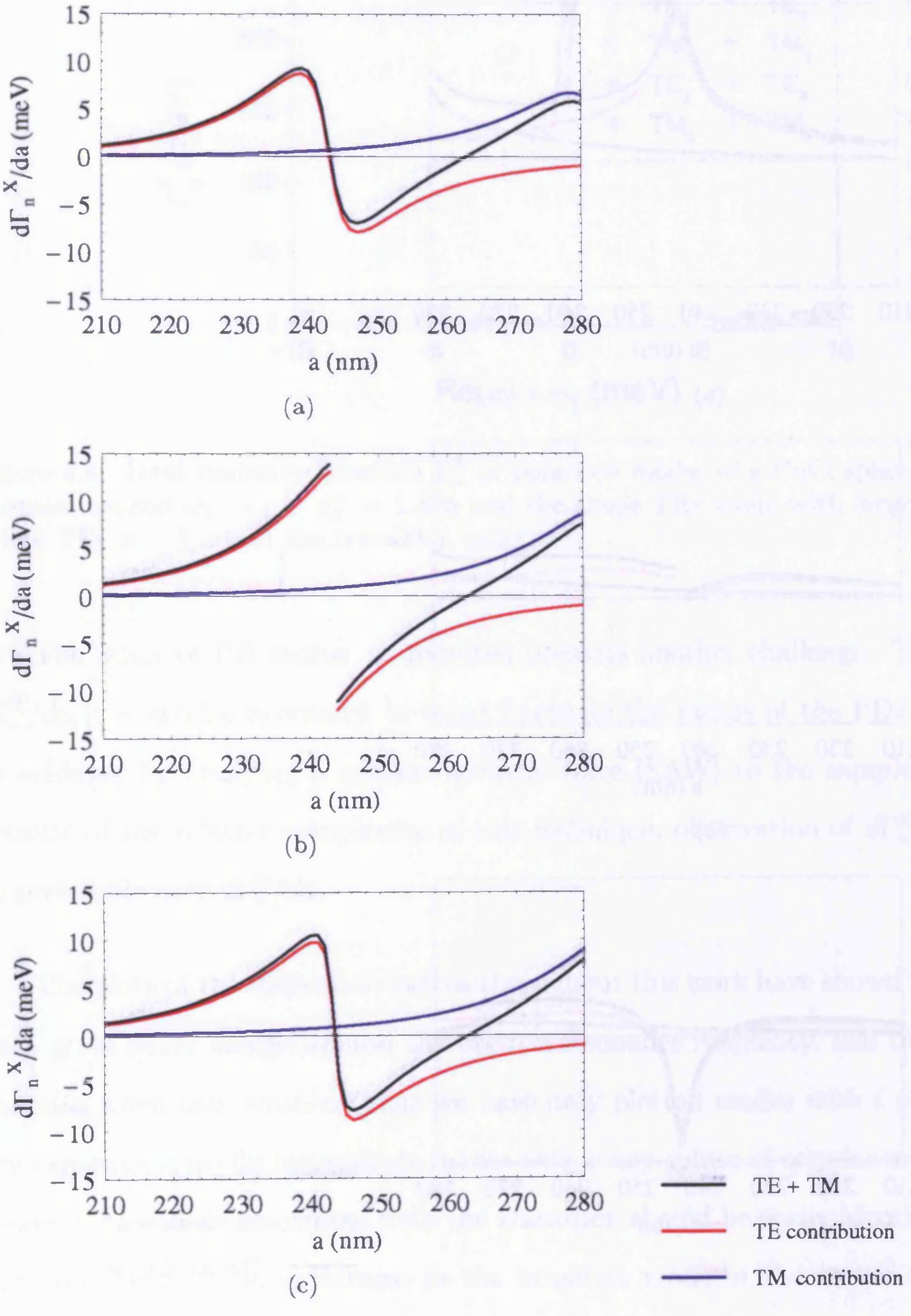

Figure 4.6: Plots of $d\Gamma^{X}_{n=3}/da(a)$ for the $n = 3$ mode of a CuCl PD for (a) $\varepsilon_{\mathrm{d}} = 1.1$, (b) $\varepsilon_{\mathrm{d}} = \varepsilon_{\mathrm{d}}^{\mathrm{cr}} = 1.495$, and (c) $\varepsilon_{\mathrm{d}} = 1.7$. While both the TE$_1$ and TM$_1$ modes contribute to $\Gamma^{X}_{n=3}$, the critical value $\varepsilon_{\mathrm{d}}^{\mathrm{cr}} \simeq 1.495$ refers to the transition associated with the TE$_1$ mode.

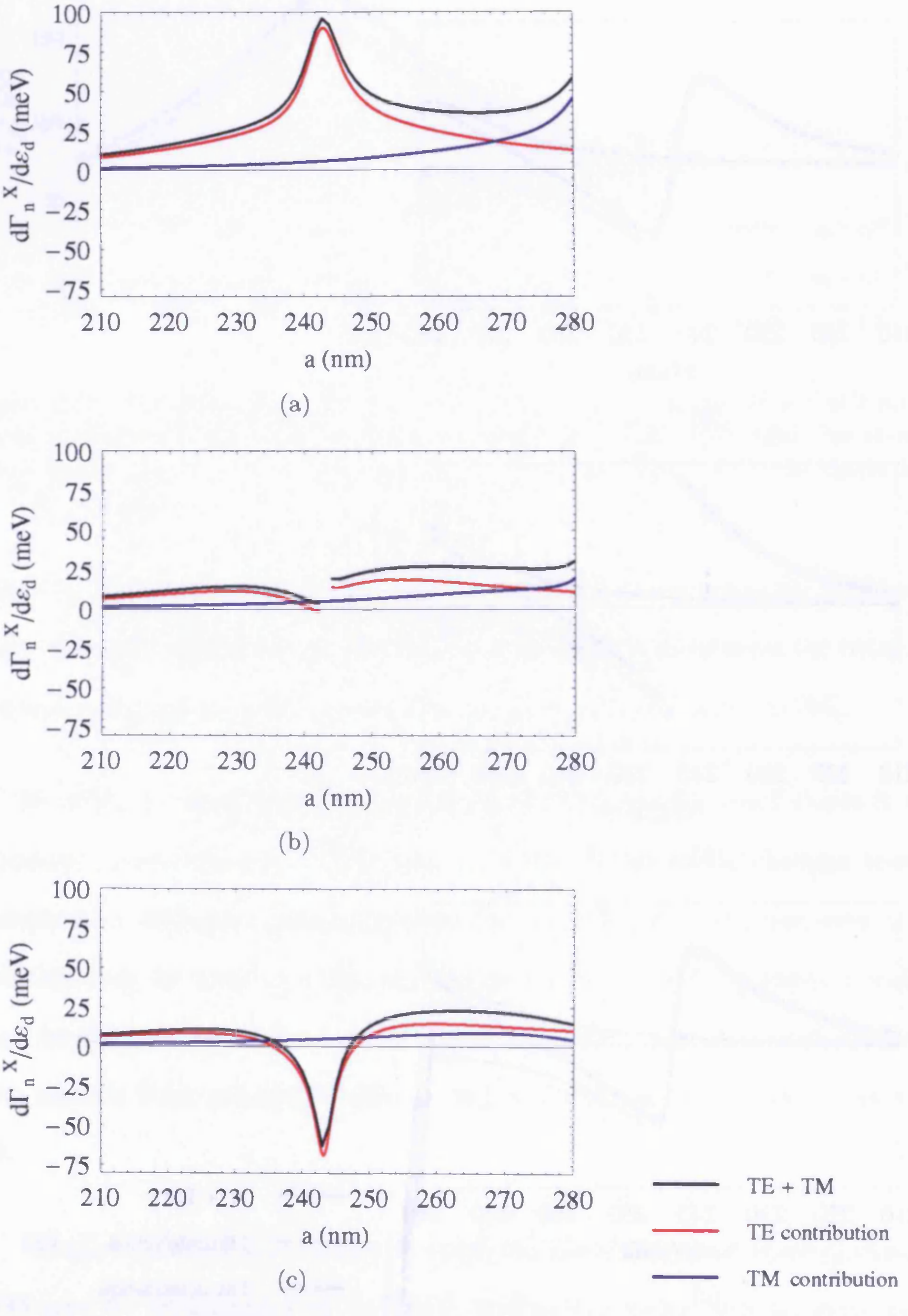

Figure 4.7: Plots of $d\Gamma^X_{n=3}/d\varepsilon_d(a)$ for the $n = 3$ mode of a CuCl PD for (a) $\varepsilon_d = 1.1$, (b) $\varepsilon_d = \varepsilon_d^{cr} = 1.495$, and (c) $\varepsilon_d = 1.7$. While both the TE$_1$ and TM$_1$ modes contribute to $\Gamma^X_{n=3}$, the critical value $\varepsilon_d^{cr} \simeq 1.495$ refers to the transition associated with the TE$_1$ mode.

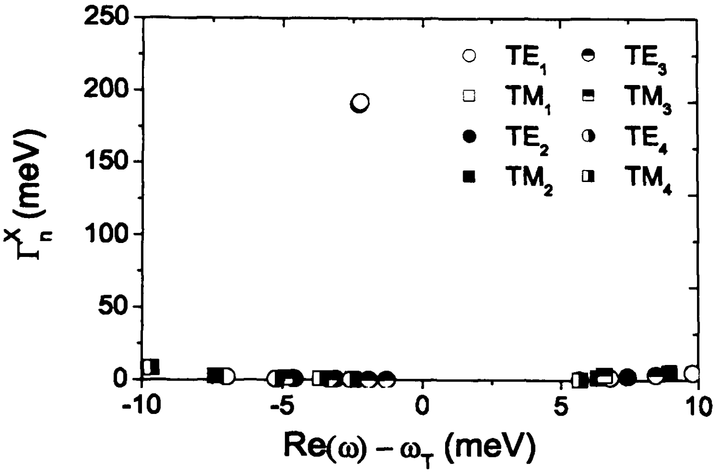

Figure 4.8: Total radiative lifewidth Γ^{X}_n of polariton modes of a CuCl sphere with frequencies around ω_{T}. $\varepsilon_{\mathrm{d}} = \varepsilon^{\mathrm{cr}}_{\mathrm{d}} = 1.495$ and the single TE_1 mode with large Γ^{X}_n is the bright $\mathrm{TE}_1, n = 3$ line at the transition point.

The range of PD radius, a, required presents another challenge. To produce $d\Gamma^{\mathrm{X}}_n/da$ it would be necessary to rapid fluctuate the radius of the PD. This may be achieved by applying a surface acoustic wave (SAW) to the sample [87], but because of the relative complexity of this technique, observation of $d\Gamma^{\mathrm{X}}_n/d\varepsilon_{\mathrm{d}}$ may be preferable over $d\Gamma^{\mathrm{X}}_n/da$.

The plots of the dispersion curves throughout this work have shown that there are a great many modes around the exciton resonance frequency, and this is compounded when one considers that we have only plotted modes with $l = 1$, whilst any experiment would incorporate modes with many values of angular momentum. However, the mode associated with the transition should be easily identifiable, despite the dense mode spectrum, as the brightest mode in the region of ω_{T}. In figure 4.8 we plot this region of the mode spectrum for values of angular momentum up to $l = 4$, and the TE_1 mode is clearly visible as having the highest value of Γ^X_n. In fact we can expect the observed value of Γ^X_n for the transition to be about double that shown in figure 4.8. This is because the numerical results effectively model the modes *just off* transition – it is impossible to model the transition with complete accuracy – and means that both branches are plotted on the graph. The raised TE_1 point can just be seen as being shadowed by another point. Experimentally the radiative linewidths of both branches effectively stack, doubling the value given in the figure.

4.3 Summary

We have identified the transition between the weak and strong polariton coupling regime as a discrete point at which the two branches of any given mode intersect in a three-dimensional space; $\mathrm{Re}(\omega)$, $\mathrm{Im}(\omega)$ and a. Only at this point do they have the same complex quasi-eigenfrequency. The regime in which a mode resides is dependent upon the the Rabi frequency of the PD material and the dielectric permittivities of the PD and surrounding material; ω_p, ε_b and ε_d. The transition point occurs for critical values of these parameters, and only at radii at which the photonic and excitonic parts of the dispersion cross – $\omega_\mathrm{p}^\mathrm{cr}$, $\tilde{\varepsilon}^\mathrm{cr}$, and a^cr – and values of these parameters have been obtained both numerically and analytically.

It may be useful, especially for experimentalists, to assume that the dielectric permittivity of the PD, ε_b is held constant, allowing the transition criticality to be transferred to the external dielectric, $\varepsilon_\mathrm{d} = \varepsilon_\mathrm{d}^\mathrm{cr}$. In fact ε_b is likely to fluctuate as a result of any experimental technique employed to change ε_d. In any case, sight of the true cause of the transition – that of $\tilde{\varepsilon}$ rather than ε_d – must not be lost.

The dependence of the regime of any given mode – and hence the transition point – upon ω_p, $\tilde{\varepsilon}$ and a can be interpreted as follows. The Rabi frequency is a measure of the inherent strength of exciton-photon interaction within the material, and does not depend on the size or shape of the structure. The ratio of the dielectric permittivities determines how strongly the photon is confined within the PD, and stronger confinement will lead to a greater degree of light-matter interaction. There is therefore an intrinsic factor, inherent to the material, and an extrinsic factor which is dependent upon the size and shape of the PD. The critical radius simply arises from the geometrical resonance of the photon field with the exciton resonance.

By examining the dispersion curves at the transition point we have identified a jump in the derivative of the total radiative linewidth, $d\Gamma_n^{\mathrm{X}}/d\varepsilon_{\mathrm{d}}$, which presents a parameter through which the transition point could be observed. We have proposed a scheme for this experiment using modulation spectroscopy, with a sinusoidal thermal variance used to induce a change in the dielectric permittivities, and a surface acoustic wave to fluctuate the radius of the PD.

Since the transition point is a general feature of PD polariton optics there is broad scope for experimental observation using many material systems, and modes with various angular momenta, l, and energy level, n. Our choice to model a CuCl PD means that it should be possible to produce a sphere of suitable radius using colloidal techniques. The choice of $n = 3$ results from the trade off between the required ε_{d} and a_n^{cr}. For higher n, $\varepsilon_{\mathrm{d}}^{\mathrm{cr}}$ rises which may offer a greater range of surrounding medium, but the CuCl PD must have a larger radius.

The results of this chapter parallel the work by Tait on the polariton transition in bulk semiconductors, however, the work presented here differs in several key respects beyond the fact that we deal with a nanostructure. In his work the bulk polariton dispersions lie within (Re(k), Im(k), ω) space, whilst our PD polaritons correspond to (Re(ω), Im(ω), a). In his work the transition was achieved by varying the degree of incoherent scattering to achieve a transition between undamped, strongly-coupled polaritons and strongly-damped polaritons. We neglect incoherent scattering to show the transition between weakly-coupled polaritons and strongly-coupled polaritons within a completely coherent framework.

Chapter 5

Conclusions

The main aim of this thesis has been to describe the completely coherent polariton optics of a spherical semiconductor nanostructure. The model developed in Chapter 2 solves the eigen-modes of the system to produce the polariton frequencies as a function of the PD radius, $\omega(a)$, in contrast to bulk polariton frequencies which are a function of the wavevector; $\omega(\mathbf{k})$. These dispersion curves are then classified into the weak and strong coupling regimes depending on whether they exhibit crossing or anti-crossing of the polariton branches, in direct analogy with polaritons in bulk materials. The removal of incoherent scattering creates a picture of the completely coherent polariton optics of the PD, where the photonic modes with $\lambda = 2a$ are resonant with the sphere. We maintain this coherent picture by distributing the polariton energy coherently between the photonic and excitonic branches in order to calculate the total radiative linewidth.

Our choice of a cyanine dye J-aggregate material as our main example material for this dispersionless model is partly a matter of necessity; though there are many dielectric materials which are both homogeneous and optically isotropic, there are few which also have excitons which are truly dispersionless. However, the current interest in these disordered organic semiconductors has put them at the forefront of research. The development of our dispersionless model in Chapter 2, which is simple and elegant whilst maintaining accuracy and applicability, is therefore very timely.

Chapter 3.1 considers the effect of spatial dispersion of excitons using the dispersion equations developed by Ruppin and the Pekar Additional Boundary Condition. The asymptotic values of the resulting dispersion curves are shown to agree with the results of Ajiki *et al.* [55]. However plots of the dispersion curves for a CuCl PD show that the TE_1, $n = 1$ and 2 modes are in the weak coupling regime, whilst $n = 3$ and 4 are in the strong regime. This contrasts with similar results by Ajiki *et al.* showing all of these modes in the weak regime due to the approximations used in that paper.

Our analysis of the radiative linewidth, both including and excluding spatial dispersion, produces a $1/a$ dependence for Γ_n for large radii. This corresponds to the "ballistic escape" of optically-dressed excitons from the PD. The low-radius behaviour has been shown to be more complicated. Excluding spatial dispersion we observe a clear a^3 dominance from the Fröhlich mode, corresponding to the volume dependent increase of the oscillator strength, whilst a^7 is observed for other TM_1 modes and a^5 is observed for TE_1 modes. In the presence of spatial dispersion, numerical results support the decrease of these dependencies to a^1 and a^5 for TM_1 and TE_1 modes respectively at *very* low radius. This contradiction with the well-known volume dependent increase of the oscillator strength is explained as the violation of the long wavelength approximation (LWA) upon which it is based.

Chapters 2 and 3 formed the basis for analysing the transition between the polariton coupling regimes. The identification of the transition as the discrete point at which the two polariton branches meet is a simple, natural definition, but a critical concept for all of the work that follows. We have shown that the regime in which a mode resides is determined by the inherent oscillator strength of the PD material (described by ω_{p}) and the degree of light trapping within the PD (governed by the permittivities of the PD and the surrounding medium). Equations for the critical values of the these parameters, along with the radius, at which the transition point occurs have been derived, though truly accurate values can only be obtained numerically. The transition in bulk materials, analysed by Tait as a function of incoherent scattering several decades ago, has thus been completely described within a spherical geometry as a purely coherent phenomena.

The unique nature of the transition as the meeting of the polariton branches leads to a discrete jump in the derivative of the radiative linewidth, $d\Gamma_n^{\mathrm{X}}/da$ or $d\Gamma_n^{\mathrm{X}}/d\tilde{\varepsilon}$, presenting an observable parameter through which the transition point can be experimentally observed. We have outlined a scheme through which this could be achieved using high-precision modulation spectroscopy.

5.1 Future outlook

The main prospect for future work from this thesis is the experimental verification of the transition point. The main obstacles to performing such an experiment are obtaining a suitable sample, and achieving the required modulation of the parameters; $\tilde{\varepsilon}$ and a. Colloidal dots offer the best hope for obtaining a sample with the required geometry and radius; dots grown through Stranski-Krastanov methods are significantly non-spherical, and are generally not grown large enough to provide the required radius. The use of sinusoidal temperature variance to modulate the dielectric permittivities, and a surface acoustic wave to fluctuate the radius of the PD, is speculative but based on the results of published experiments. Although the author would not wish to suggest that such an experiment would be *easy*, it is within the realm of possibility.

From a theoretical viewpoint there are several possible extensions to this work, largely based around additional complications to the model. For example, the model could be extended to include a layer (or multiple layers) surrounding the PD, instead of our infinite medium. Just a single layer would allow the model to more accurately model a colloidal dot, which typically grow with an inhomogeneous material composition such that a thin layer around the outside of the dot has a different composition to the core.

The dispersionless model can be used almost its exact current form to model a spherical PD which does *not* have an excitonic resonance, surrounded by a material that does. An example would be a porous semiconductor, where a spherical pore could be treated as a vacuum sphere with appropriate radius surrounded by the semiconductor.

The most interesting area of development may be to perform a similar analysis of the transition point within a more complex geometry. Spheroidal geometry is of particular interest and has received considerable attention in the literature in recent years. It offers the potential to more accurately model a Stranski-Krastinov dot, but at the cost of significantly more complex dispersion equations.

Perhaps the greatest potential in this research lies beyond what can easily be foreseen. The transition point offers some interesting physical phenomena, notably a strong enhancement of Γ^X at the transition point. It may prove to offer a novel method of examining light-trapping within nanostructures, or spawn a new breed of applications and devices based around the transition point's specific qualities.

Chapter 6

Appendix

This appendix covers topics which support the research presented in this thesis. The next section contains a full derivation of the polariton dispersion equations equations excluding spatial dispersion. Section 6.2 goes on to derive the dispersion equations for $l = 0$ modes, and indentifies a correlation between $l = 0$ and $l = 1$ modes which proves useful as an analytical approximation. Section 6.3 covers various aspects relating to the Mathematica package and its use in obtaining the numerical results presented in the main body of the text, and is followed by a discussion in Section 6.4 on complex slices as a tool for presenting those results.

6.1 Derivation of polariton dispersion equations excluding spatial dispersion

Here is a detailed derivation of the polariton dispersion equations excluding spatial dispersion, which are the basis of the work in Chapter 2. We derive the dispersion equations which describe how light is emitted from a dielectric sphere surrounded by another material. Each material has a magnetic permittivity, μ, and dielectric constant, ε, associated with it. Although our initial derivation will include a change in μ between the sphere and the surrounding media, this difference will be removed from our final solutions so that the resulting dispersion equations describe modes due solely to the effect of the change in ε. Throughout this section we closely follow the derivation of Weng Cho Chew [88].

We first solve this problem by describing it as a transmissivity problem, where there is a source at the center of the sphere. In this case the problem is entirely homogeneous and ω remains real. We then re-set the problem as an eigenvalue problem, to show that the same result can be obtained but now using a complex frequency.

6.1.1 Vector wave equation in spherical coordinates

To solve the vector wave equation in spherical coordinates we introduce the Debye potentials π_e and π_m to describe the transverse-electric, TE, and transverse-magnetic, TM, modes respectively. The $\mathbf{H}$ and $\mathbf{E}$ fields are then of the form

$$\begin{aligned} \mathbf{H} &= \nabla \times \mathbf{r}\pi_e + \frac{1}{i\omega\mu}\nabla \times \nabla \times \mathbf{r}\pi_m, \\ \mathbf{E} &= \nabla \times \mathbf{r}\pi_m - \frac{1}{i\omega\varepsilon}\nabla \times \nabla \times \mathbf{r}\pi_e, \end{aligned} \tag{6.1}$$

with π_e and π_m having general solutions of the form

$$\left\{ \begin{array}{c} j_l(kr) \\ h_l(kr) \end{array} \right\} P_l^m(\cos\theta) \left\{ \begin{array}{c} \cos m\phi \\ \sin m\phi \end{array} \right\} \tag{6.2}$$

Here the curly brackets indicate a linear superposition of terms, and the functions $j_l(x)$ and $h_l(x)$ are the spherical Bessel functions of the first and third kind respectively. The latter is often denoted as $h_n^{(1)}$, but the superscript is dropped here for brevity. In this work the order of these functions, often written as n, equates to the angular momentum quantum number, l, and is denoted as such throughout. $P_l^m(x)$ is an associated Legendre polynomial.

We can now extract the r, θ, and ϕ components of the field. The radial components give

$$H_r = \frac{1}{i\omega\mu}\left[\frac{\partial^2}{\partial r^2}r\pi_m + k^2 r\pi_m\right],$$

$$E_r = -\frac{1}{i\omega\varepsilon}\left[\frac{\partial^2}{\partial r^2}r\pi_e + k^2 r\pi_e\right], \tag{6.3}$$

which can be simplified using the identity

$$\frac{\partial^2}{\partial r^2}\begin{bmatrix} r\pi_m \\ r\pi_e \end{bmatrix} = -\left[k^2 - \frac{l(l+1)}{r}\right]\begin{bmatrix} r\pi_m \\ r\pi_e \end{bmatrix}, \tag{6.4}$$

to give

$$H_r = \frac{1}{i\omega\mu}\frac{l(l+1)}{r}\pi_m,$$

$$E_r = -\frac{1}{i\omega\varepsilon}\frac{l(l+1)}{r}\pi_e. \tag{6.5}$$

The θ, and ϕ components can be extracted from (6.1) to give the components tangential to the surface as

$$\mathbf{H}_s = -\mathbf{r}\times\nabla_s\pi_e + \frac{1}{i\omega\mu}\frac{1}{r}\frac{\partial}{\partial r}\left[r^2\nabla_s\pi_m\right],$$

$$\mathbf{E}_s = -\mathbf{r}\times\nabla_s\pi_m - \frac{1}{i\omega\varepsilon}\frac{1}{r}\frac{\partial}{\partial r}\left[r^2\nabla_s\pi_e\right]. \tag{6.6}$$

These can be rearranged to give

$$
\begin{aligned}
\mathbf{H}_s &= \begin{bmatrix} H_\theta \\ H_\phi \end{bmatrix}, \\
&= \begin{bmatrix} \frac{1}{\sin\theta}\frac{\partial}{\partial\phi} & \frac{-i}{\omega\mu}\frac{1}{r}\frac{\partial^2}{\partial r\partial\theta}r \\ -\frac{\partial}{\partial\theta} & \frac{-i}{\omega\mu}\frac{1}{r\sin\theta}\frac{\partial^2}{\partial r\partial\phi}r \end{bmatrix} \begin{bmatrix} \pi_e \\ \pi_m \end{bmatrix}, \qquad (6.7) \\
&= \begin{bmatrix} \frac{\partial}{\partial\theta} & \frac{-1}{\sin\theta}\frac{\partial}{\partial\phi} \\ \frac{1}{\sin\theta}\frac{\partial}{\partial\phi} & \frac{\partial}{\partial\theta} \end{bmatrix} \begin{bmatrix} 0 & \frac{-i}{\omega\mu}\frac{1}{r}\frac{\partial}{\partial r}r \\ -1 & 0 \end{bmatrix} \begin{bmatrix} \pi_e \\ \pi_m \end{bmatrix},
\end{aligned}
$$

and

$$
\begin{aligned}
\mathbf{E}_s &= \begin{bmatrix} E_\theta \\ E_\phi \end{bmatrix}, \\
&= \begin{bmatrix} \frac{i}{\omega\varepsilon}\frac{1}{r}\frac{\partial^2}{\partial r\partial\theta}r & \frac{1}{\sin\theta}\frac{\partial}{\partial\phi} \\ \frac{i}{\omega\varepsilon}\frac{1}{r\sin\theta}\frac{\partial^2}{\partial r\partial\phi}r & -\frac{\partial}{\partial\theta} \end{bmatrix} \begin{bmatrix} \pi_e \\ \pi_m \end{bmatrix}, \qquad (6.8) \\
&= \begin{bmatrix} \frac{\partial}{\partial\theta} & \frac{-1}{\sin\theta}\frac{\partial}{\partial\phi} \\ \frac{1}{\sin\theta}\frac{\partial}{\partial\phi} & \frac{\partial}{\partial\theta} \end{bmatrix} \begin{bmatrix} \frac{i}{\omega\varepsilon}\frac{1}{r}\frac{\partial}{\partial r}r & 0 \\ 0 & -1 \end{bmatrix} \begin{bmatrix} \pi_e \\ \pi_m \end{bmatrix}.
\end{aligned}
$$

We can write the Debye potentials in the general form

$$
\begin{pmatrix} \pi_e \\ \pi_m \end{pmatrix} = \left[\mathbf{a} j_l(kr) + \mathbf{b} h_l(kr)\right] P_l^m(\cos\theta)\, e^{im\phi}, \qquad (6.9)
$$

where **a** and **b** are column vectors. Substituting this into (6.7) and (6.8), we finally obtain

$$\mathbf{H}_s = \overline{\mathbf{P}}_l^m(\cos\theta)\cdot\left[\overline{\mathbf{j}}_{lh}(kr)\cdot\mathbf{a}+\overline{\mathbf{h}}_{lh}(kr)\cdot\mathbf{b}\right]\cdot e^{im\phi},$$

$$\mathbf{E}_s = \overline{\mathbf{P}}_l^m(\cos\theta)\cdot\left[\overline{\mathbf{j}}_{le}(kr)\cdot\mathbf{a}+\overline{\mathbf{h}}_{le}(kr)\cdot\mathbf{b}\right]\cdot e^{im\phi}, \tag{6.10}$$

where

$$\overline{\mathbf{P}}_l^m(\cos\theta) = \begin{bmatrix} \frac{\partial}{\partial\theta}P_l^m(\cos\theta) & \frac{-im}{\sin\theta}P_l^m(\cos\theta) \\ \\ \frac{im}{\sin\theta}P_l^m(\cos\theta) & \frac{\partial}{\partial\theta}P_l^m(\cos\theta) \end{bmatrix}, \tag{6.11}$$

$$\overline{\mathbf{b}}_{le}(kr) = \begin{bmatrix} \frac{1}{\omega\varepsilon}\frac{1}{r}\frac{\partial}{\partial r}rb_l(kr) & 0 \\ 0 & -b_l(kr) \end{bmatrix}, \tag{6.12}$$

and

$$\overline{\mathbf{b}}_{lh}(kr) = \begin{bmatrix} 0 & -\frac{1}{\omega\mu}\frac{1}{r}\frac{\partial}{\partial r}rb_l(kr) \\ -b_l(kr) & 0 \end{bmatrix}. \tag{6.13}$$

The function b_l can be either j_l or h_l.

6.1.2 Reflection of waves at a spherical boundary

Having established base equations for solving the vector wave equation in spherical coordinates we now proceed to solve the problem of the light modes of a dielectric sphere in terms of a transmissivity problem. Consider a source at the center of the sphere shown in figure 6.1. The outgoing wave in region 1 will strike the spherical boundary at $r = a$ and be partially reflected. This will set up a standing wave inside the sphere and a purely outgoing wave outside of it, in region 2. Solutions for the problem can then be found via the determination of the reflection and transmission coefficients as functions of the frequency.

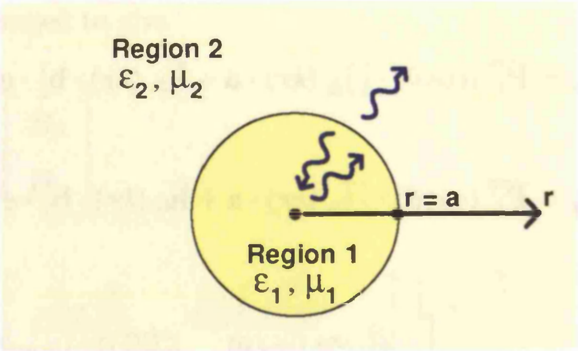

Figure 6.1: Diagram illustrating the transmissivity problem of waves reflected from a spherical boundary. The source at the center of region 1 emits waves which are partially reflected at the boundary at $r = a$.

Since we consider a source at the center of the sphere we need not worry about maintaining a finite field at $r = 0$. The standing wave within region 1 will result in a field of the form

$$\mathbf{H}_{1s} = \overline{\mathbf{P}}_l^m(\cos\theta) \cdot \left[\overline{\mathbf{h}}_{lh}(k_1 r) + \overline{\mathbf{j}}_{lh}(k_1 r) \cdot \overline{\mathbf{R}}_{12}\right] \cdot \mathbf{a},$$

$$\mathbf{E}_{1s} = \overline{\mathbf{P}}_l^m(\cos\theta) \cdot \left[\overline{\mathbf{h}}_{le}(k_1 r) + \overline{\mathbf{j}}_{le}(k_1 r) \cdot \overline{\mathbf{R}}_{12}\right] \cdot \mathbf{a}. \tag{6.14}$$

In re
regio

In region 2 the transmitted wave is an outgoing wave only, and hence the field in region 2 is

$$\mathbf{H}_{2s} = \overline{\mathbf{P}}_l^m(\cos\theta) \cdot \overline{\mathbf{h}}_{lh}(k_2 r) \cdot \overline{\mathbf{T}}_{12} \cdot \mathbf{a},$$

$$\mathbf{E}_{2s} = \overline{\mathbf{P}}_l^m(\cos\theta) \cdot \overline{\mathbf{h}}_{le}(k_2 r) \cdot \overline{\mathbf{T}}_{12} \cdot \mathbf{a}. \tag{6.15}$$

(6.15)

In the above equations we have dropped the $e^{im\phi}$ dependence. In addition the orthogonality of the $\overline{\mathbf{P}}_l^m$ harmonics means that all of the l harmonics are decoupled, and only a single harmonic need be considered at a time.

Applying the boundary conditions

$$\begin{gathered}\mathbf{H}_{1s}\big|_{r=a} = \mathbf{H}_{2s}\big|_{r=a}, \\ \mathbf{E}_{1s}\big|_{r=a} = \mathbf{E}_{2s}\big|_{r=a},\end{gathered} \tag{6.16}$$

to (6.14) and (6.15) gives

$$\begin{gathered}\overline{\mathbf{h}}_{lh}\left(k_1 r\right) + \overline{\mathbf{j}}_{lh}\left(k_1 r\right) \cdot \overline{\mathbf{R}}_{12} = \overline{\mathbf{h}}_{lh}\left(k_2 r\right) \cdot \overline{\mathbf{T}}_{12}, \\ \overline{\mathbf{h}}_{le}\left(k_1 r\right) + \overline{\mathbf{j}}_{le}\left(k_1 r\right) \cdot \overline{\mathbf{R}}_{12} = \overline{\mathbf{h}}_{le}\left(k_2 r\right) \cdot \overline{\mathbf{T}}_{12}.\end{gathered} \tag{6.17}$$

Since we know the form of the components of $\overline{\mathbf{b}}_{le}$ and $\overline{\mathbf{b}}_{le}$, given by (6.12) and (6.13) respectively, we can rewrite these equations in symbolic form

$$\begin{gathered}\begin{pmatrix} a_1 & 0 \\ 0 & a2 \end{pmatrix} + \begin{pmatrix} b_1 & 0 \\ 0 & b2 \end{pmatrix}\begin{pmatrix} R_1 & R_2 \\ R_3 & R_4 \end{pmatrix} = \begin{pmatrix} c_1 & 0 \\ 0 & c2 \end{pmatrix}\begin{pmatrix} T_1 & T_2 \\ T_3 & T_4 \end{pmatrix}, \\ \begin{pmatrix} 0 & d_1 \\ d_2 & 0 \end{pmatrix} + \begin{pmatrix} 0 & e_1 \\ e_2 & 0 \end{pmatrix}\begin{pmatrix} R_1 & R_2 \\ R_3 & R_4 \end{pmatrix} = \begin{pmatrix} 0 & f_1 \\ f_2 & 0 \end{pmatrix}\begin{pmatrix} T_1 & T_2 \\ T_3 & T_4 \end{pmatrix},\end{gathered} \tag{6.18}$$

which allows us to more clearly solve to get eight simultaneous equations

$$\begin{array}{cc} a_1 + b_1 R_1 = c_1 T_1, & d_2 + e_2 R_1 = f_2 T_1, \\ b_1 R_2 = c_1 T_2, & e_2 R_2 = f_2 T_2, \\ b_2 R_3 = c_2 T_3, & e_1 R_3 = f_1 T_3, \\ a_2 + b_2 R_4 = c_2 T_4, & d_1 + e_1 R_4 = f_1 T_4. \end{array} \tag{6.19}$$

In the above nothing has been assumed about the form of the matrices $\overline{\mathbf{R}}_{12}$ and $\overline{\mathbf{T}}_{12}$. We will now show that R_2 and R_3 are in fact zero. By taking the two equations above that refer to R_2, and casting them in matrix form

$$\begin{pmatrix} b_1 & c_1 \\ e_2 & f_2 \end{pmatrix} \begin{pmatrix} R_2 \\ T_2 \end{pmatrix} = 0, \tag{6.20}$$

it can be seen that in general R_2 and T_2 will be zero except when

$$\begin{vmatrix} b_1 & c_1 \\ e_2 & f_2 \end{vmatrix} = 0. \tag{6.21}$$

In a similar manner it is possible to show that the same applies for R_3 and T_3. We have thus shown that $\overline{\mathbf{R}}_{12}$ and $\overline{\mathbf{T}}_{12}$ are diagonal, implying that the TE and TM waves are decoupled.

We can hence define

$$\overline{\mathbf{R}}_{12} = \begin{pmatrix} R_{12}^{TM} & 0 \\ 0 & R_{12}^{TE} \end{pmatrix}, \tag{6.22}$$

and proceed to define R_{12}^{TM} as follows. Taking the parts of (6.19) relating to R_1, and equating them gives

$$\frac{a_1}{c_1} + \frac{b_1}{c_1} R_1 = \frac{d_2}{f_2} + \frac{e_2}{f_2} R_1, \tag{6.23}$$

so that

$$R_{12}^{TM} = R_1 = \frac{\dfrac{a_1}{c_1} - \dfrac{d_2}{f_2}}{\dfrac{e_2}{f_2} - \dfrac{b_1}{c_1}}. \tag{6.24}$$

Referring back to previous equations and substituting in the $\overline{\mathbf{b}}_{te}$ and $\overline{\mathbf{b}}_{th}$ components gives

$$R_{12}^{TM} = \frac{\dfrac{\dfrac{1}{\omega_1\varepsilon_1}\dfrac{\partial}{\partial a}\left[a\cdot h_l\left(k_1a\right)\right]}{\dfrac{1}{\omega_2\varepsilon_2}\dfrac{\partial}{\partial a}\left[a\cdot h_l\left(k_2a\right)\right]} - \dfrac{h_l\left(k_1a\right)}{h_l\left(k_2a\right)}}{\dfrac{j_l\left(k_1a\right)}{h_l\left(k_2a\right)} - \dfrac{\dfrac{1}{\omega_1\varepsilon_1}\dfrac{\partial}{\partial a}\left[a\cdot j_l\left(k_1a\right)\right]}{\dfrac{1}{\omega_2\varepsilon_2}\dfrac{\partial}{\partial a}\left[a\cdot h_l\left(k_2a\right)\right]}}, \tag{6.25}$$

$$= \frac{\dfrac{1}{\omega_1\varepsilon_1}\dfrac{\partial}{\partial a}\left[a\cdot h_l\left(k_1a\right)\right]\cdot h_l\left(k_2a\right) - \dfrac{1}{\omega_2\varepsilon_2}\dfrac{\partial}{\partial a}\left[a\cdot h_l\left(k_2a\right)\right]\cdot h_l\left(k_1a\right)}{\dfrac{1}{\omega_2\varepsilon_2}\dfrac{\partial}{\partial a}\left[a\cdot h_l\left(k_2a\right)\right]\cdot j_l\left(k_1a\right) - \dfrac{1}{\omega_1\varepsilon_1}\dfrac{\partial}{\partial a}\left[a\cdot j_l\left(k_1a\right)\right]\cdot h_l\left(k_2a\right)}.$$

We can substitute in for ω_1 and ω_2 using [43]

$$k = \tfrac{\omega}{c}\sqrt{\varepsilon\mu}, \tag{6.26}$$

which can more conveniently be expressed as;

$$\omega_i = \frac{k_i c}{\sqrt{\varepsilon_i\mu_i}}, \tag{6.27}$$

giving

$$R_{12}^{TM} = \frac{k_2\sqrt{\varepsilon_2\mu_1}\frac{\partial}{\partial a}\left[a\cdot h_l(k_1a)\right]\cdot h_l(k_2a) - k_1\sqrt{\varepsilon_1\mu_2}\frac{\partial}{\partial a}\left[a\cdot h_l(k_2a)\right]\cdot h_l(k_1a)}{k_1\sqrt{\varepsilon_1\mu_2}\frac{\partial}{\partial a}\left[a\cdot h_l(k_2a)\right]\cdot j_l(k_1a) - k_2\sqrt{\varepsilon_2\mu_1}\frac{\partial}{\partial a}\left[a\cdot j_l(k_1a)\right]\cdot h_l(k_2a)}. \tag{6.28}$$

We now introduce the functions

$$\begin{aligned} J_l\left(x\right) &= x\cdot j_l\left(x\right), \\ H_l\left(x\right) &= x\cdot h_l\left(x\right), \end{aligned} \tag{6.29}$$

to give

$$R_{12}^{TM} = \frac{\sqrt{\varepsilon_2\mu_1}\frac{\partial}{\partial a}\left[a \cdot h_l\left(k_1 a\right)\right] \cdot H_l\left(k_2 a\right) - \sqrt{\varepsilon_1\mu_2}\frac{\partial}{\partial a}\left[a \cdot h_l\left(k_2 a\right)\right] \cdot H_l\left(k_1 a\right)}{\sqrt{\varepsilon_1\mu_2}\frac{\partial}{\partial a}\left[a \cdot h_l\left(k_2 a\right)\right] \cdot J_l\left(k_1 a\right) - \sqrt{\varepsilon_2\mu_1}\frac{\partial}{\partial a}\left[a \cdot j_l\left(k_1 a\right)\right] \cdot H_l\left(k_2 a\right)} \tag{6.30}$$

This can be further simplified using the following proof that for an arbitrary spherical Bessel function, f,

$$\begin{aligned} \frac{\partial}{\partial a}\left[a \cdot f(ka)\right] &= a \cdot \frac{\partial}{\partial a}\left[f(ka)\right] + f(ka) \\ &= ka \cdot \frac{\partial}{\partial ka}\left[f(ka)\right] + f(ka) \quad = \frac{\partial}{\partial ka}\left[ka \cdot f(ka)\right], \end{aligned} \tag{6.31}$$

which finally gives the reflection coefficient as

$$R_{12}^{TM} = \frac{\sqrt{\varepsilon_2\mu_1}H_l'\left(k_1 a\right) \cdot H_l\left(k_2 a\right) - \sqrt{\varepsilon_1\mu_2}H_l'\left(k_2 a\right) \cdot H_l\left(k_1 a\right)}{\sqrt{\varepsilon_1\mu_2}H_l'\left(k_2 a\right) \cdot J_l\left(k_1 a\right) - \sqrt{\varepsilon_2\mu_1}J_l'\left(k_1 a\right) \cdot H_l\left(k_2 a\right)}. \tag{6.32}$$

By duality we can now immediately transform the TM reflection coefficient using [2]

$$\varepsilon \longrightarrow -\mu,\ \mu \longrightarrow -\varepsilon, \tag{6.33}$$

to define the coefficient of reflection for TE polarised waves,

$$R_{12}^{TE} = \frac{\sqrt{\varepsilon_1\mu_2}H_l'\left(k_1 a\right) \cdot H_l\left(k_2 a\right) - \sqrt{\varepsilon_2\mu_1}H_l'\left(k_2 a\right) \cdot H_l\left(k_1 a\right)}{\sqrt{\varepsilon_2\mu_1}H_l'\left(k_2 a\right) \cdot J_l\left(k_1 a\right) - \sqrt{\varepsilon_1\mu_2}J_l'\left(k_1 a\right) \cdot H_l\left(k_2 a\right)}. \tag{6.34}$$

Transmission coefficients can be found using a similar method, but are unnecessary for the proceeding derivation.

The TM and TE modes of the dielectric sphere can then be found when the respective reflection coefficient is at a maximum. This occurs when the denominator of the coefficients given above is equal to zero, giving a transcendental equation.

Modes can then be found by scanning through the frequency ω, included in the above equations as part of k.

6.1.3 Eigenvalue problem

We now alter the problem to that of solving the eigenvalue problem for the dielectric sphere. In doing so we will prove the assertion above that the TM and TE modes can be solved from the denominators of the reflection and transmission coefficients.

Consider the dielectric sphere with surrounding material as shown in figure 6.1, where there is now no source at the center of the sphere. We choose forms for the field inside and outside of the sphere such that there is a finite field at the center of the sphere, and an outgoing field in the surrounding medium. These conditions are satisfied by the functions $j_l\left(kr\right)$ and $h_l\left(kr\right)$ respectively.

The tangential components of the fields inside the sphere are then given by

$$\begin{gathered}\begin{pmatrix} \mathbf{H}^1_\theta \\ \mathbf{H}^1_\phi \end{pmatrix} = \overline{\mathbf{P}}^m_l(\cos\theta)\cdot\bar{\mathbf{j}}_{lh}(k_1 r)\cdot\begin{pmatrix} \mathbf{a}_1 \\ \mathbf{a}_2 \end{pmatrix}\cdot e^{im\phi}, \\ \begin{pmatrix} \mathbf{E}^1_\theta \\ \mathbf{E}^1_\phi \end{pmatrix} = \overline{\mathbf{P}}^m_l(\cos\theta)\cdot\bar{\mathbf{j}}_{le}(k_1 r)\cdot\begin{pmatrix} \mathbf{a}_1 \\ \mathbf{a}_2 \end{pmatrix}\cdot e^{im\phi},\end{gathered} \tag{6.35}$$

and in the surrounding material by

$$\begin{pmatrix} \mathbf{H}_\theta^2 \\ \mathbf{H}_\phi^2 \end{pmatrix} = \overline{\mathbf{P}}_l^m(\cos\theta) \cdot \overline{\mathbf{h}}_{lh}(k_2 r) \cdot \begin{pmatrix} \mathbf{b}_1 \\ \mathbf{b}_2 \end{pmatrix} \cdot e^{im\phi},$$

$$\begin{pmatrix} \mathbf{E}_\theta^2 \\ \mathbf{E}_\phi^2 \end{pmatrix} = \overline{\mathbf{P}}_l^m(\cos\theta) \cdot \overline{\mathbf{h}}_{le}(k_2 r) \cdot \begin{pmatrix} \mathbf{b}_1 \\ \mathbf{b}_2 \end{pmatrix} \cdot e^{im\phi}, \tag{6.36}$$

We can apply the boundary condition that the tangential components of the electric and magnetic fields must be continuous at the boundary,

$$\mathbf{H}_\theta^1|_{r=a} = \mathbf{H}_\theta^2|_{r=a}, \quad \mathbf{H}_\phi^1|_{r=a} = \mathbf{H}_\phi^2|_{r=a},$$

$$\mathbf{E}_\theta^1|_{r=a} = \mathbf{E}_\theta^2|_{r=a}, \quad \mathbf{E}_\phi^1|_{r=a} = \mathbf{E}_\phi^2|_{r=a}. \tag{6.37}$$

to obtain

$$\overline{\mathbf{j}}_{lh}(k_1 r)\,|_{r=a} \cdot \begin{pmatrix} \mathbf{a}_1 \\ \mathbf{a}_2 \end{pmatrix} = \overline{\mathbf{h}}_{lh}(k_2 r)\,|_{r=a} \cdot \begin{pmatrix} \mathbf{b}_1 \\ \mathbf{b}_2 \end{pmatrix}, \tag{6.38}$$

and

$$\overline{\mathbf{j}}_{le}(k_1 r)\,|_{r=a} \cdot \begin{pmatrix} \mathbf{a}_1 \\ \mathbf{a}_2 \end{pmatrix} = \overline{\mathbf{h}}_{le}(k_2 r)\,|_{r=a} \cdot \begin{pmatrix} \mathbf{b}_1 \\ \mathbf{b}_2 \end{pmatrix}. \tag{6.39}$$

These two conditions will allow us to derive the transcendental equations for the TM and TE modes.

Substituting (6.12) and (6.13) into (6.39) gives

$$\begin{pmatrix} \frac{1}{\omega_1\varepsilon_1}\frac{1}{a}\frac{\partial}{\partial a}\left[a\cdot j_l\,(k_1 a)\right] & 0 \\ 0 & -j_l\,(k_1 a) \end{pmatrix}\begin{pmatrix} \mathbf{a}_1 \\ \mathbf{a}_2 \end{pmatrix} = \begin{pmatrix} \frac{1}{\omega_2\varepsilon_2}\frac{1}{a}\frac{\partial}{\partial a}\left[a\cdot h_l\,(k_2 a)\right] & 0 \\ 0 & -h_l\,(k_2 a) \end{pmatrix}\begin{pmatrix} \mathbf{b}_1 \\ \mathbf{b}_2 \end{pmatrix}. \tag{6.40}$$

Multiplying this through produces two equations;

$$\frac{1}{\omega_1 \varepsilon_1} \frac{1}{a} \frac{\partial}{\partial a} \left[a \cdot j_l \left(k_1 a\right)\right] \cdot \mathbf{a}_1 = \frac{1}{\omega_2 \varepsilon_2} \frac{1}{a} \frac{\partial}{\partial a} \left[a \cdot h_l \left(k_2 a\right)\right] \cdot \mathbf{b}_1, \tag{6.41}$$

and

$$-j_l \left(k_1 a\right) \cdot \mathbf{a}_2 = -h_l \left(k_2 a\right) \cdot \mathbf{b}_2, \tag{6.42}$$

which can be cast in matrix form. Solutions then occur when the determinant of this matrix is zero;

$$\begin{vmatrix} \frac{1}{\omega_1 \varepsilon_1} \frac{1}{a} \frac{\partial}{\partial a} \left[a \cdot j_l \left(k_1 a\right)\right] & -\frac{1}{\omega_2 \varepsilon_2} \frac{1}{a} \frac{\partial}{\partial a} \left[a \cdot h_l \left(k_2 a\right)\right] \\ -j_l \left(k_1 a\right) & h_l \left(k_2 a\right) \end{vmatrix} = 0. \tag{6.43}$$

Multiplying this out gives

$$\frac{1}{\omega_1 \varepsilon_1} \frac{1}{a} \frac{\partial}{\partial a} \left[a \cdot j_l \left(k_1 a\right)\right] \cdot h_l \left(k_2 a\right) - \frac{1}{\omega_2 \varepsilon_2} \frac{1}{a} \frac{\partial}{\partial a} \left[a \cdot h_l \left(k_2 a\right)\right] \cdot j_l \left(k_1 a\right) = 0, \tag{6.44}$$

and substituting in using (6.26), (6.29) and (6.31) gives the transcendental equation for the TM case:

$$\sqrt{\varepsilon_1 \mu_2} H_l' \left(k_2 a\right) \cdot J_l \left(k_1 a\right) - \sqrt{\varepsilon_2 \mu_1} J_l' \left(k_1 a\right) \cdot H_l \left(k_2 a\right) = 0. \tag{6.45}$$

Taking (6.38) and performing similar manipulations and substitutions gives us the TE case:

$$\sqrt{\varepsilon_2 \mu_1} H_l' \left(k_2 a\right) \cdot J_l \left(k_1 a\right) - \sqrt{\varepsilon_1 \mu_2} J_l' \left(k_1 a\right) \cdot H_l \left(k_2 a\right) = 0. \tag{6.46}$$

These transcendental equations are identical to the denominators of (6.32) and (6.34) from the transmissivity problem.

6.1.4 Constant magnetic permittivity

We consider a sphere surrounded by a material with different dielectric constant but the same magnetic permittivity. In doing so we can investigate the light modes formed solely by the change in dielectric constant. We will only detail the derivation of the TM case here, as the TE case is almost identical.

We wish to find solutions to the problem of a dielectric sphere of radius a, surrounded by a material of different dielectric constant. The magnetic permittivity is the same in both materials, so that $\mu_1 = \mu_2 = \mu$, immediately simplifying (6.45) above;

$$\sqrt{\varepsilon_1} H_l'(k_2 a) \cdot J_l(k_1 a) - \sqrt{\varepsilon_2} J_l'(k_1 a) \cdot H_l(k_2 a) = 0. \tag{6.47}$$

and equation (6.46) to:

$$\sqrt{\varepsilon_2} H_l'(k_2 a) \cdot J_l(k_1 a) - \sqrt{\varepsilon_1} J_l'(k_1 a) \cdot H_l(k_2 a) = 0. \tag{6.48}$$

6.1.5 Angular momentum $l = 1$

The general dispersion equations above can be simplified for the specific case of angular momentum $l = 1$. The spherical Bessel functions for $l = 1$ given by:

$$\begin{aligned} j_1(x) &= \frac{\sin(x)}{x^2} - \frac{\cos(x)}{x}, \\ h_1(x) &= e^{ix}\left(\frac{-1}{x} - \frac{i}{x^2}\right), \end{aligned} \tag{6.49}$$

are substituted into equations (6.47) and (6.48) giving:

$$k_1 a = \arctan\left[\frac{k_1 k_2^2 a}{i k_1^2 k_2 a - k_1^2 + k_2^2}\right] + n\pi, \tag{6.50}$$

and for TE modes, and:

$$k_1 a = \arctan\left[\frac{-i k_1 a [k_1^2 k_2^2 a^2 + (1 - i k_2 a)(k_2^2 - k_1^2)]}{k_1^2 k_2^3 a^3 + (k_2 a + i)(k_1^2 - k_2^2)}\right] + n\pi, \tag{6.51}$$

for TM modes. Where n is the radial quantum number. TM and TE solutions can now be found numerically for any given set of system parameters by finding complex energies for which (6.50) or (6.51) is satisfied.

6.2 Correlation between $l = 0$ and $l = 1$ modes

Although modes with angular momentum $l = 0$ within a sphere are unphysical, there is a useful mathematical correlation between $l = 0$ and $l = 1$ photon modes which can be exploited during analytical derivations in order to greatly simplify the resulting equations. In this section we will derive the dispersion equations of the $l = 0$ modes, both in general and specifically in the non-interacting case, and numerically compare them with $l = 1$ to illustrate this correlation.

The reader is reminded that we refer to the transverse modes in the form TE_l and TM_l, so that $l = 0$ modes are called TE_0 and TM_0, and $l = 1$ modes are called TE_1 and TM_1 modes. The l subscript should not be confused with the radial mode number, n.

6.2.1 $l = 0$ dispersion equations

Taking the general dispersion equations, (6.45) and (6.46), and substituting in the $l = 0$ equations for the spherical Bessel functions;

$$j_0(x) = \frac{\sin(x)}{x}, \qquad\qquad (6.52)$$

$$h_0(x) = \tfrac{1}{x}\left[\sin(x) - i\cos(x)\right] = -\tfrac{i}{x}e^{ix},$$

we obtain;

$$\tan(k_1 a) = -i\frac{k_1}{k_2}, \qquad\qquad (6.53)$$

for TE modes, and:

$$\tan(k_1 a) = -i\frac{\varepsilon_2}{\varepsilon_1}\frac{k_1}{k_2}, \qquad\qquad (6.54)$$

for TM modes.

In the absence of any exciton-photon interaction, ε_1 and ε_2 become ε_b and ε_d, respectively. We can then substitute in for k_1 and k_2 using:

$$k_1 = \frac{\omega_n^0}{c}\sqrt{\varepsilon_\mathrm{b}}, \text{ and } k_2 = \frac{\omega_n^0}{c}\sqrt{\varepsilon_\mathrm{d}}, \qquad\qquad (6.55)$$

where ω_n^0 are the non-interacting photon mode frequencies, to give:

$$\omega_n^0 = \frac{1}{\tilde{a}}\left[\arctan(-i\sqrt{1/\tilde{\varepsilon}}) + n\pi\right], \qquad\qquad (6.56)$$

for TE modes, and:

$$\omega_n^0 = \frac{1}{\tilde{a}}\left[\arctan(-i\sqrt{\tilde{\varepsilon}}) + n\pi\right], \qquad\qquad (6.57)$$

for TM modes. Here we have introduced the dimensionless parameters $\tilde{\varepsilon} = \varepsilon_\mathrm{d}/\varepsilon_\mathrm{b}$, and $\tilde{a} = \sqrt{\varepsilon_\mathrm{b}}\omega_\mathrm{T}a/c$.

6.2.2 Numerical comparison of $l = 0$ and $l = 1$ modes

In figure 6.2 we plot numerical results from both $l = 1$ and $l = 0$ modes. The TE_1 and TM_1 polariton dispersion curves, calculated from equations (6.50) and (6.51) are in the weak coupling regime, and are plotted alongside TE_0 and TM_0 photon dispersions calculated with equations (6.56) and (6.57).

There is an obvious correlation between the modes plotted in figure 6.2, however the $l = 0$ and $l = 1$ modes do not agree on a one-to-one basis. Consideration of the mode numbers, which go from lowest real-frequency up to highest real-frequency, shows that the TM_1, $n = 0$ mode is approximately the same as the TE_0, $n = 1$ mode, the TE_1, $n = 1$ mode is very close to the TM_0, $n = 1$ mode, and so on. The TM_0, $n = 0$ mode lies along $\mathrm{Re}(\tilde{\omega}) = 0$, though it has a significant imaginary component, and the highest-order TM_1 mode has no corresponding $l = 0$ mode. This is because all sets of modes have been plotted up to $n = 4$.

The correlation between the modes is described as follows:

$$\begin{aligned} &\mathrm{TM}_1\text{, n mode} \simeq \mathrm{TE}_0\text{, (n+1) mode,} \\ &\mathrm{TE}_1\text{, n mode} \simeq \mathrm{TM}_0\text{, (n) mode,} \end{aligned} \tag{6.58}$$

assuming that $\tilde{\varepsilon} < 1$. In the less usual case of $\tilde{\varepsilon} > 1$, the correspondence becomes:

$$\begin{aligned} &\mathrm{TM}_1\text{, n mode} \simeq \mathrm{TE}_0\text{, (n) mode,} \\ &\mathrm{TE}_1\text{, n mode} \simeq \mathrm{TM}_0\text{, (n+1) mode.} \end{aligned} \tag{6.59}$$

The difference in the imaginary dispersions, figure 6.2(b), arises because the photon dispersions inherently have the same imaginary value set by the dielectric permittivities. Better agreement of the imaginary components would be obtained

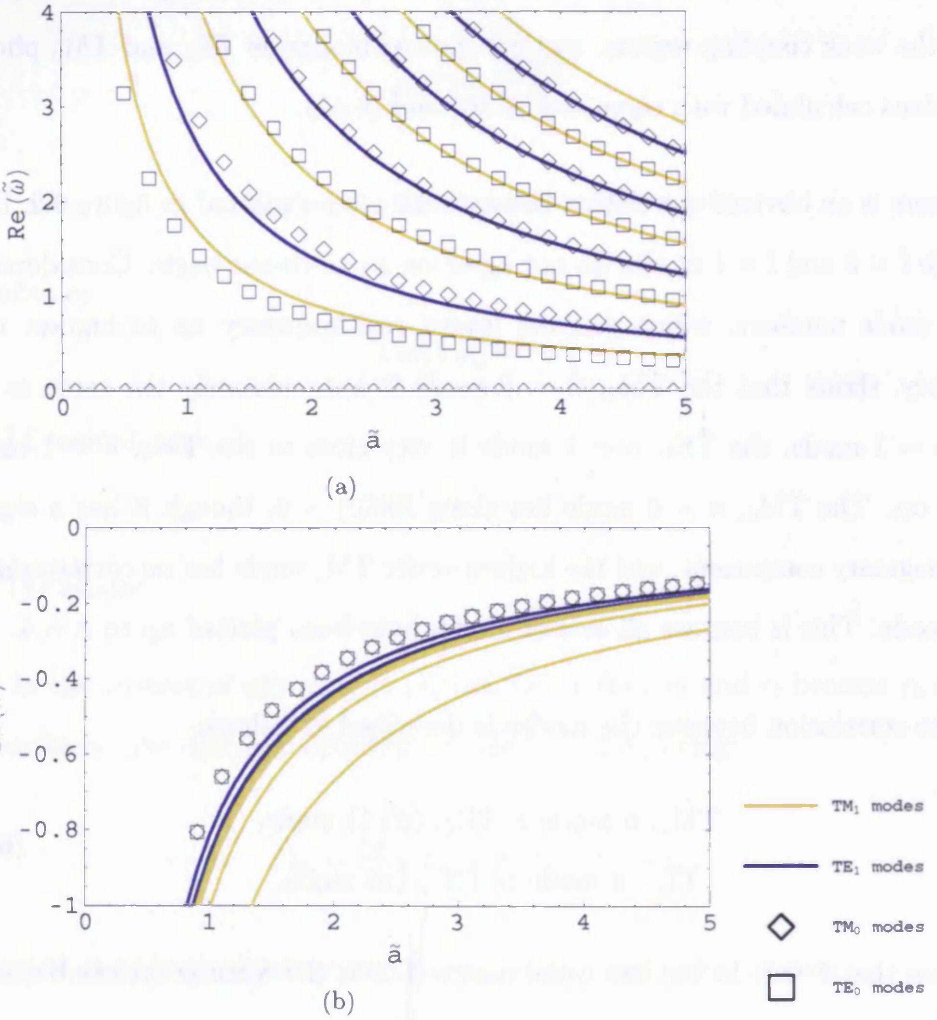

Figure 6.2: Plots of the (a) real, and (b) imaginary parts of the TE_1 polariton modes (blue lines), TM_1 polariton modes (yellow lines), TE_0 photon modes (open squares) and TM_0 photon modes (open diamonds). The TM modes are plotted for $n = 0$ to 4, and for TE modes $n = 1$ to 4. The simulation parameters are $\tilde{\omega}_p = 0.09$, $\tilde{\varepsilon} = 0.385$.

if the $l = 0$ polariton equations, (6.53) and (6.54), were used instead of the photon dispersions. However, this is generally far less useful as an analytical approximation.

6.3 Aspects of numerical solutions with Mathematica

This section highlights some of the problems associated with obtained numerical solutions to the equations presented in the manuscript. Although such solutions can be obtained using many programming languages and packages, and within each language different procedures and methods can be used, this section will focus on specific problems and solutions associated with using the Mathematica package.

6.3.1 Accuracy and precision

Most programming languages such as C, C+, and Fortran store numbers using the standard data constructs called Integer and Real numbers. However, the limitations of Real numbers can lead to inaccuracies in the results due to rounding errors. Mathematica also uses a form of Real numbers, but has some very useful features for extending beyond their usual limitations and thus avoiding numerical problems. Fortan 90 [89] will be used to compare and contrast with Mathematica.

Integer and Real numbers are represented in a computer using a set number of bits. This sets a fundamental limit on the accuracy to which a number can be stored and operated upon, as well as the maximum and minimum value that number can take. A real number, using a floating point representation, is typically stored with up to six or seven digits of precision. Usually computations take place in registers which have twice that level of precision, so numbers are operated on and then rounded for storage. This introduces rounding errors into calculations.

Mathematica does not have this limitation, and instead stores numbers (and operates on them) with any number of digits. Mathematica differentiates between two distinct types of numbers; *exact* numbers, which are represented perfectly with no rounding, and *approximate* numbers which have been rounded to some degree. An integer is exact, 5, as is the fraction 1/2. However, the floating point representation of 1/2; 0.5 is an approximate number.

Approximate numbers are rounded down to MachinePrecision. This is a setting within Mathematica which sets the numbers of digits used to represent a number. The standard value of MachinePrecision is:

In:= $MachinePrecision
Out:= 15.9546

This is similar to a normal Real number except that MachinePrecision can be changed. For example, π can be expressed as follows:

In:= N[π]
Out:= 3.14159

This is π expressed to MachinePrecision. However, we can easily change the level of precision being used, for example:

In:= N[π, 4]
Out:= 3.142

In:= N[π, 10]

Out:= 3.141592654

Here, the function $N[x, n]$ simply displays the variable x using a precision of n.

This ability to change the number of digits used to represent, store and operate upon a number is called *arbitrary precision.* This very useful concept can be implemented with other programming languages, usually as an additional library package, for example the Variable Precision Arithmetic package for Fortran 95 [90]. However, the use of higher precision numbers has the drawback of using more computer processor resources both to store and operate with that number. This inevitably leads to slower calculations and longer simulation times.

One solution to this problem is to express all numbers in the calculation as *exact* numbers. For example, $\tilde{\omega}_{\mathrm{p}} = 1.95$ can be expressed as 195×10^{-2}, $\tilde{\varepsilon} = 0.5$ as 5×10^{-1}. Exact numbers have an infinite precision, since they are defined completely, and require relatively little processor power.

Very high precision is required for accurate solutions to the dispersion equations throughout this thesis. In particular, the fine structure of modes around the excitonic resonance can produce very small fluctuations. These can easily be lost if the numbers are rounded too much. Typically a MachinePrecision value of 30 has been used for much of the numerical results shown in this thesis, but a value of 200 has been used in difficult cases.

6.3.2 Underflow and overflow errors

An underflow or overflow error occurs when the value of a variable, whether it is Integer, Real or Complex, exceeds the limits of the range of numbers that can be expressed using the given data structure. For example, a typical Integer is restricted to within a range of -10^9 to 10^9, and a real number to the range -10^{38} to 10^{38}. If a calculation generates a number which lies outside this range, it cannot be represented and an overflow error occurs. If a number is generated which has a magnitude which is so small that it cannot be expressed, an underflow occurs.

Different languages may respond differently to flow errors, but typically the variable will just be capped at the most extreme value that can be represented, and the calculation will continue. This effectively introduces an inaccuracy into the calculation. Since an integer variable which should be 10^{15} would be represented as being five orders of magnitude less than that, this form of error can be much more problematic than a simple rounding error.

With Mathematica the limits upon machine precision numbers are given by variables $MaxMachinePrecision and $MaxMachinePrecision, which have typical values of about 2×10^{308} and 2×10^{-308} respectively. This already significantly better than most standard programming languages, but this can be extended, since these values are 2^n, where n is the maximum exponent that can be used in the internal representation of machine-precision numbers. Hence one possibility to avoid flow error with Mathematica is to simply increase the precision of your variables, as discussed in the above section.

6.4 Complex slices

In solving the polariton dispersion equations throughout this thesis, the Rabi frequency and dielectric permittivities are generally set at given values, in effect describing the materials of the PD and surrounding medium. The complex polariton frequencies are then calculated as a function of radius. This produces a three dimensional (3D) solution space comprised of radius, a, and the real and imaginary parts of the frequency, $\mathrm{Re}(\omega) = \omega_r$ and $\mathrm{Im}(\omega) = \omega_i$. Plotting this data clearly is critical to analysing the results and understanding the underlying physics. Thankfully Mathematica includes a range of functions for plotting both 2D and 3D graphs.

2D graphs of any function $f(x)$ can be produced simply using the Plot function. A 2D data set can be plotted using ListPlot. These are basic functions and are covered quite extensively in The Mathematica Book [66, sections 1.91 and 1.98 respectively]. 3D versions of this functions, Plot3D and ListPlot3D, also exist and function in a very similar manner. The 3D graphs in figures 4.1 and 4.2, illustrating the meeting of the two polariton branches at the transition point, were generated using the ListPlot3D function. Plotting this single mode alone, over a relatively short section of the solution space, produced a clear graph, but including additional modes quickly clutters such graphs. Hence 2D graphs have been used to show multiple mode dispersions.

The polariton mode solutions to a dispersion equation can be expressed in a general form as $f(\omega_r + i\omega_i, a) = 0$, for given dielectric permittivities. However, for values of ω and a which do not correspond to a solution, the function will take non-zero values, $f(\omega_r + i\omega_i, a) = x$, where x may be complex. So, in searching for solutions we have a 4D solution space; ω_r, ω_i, a and x.

To make this manageable in terms of graphing solutions we take the absolute value of the function, $Abs[f((\omega_r + i\omega_i, a)]$ to force x to be real. A 3D plot can then be made x over a complex plane, ω_r, ω_i. We effectively take a slice through the 4D solution space to produce a 3D graph. An example is shown in figure 6.3(a) for a direct numerical solution of equation 2.3 for TE_1 modes. The parameters $\tilde{\omega}_{\mathrm{p}} = 1.95$ and $\tilde{\varepsilon} = 0.52$, are the same as for figure 2.6. An arbitrary radius of $\tilde{a} = 5$ has been chosen.

The plot is featureless except for a large increase for highly-negative values of ω_i. The code to generate this figure is:

In:= Plot3D[Abs[f[ω_r + $i\omega_i$,a]], {ω_r,0,5}, {ω_i,-5,5}]

but since we are searching for solutions near zero, we add a PlotRange option:

In:= Plot3D[Abs[f[ω_r + $i\omega_i$,a]], {ω_r,0,5}, {ω_i,-5,5},
PlotRange→{All, All, {0,0.5}}]

The third entry in the PlotRange sets the z-axis range for the plot. The resulting graph is shown in figure 6.3(b).

Solutions can be seen at the minima of this plot. However, the 3D nature of the graph makes the solutions difficult to isolate. It is therefore much better to use the ContourPlot function to produce a very similar effect to Plot3D, but resulting in a 2D, "bird's-eye-view", of the complex plane, as shown in figure 6.4. Such plots are called a *complex slice* because they provide a clear illustration of the topology of the dispersion curve for that given radius, within the 4D solution space.

The region of the complex plane being shown in figure 6.4, as well as the range of values over which the figure is plotted, has been chosen to illustrate

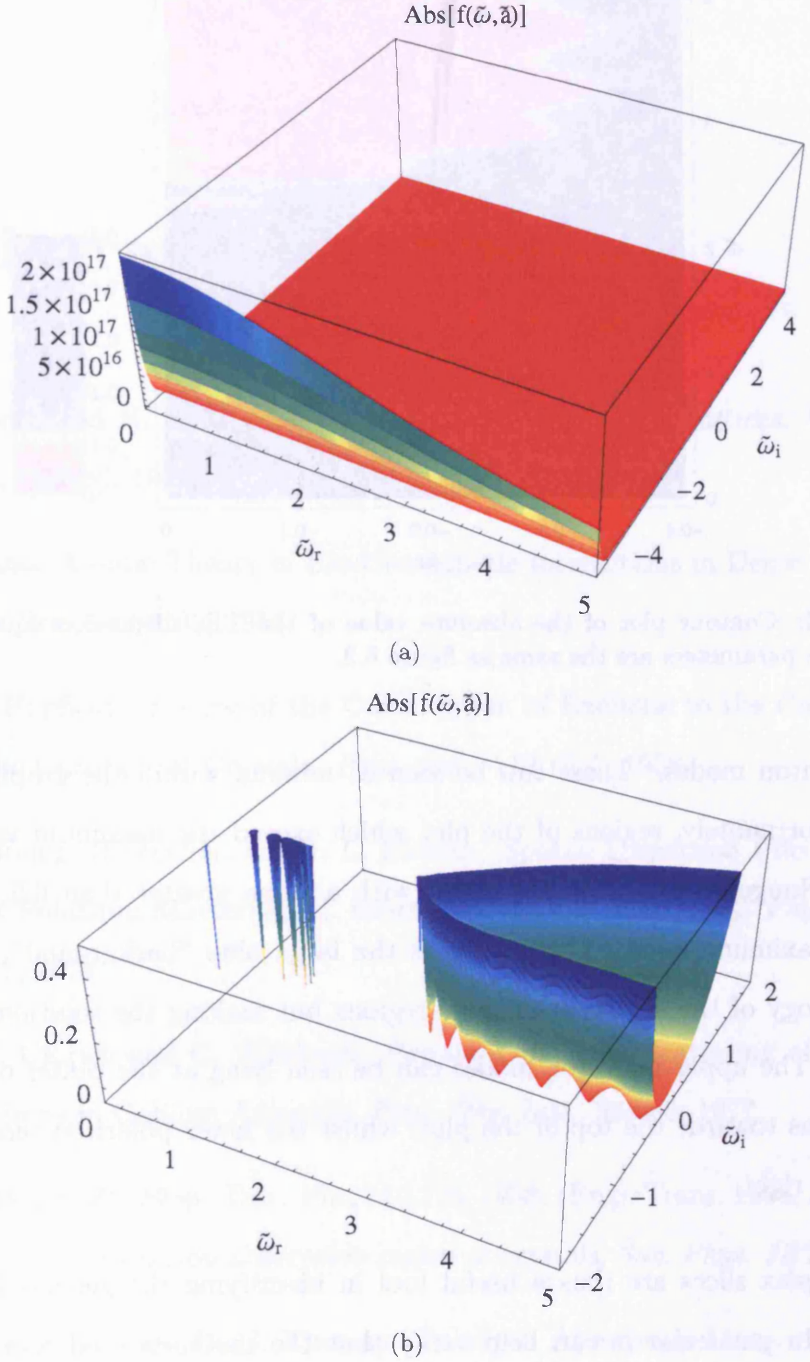

(a)

(b)

Figure 6.3: 3D plot of the absolute value of the TE_1 dispersion equation (a) as calculated, (b) plotted only within a range $0 \leq \mathrm{Abs}[\mathrm{f}(\tilde{\omega},\tilde{a})] \leq 0.5$, over a range of complex frequency. $\tilde{\omega}_\mathrm{p} = 1.95$, $\tilde{\varepsilon} = 0.52$, $\tilde{a} = 5$.

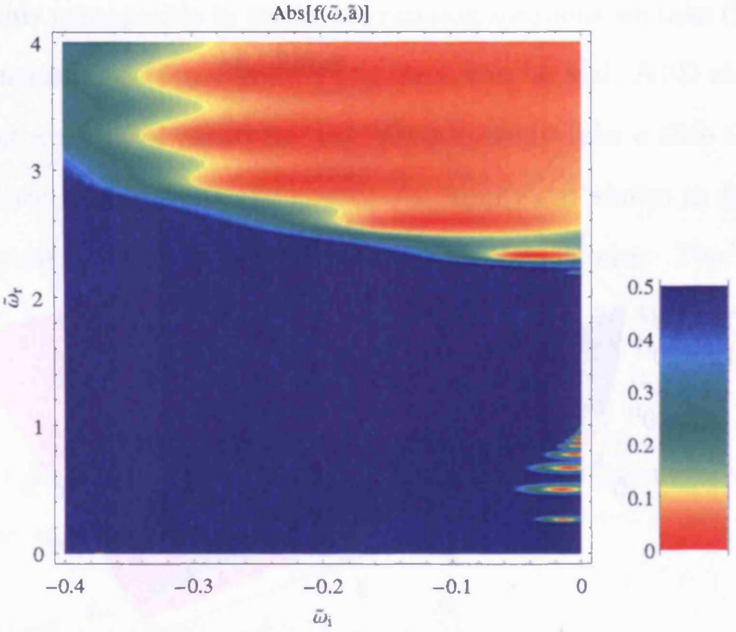

Figure 6.4: Contour plot of the absolute value of the TE_1 dispersion equation. The simulation parameters are the same as figure 6.3.

the polariton modes. These can be seen as minima within the graph, coloured red. Unfortunately, regions of the plot which exceed the maximum value set by our PlotRange, in this case any point with a value greater than 0.5, is plotted at the maximum value. This produces the large blue "background", obscuring the topology of the solutions in these regions but making the solutions easier to identify. The upper polariton modes can be seen lying at the center of the large red regions towards the top of the plot, whilst the lower polariton modes are on the lower right.

Complex slices are thus a useful tool in identifying the general location of modes. In particular it can help verify that the methods used to find modes through exact solutions of the dispersion equation have located all of the polariton modes, and none have been overlooked.

Bibliography

[1] M. Born and K. Huang. *Dynamical Theory of Crystal Lattices.* Clarendon Press, Oxford, 1954.

[2] U. Fano. Atomic Theory of Electromagnetic Interactions in Dense Materials. *Phys. Rev.*, 103:1202, 1956.

[3] J. J. Hopfield. Theory of the Contribution of Excitons to the Complex Dielectric Constant of Crystals. *Phys. Rev.*, 112:1555, 1958.

[4] W. Brenig, R. Zeyher, and J. L. Birman. Spatial Dispersion Effects in Resonant Polariton Scattering. II. Resonant Brillouin Scattering. *Phys. Rev. B*, 6:4617, 1972.

[5] R. G. Ulbrich and C. Weisbuch. Resonant Brillouin Scattering of Excitonic Polaritons in Gallium Arsenide. *Phys. Rev. Lett.*, 38:865, 1977.

[6] S. I. Pekar. *Zh. Eksp. Teor. Fiz.*, 34:1176, 1958. (Engl. Trans. 1958, Dispersion of light in the exciton absorption region of crystals, *Sov. Phys. JETP*, 7:813).

[7] J. J. Hopfield and D. G. Thomas. Polariton Absorption Lines. *Phys. Rev. Lett.*, 15:22, 1965.

[8] J. Voigt. Influence of spatial-dispersion on transmission spectra of CdS single-crystals. *Phys. Stat. Sol. (b)*, 64:549, 1974.

[9] C. Benoit a la Guillaume, A. Bonnot, and J. M. Debever. Luminescence from Polaritons. *Phys. Rev. Lett.*, 24:1235, 1970.

[10] E. Gross, S. Permogorov, V. Travnikov, and A. Selkin. Polariton emission from crystals. *Solid State Commun.*, 10:1071, 1972.

[11] C. Weisbuch and R. G. Ulbrich. Resonant Polariton Fluorescence in Gallium Arsenide. *Phys. Rev. Lett.*, 39:654, 1977.

[12] D. Fröhlich, E. Mohler, and P. Wiesner. Observation of Exciton Polariton Dispersion in CuCl. *Phys. Rev. Lett.*, 26:554, 1971.

[13] J. J. Hopfield and D. G. Thomas. Theoretical and Experimental Effects of Spatial Dispersion on the Optical Properties of Crystals. *Phys. Rev.*, 132:563, 1963.

[14] F. Evangelisti, A. Frova, and J. U. Fischbach. Electric-Field-Induced Interference Effects at the Ground Exciton Level in GaAs. *Phys. Rev. Lett.*, 29:1001, 1972.

[15] R. Tsu. Silicon-based quantum wells. *Nature*, 364:19, 1993.

[16] L. Jacak, P. Hawrylak, and A. Wojs. *Quantum Dots.* Springer-Verlag, Berlin, 1998.

[17] J.P. Reithmaier and A. Forchel. Recent advances in semiconductor quantum-dot lasers. *Comptes Rendus Physique*, 4:611, 2003.

[18] J. D. Joannopoulos, R.D. Meade, and J. N. Winn. *Photonic Crystals: Molding the Flow of Light.* Princeton University Press, 1995.

[19] L. M. Herz and R. T. Phillips. Quantum computing: Fine lines from dots. *Nature Materials*, 1:212, 2002.

[20] N. Gisin, G. Ribordy, W. Tittel, and H. Zbinden. Quantum cryptography. *Rev. Mod. Phys.*, 74:145, 2002.

[21] C. Weisbuch and R. G. Ulbrich in *Light scattering in solids III*, edited by M. Cardona and G. Güntherodt. Springer-Verlag, Berlin, 1982.

[22] Y. Toyozawa. Interband effect of lattice vibrations in the exciton absorption spectra. *J. Phys. Chem. Solids*, 25:59, 1964.

[23] R. S. Knox in *Solid State Physics*, supplement 5, edited by F. Seitz and D. Turnbull. Academic Press, New York, 1963.

[24] C. P. Slichter. *Principles of Magnetic Resonance.* Springer, Berlin, 1980.

[25] A. Abragam. *The Principles of Nuclear Magnetism.* Cambridge University Press, Cambridge, 1961.

[26] W. C. Tait. Quantum Theory of a Basic Light-Matter Interaction. *Phys. Rev. B*, 5:648, 1971.

[27] M. F. Bishop and A. A. Maradudin. Energy flow in a semi-infinite spatially dispersive absorbing dielectric. *Phys. Rev. B*, 14:3384, 1976.

[28] G. Bastard. *Wave Mechanics Applied to Semiconductor Heterostructures.* Les Editions de Physique, Paris, 1989.

[29] J. H. Davies. *The Physics of Low-dimensional Semiconductors.* Cambridge University Press, Cambridge, 1998.

[30] G. Bastard, E. E. Mendez, L. L. Chang, and L. Esaki. Exciton binding energy in quantum wells. *Phys. Rev. B*, 26:1974, 1982.

[31] R. L. Greene, K. K. Bajaj, and D. E. Phelps. Energy levels of Wannier excitons in GaAs-Ga$_{1-x}$Al$_x$As quantum-well structures. *Phys. Rev. B*, 29:1807, 1984.

[32] L. C. Andreani and A. Pasquarello. Accurate theory of excitons in GaAs-$Ga_{1-x}Al_xAs$ quantum wells. *Phys. Rev. B*, 42:8928, 1990.

[33] M. Gurioli, J. Martinez-Pastor, M. Colocci, A. Bosacchi, S. Franchi, and L. C. Andreani. Well-width and aluminum-concentration dependence of the exciton binding energies in $GaAs/Al_xGa_{1-x}As$ quantum wells. *Phys. Rev. B*, 47:15755, 1993.

[34] K. Cho and M. Kawata. Theoretical Analysis of Polariton Interference in a Thin Platelet of CuCl. I. Additional Boundary Condition. *J. Phys. Soc. Jpn.*, 54:4431, 1985.

[35] A. D'Andrea and R. Del Sole. Exciton quantization and polariton propagation in semiconductor slabs: From semi-infinite crystals to quantum wells. *Phys. Rev. B*, 41:1413, 1990.

[36] A. Tredicucci, Y. Chen, F. Bassani, J. Massies, C. Deparis, and G. Neu. Center-of-mass quantization of excitons and polariton interference in GaAs thin layers. *Phys. Rev. B*, 47:10348, 1993.

[37] M. Nakayama. Theory of the excitonic polariton of the quantum well. *Solid State Commun.*, 55:1053, 1985.

[38] L. C. Andreani and F. Bassani. Exchange interaction and polariton effects in quantum-well excitons. *Phys. Rev. B*, 41:7536, 1990.

[39] S. Jorda, U. Rössler, and D. Broido. Fine structure of excitons and polariton dispersion in quantum wells. *Phys. Rev. B*, 48:1669, 1993.

[40] L. C. Andreani. *Exciton-polaritons in confined systems*, in *Electron and Photon Confinement in Semiconductor Nanostructures*, edited by B. Deveaud, A. Quattropani and P. Schwendimann. IOS Press, Amsterdam, 2003.

[41] E. Hanamura. Rapid radiative decay and enhanced optical nonlinearity of excitons in a quantum well. *Phys. Rev. B*, 38:1228, 1988.

[42] L. C. Andreani, F. Tassone, and F. Bassani. Radiative lifetime of free excitons in quantum wells. *Solid State Commun.*, 77:641, 1991.

[43] M. Born and E. Wolf. *Principles of Optics.* Pergamon Press, London, 4th edition, 1970.

[44] M. S. Skolnick, T. A. Fisher, and D. M. Whittaker. Strong coupling phenomena in quantum microcavity structures. *Semicond. Sci. Technol.*, 13:645, 1998.

[45] A. V. Kavokin and G. Malpuech. *Cavity Polaritons.* Elsevier, Amsterdam, 2003.

[46] P. G. Savvidis, J. J. Baumberg, R. M. Stevenson, M. S. Skolnick, D. M. Whittaker, and J. S. Roberts. Angle-Resonant Stimulated Polariton Amplifier. *Phys. Rev. Lett.*, 84:1547, 2000.

[47] R. Huang, Y. Yamamoto, R. Andre, J. Bleuse, M. Muller, and H. Ulmer-Tuffigo. Exciton-polariton lasing and amplification based on exciton-exciton scattering in CdTe microcavity quantum wells. *Phys. Rev. B*, 65:165314, 2002.

[48] A. V. Kavokin, G. Malpuech, and F. P. Laussy. Polariton laser and polariton superfluidity in microcavities. *Phys. Lett. A*, 306:187, 2003.

[49] C. Weisbuch, M. Nishioka, A. Ishikawa, and Y. Arakawa. Observation of the coupled exciton-photon mode splitting in a semiconductor quantum microcavity. *Phys. Rev. Lett.*, 69:3314, 1992.

[50] J.-M. Gérard, D. Barrier, J.-Y. Marzin, R. Kuszelewicz, L. Manin, E. Costard, V. Thierry-Mieg, and T. Rivera. Quantum boxes as active probes for photonic microstructures: The pillar microcavity case. *Appl. Phys. Lett.*, 69:449, 1996.

[51] G. Panzarini and L. C. Andreani. Quantum theory of exciton polaritons in cylindrical semiconductor microcavities. *Phys. Rev. B*, 60:16799, 1999.

[52] R. Ruppin. Optical-properties of spatially dispersive dielectric spheres. *J. Opt. Soc. Am.*, 71:755, 1981.

[53] R Ruppin. Optical absorption by excitons in microcrystals. *J. Phys. Chem. Solids*, 50:877, 1989.

[54] H. Ajiki and K. Cho. Longitudinal and transverse components of excitons in a spherical quantum dot. *Phys. Rev. B*, 62:7402, 2000.

[55] H. Ajiki, T. Tsuji, K. Kawano, and K. Cho. Optical spectra and exciton-light coupled modes of a spherical semiconductor nanocrystal. *Phys. Rev. B*, 66:245322, 2002.

[56] A. I. Tartakovskii, D. N. Krizhanovskii, G. Malpuech, M. Emam-Ismail, A. V. Chernenko, A. V. Kavokin, V. D. Kulakovskii, M. S. Skolnick, and J. S. Roberts. Giant enhancement of polariton relaxation in semiconductor microcavities by polariton-free carrier interaction: Experimental evidence and theory. *Phys. Rev. B*, 67:165302, 2003.

[57] M. A. Kaliteevski, S. Brand, R. A. Abram, V. V Nikolaev, M. V. Maximov, C. M. Sotomayor Torres, and A. V. Kavokin. Electromagnetic theory of the coupling of zero-dimensional exciton and photon states: A quantum dot in a spherical microcavity. *Phys. Rev. B*, 64:115305, 2001.

[58] J. E. Inglesfield. The embedding method for electromagnetics. *J. Phys. A: Math. Gen.*, 31:8495, 1998.

[59] P. Bigenwald, V. V. Nikolaev, D. Solnyshkov, A. Kavokin, G. Malpuech, and B. Gil. Polariton lasers based on semiconductor quantum microspheres. *Phys. Rev. B*, 70:205343, 2004.

[60] W. K. H. Panovsky and M. Phillips. *Classical Electricity and Magnetism.* Addison-Wesley, London, 1962.

[61] D. S. Jones. *The Theory of Electromagnetism.* Pergamon, London, 1964.

[62] J. D. Jackson. *Classical Electrodynamics.* Wiley, New York, 1999.

[63] Y. Kayanuma. Quantum-size effects of interacting electrons and holes in semiconductor microcrystals with spherical shape. *Phys. Rev. B*, 38:9797, 1988.

[64] T. Itoh, Y. Iwabuchi, and M. Kataoka. Study on the size and shape of CuCl microcrystals embedded in alkali-chloride matrices and their correlation with exciton confinement. *Phys. Stat. Sol. (b)*, 145:567, 1988.

[65] T. Itoh, M. Furumiya, T. Ikehara, and C. Gourdon. Size-dependent radiative decay time of confined excitons in CuCl microcrystals. *Solid State Commun.*, 73:271, 1990.

[66] S. Wolfram. *The Mathematica Book.* Wolfram Media, Champaign, IL, 5th edition, 2003.

[67] V. M. Agranovich, D. M. Basko, G. C. La Rocca, and F. Bassani. Excitons and optical nonlinearities in hybrid organic-inorganic nanostructures. *J. Phys.: Condens. Matt.*, 10:9369, 1998.

[68] H. Zhoubi and G. C. La Rocca. Exciton-polariton kinematic interactions in organic microcavities. *Phys. Rev. B*, 72:125306, 2005.

[69] K. Edamatsu, S. Yano, S. Iwai, T. Itoh, T. Goto, and A. Ekimov. Subpicosecond dynamics of confined excitons and optical nonlinearities of CuCl quantum dots. *J. Lumin.*, 66-67:406, 1995.

[70] T. Itoh, S. Yano, S. Iwai, K. Edamatsu, T. Goto, and A. Ekimov. Subpicosecond dynamics of confined excitons in CuCl nanocrystals. *Mater. Sci. Eng. A*, 217:167, 1996.

[71] R. Fuchs and K. L. Kliewer. Optical Modes of Vibration in an Ionic Crystal Sphere. *J. Opt. Soc. Am.*, 58:319, 1968.

[72] R. Ruppin in *Electromagnetic Surface Modes*, edited by A. D. Boardman. Wiley, New York, 1982, p.345-398.

[73] J. A. Stratton. *Electromagnetic Theory.* McGraw-Hill Book Company, New York, 1941.

[74] A. L. Ivanov, H. Haug, and L. V. Keldysh. Optics of excitonic molecules in semiconductors and semiconductor microstructures. *Phys. Reports*, 296:237, 1998.

[75] A. Hobson, W. L. Barnes, D. G. Lidzey, G. A. Gehring, D. M. Whittaker, M. S. Skolnick, and S. Walker. Strong excitonphoton coupling in a low-Q all-metal mirror microcavity. *Appl. Phys. Lett.*, 81:3519, 2002.

[76] V. M. Agranovich, M. Litinskaia, and D. G. Lidzey. Cavity polaritons in microcavities containing disordered organic semiconductors. *Phys. Rev. B*, 67:085311, 2003.

[77] D. G. Lidzey, D. D. C. Bradley, T. Virgili, A. Armitage, M. S. Skolnick, and S. Walker. Room Temperature Polariton Emission from Strongly Coupled Organic Semiconductor Microcavities. *Phys. Rev. Lett.*, 82:3316, 1999.

[78] A. I. Tartakovskii, M. Emam-Ismail, D. G. Lidzey, M. S. Skolnick, D. D. C. Bradley, S. Walker, and V. M. Agranovich. Raman scattering in strongly coupled organic semiconductor microcavities. *Phys. Rev. B*, 63:121302, 2001.

[79] K. L. Kliewer and R. Fuchs. Optical Modes of Vibration in an Ionic Crystal Slab Including Retardation. II. Radiative Region. *Phys. Rev.*, 150:573, 1966.

[80] E. Hanamura. Gigantic nonlinear optical polarizability of semiconductor microcrystallites. *Solid State Commun.*, 62:465, 1987.

[81] E. Hanamura. Very large optical nonlinearity of semiconductor microcrystallites. *Phys. Rev. B*, 37:1273, 1988.

[82] R. Ruppin. Electromagnetic energy density in a dispersive and absorptive material. *Phys. Lett. A*, 299:309, 2002.

[83] S. I. Pekar. *Zh. Eksp. Teor. Fiz.*, 33:1022, 1957.

[84] A. I. Ekimov, A. A. Onushchenko, M. E. Raikh, and Al. L. Efros. Size quantization of excitons in microcrystals with large longitudinal-transervse splitting. *Zh. Eksp. Teor. Fiz.*, 90:1795, 1985. (Engl. Trans. 1986, *Sov. Phys. JETP*, 63:1054).

[85] M. Cardona. *Modulation Spectroscopy.* Academic, New York, 1969.

[86] G. P. Johari, C. Ferrari, E. Tombari, and G. Salvetti. Temperature modulation effects on a material's properties: Thermodynamics and dielectric relaxation during polymerization. *J. Chem. Phys.*, 110:11592, 1999.

[87] K. Yamanaka, H. Cho, and Y. Tsukahara. Precise velocity measurement of surface acoustic waves on a bearing ball. *Appl. Phys. Lett.*, 76:2797, 2000.

[88] W. C. Chew. *Waves and Fields in Inhomogenous Media.* IEEE Press, New York, 1995.

[89] T. M. R. Ellis, I. R. Philips, and T. M. Lahey. *Fortran 90 Programming.* Addison-Wesley, Wokingham, 1994.

[90] J. J. Schonfelder. Variable precision arithmetic: a Fortran 95 module. *ACM SIGPLAN Fortran Forum*, 20:2, 2001.